



Defense Nuclear Agency  
Alexandria, VA 22310-3398

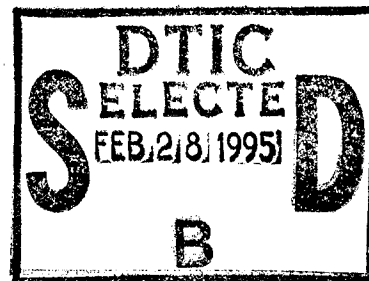


DNA-TR-93-175

## Near Surface Dust—Late Time Atmospheric Effects

R. Ian Sykes  
Douglas S. Henn  
Carmen P. Cerasoli  
The Titan Corporation  
Titan Research & Technology Div  
P.O. Box 2229  
Princeton, NJ 08543-2229

February 1995



Technical Report

CONTRACT No. DNA 001-91-C-0154

Approved for public release;  
distribution is unlimited.

19950217 005

**Destroy this report when it is no longer needed. Do not  
return to sender.**

**PLEASE NOTIFY THE DEFENSE NUCLEAR AGENCY,  
ATTN: CSTI, 6801 TELEGRAPH ROAD, ALEXANDRIA, VA  
22310-3398, IF YOUR ADDRESS IS INCORRECT, IF YOU  
WISH IT DELETED FROM THE DISTRIBUTION LIST, OR  
IF THE ADDRESSEE IS NO LONGER EMPLOYED BY YOUR  
ORGANIZATION.**



## DISTRIBUTION LIST UPDATE

This mailer is provided to enable DNA to maintain current distribution lists for reports. (We would appreciate your providing the requested information.)

- Add the individual listed to your distribution list.
- Delete the cited organization/individual.
- Change of address.

### NOTE:

Please return the mailing label from the document so that any additions, changes, corrections or deletions can be made easily. For distribution cancellation or more information call DNA/IMAS (703) 325-1036.

NAME: \_\_\_\_\_

ORGANIZATION: \_\_\_\_\_

### OLD ADDRESS

---

---

---

### CURRENT ADDRESS

---

---

---

TELEPHONE NUMBER: ( ) \_\_\_\_\_

### DNA PUBLICATION NUMBER/TITLE

---

---

---

### CHANGES/DELETIONS/ADDITIONS, etc.) (Attach Sheet if more Space is Required)

---

---

---

DNA OR OTHER GOVERNMENT CONTRACT NUMBER: \_\_\_\_\_

CERTIFICATION OF NEED-TO-KNOW BY GOVERNMENT SPONSOR (if other than DNA):

SPONSORING ORGANIZATION: \_\_\_\_\_

CONTRACTING OFFICER OR REPRESENTATIVE: \_\_\_\_\_

SIGNATURE: \_\_\_\_\_

CUT HERE AND RETURN



**DEFENSE NUCLEAR AGENCY  
ATTN: IMAS  
6801 TELEGRAPH ROAD  
ALEXANDRIA, VA 22310-3398**

**DEFENSE NUCLEAR AGENCY  
ATTN: IMAS  
6801 TELEGRAPH ROAD  
ALEXANDRIA, VA 22310-3398**

REPORT DOCUMENTATION PAGE			Form Approved OMB No. 0704-0188
<p>Public reporting burden for this collection of information is estimated to average 1 hour per response including the time for reviewing instructions, searching existing data sources, gathering and maintaining the data needed, and completing and reviewing the collection of information. Send comments regarding this burden estimate or any other aspect of this collection of information, including suggestions for reducing this burden, to Washington Headquarters Services Directorate for Information Operations and Reports, 1215 Jefferson Davis Highway, Suite 1204, Arlington, VA 22202-4302, and to the Office of Management and Budget, Paperwork Reduction Project (0704-0188), Washington, DC 20503.</p>			
1. AGENCY USE ONLY (Leave blank)	2. REPORT DATE	3. REPORT TYPE AND DATES COVERED	
	950201	Technical 910901 – 931031	
4. TITLE AND SUBTITLE		5. FUNDING NUMBERS	
Near Surface Dust—Late Time Atmospheric Effects		C - DNA 001-91-C-0154 PE - 62715H PR - RA TA - RG WU - DH314000	
6. AUTHOR(S)			
R. Ian Sykes, Douglas S. Henn, and Carmen P. Cerasoli			
7. PERFORMING ORGANIZATION NAME(S) AND ADDRESS(ES)		8. PERFORMING ORGANIZATION REPORT NUMBER	
The Titan Corporation Titan Research & Technology Div P.O. Box 2229 Princeton, NJ 08543-2229		A.R.A.P. Report No. 702	
9. SPONSORING/MONITORING AGENCY NAME(S) AND ADDRESS(ES)		10. SPONSORING/MONITORING AGENCY REPORT NUMBER	
Defense Nuclear Agency 6801 Telegraph Road Alexandria, VA 22310-3398 SPWE/Byers		DNA-TR-93-175	
11. SUPPLEMENTARY NOTES			
This work was sponsored by the Defense Nuclear Agency under RDT&E RMC Code B4662D RA RG 00261 4400A AC 25904D.			
12a. DISTRIBUTION/AVAILABILITY STATEMENT		12b. DISTRIBUTION CODE	
Approved for public release; distribution is unlimited.			
13. ABSTRACT (Maximum 200 words)			
<p>Atmospheric processes determining the late-time evolution of near-surface dust concentrations from nuclear bursts are examined, with the objective of providing model representations for late-time dispersion codes. Turbulent transfer in the atmospheric boundary layer is an important phenomenon for small particles, since turbulent eddy velocities are on the order of <math>1\text{ms}^{-1}</math> and extend from the surface up to altitudes of 1 km or higher. Simplified estimates for turbulence structure and diffusion rates are given. The effect of absorption of solar radiation by the dust is also considered, and a radiative transfer mode is described.</p> <p>Turbulent deposition of particles to various surface types, including open terrain or vegetative canopies, is considered and simple parameterization schemes are recommended.</p> <p>An extensive study of boundary layer flow over complex terrain has been conducted, using Large-Eddy Simulation to represent the energy-containing turbulent motions. A generalized scheme for estimating the average surface drag over complex terrain is derived. The effect of terrain on atmospheric turbulence levels and dispersion characteristics is studied, and simple estimation schemes for use in late-time models are suggested.</p>			
14. SUBJECT TERMS			15. NUMBER OF PAGES
Dust Cloud	Turbulence	Terrain Effects	154
Nuclear Cloud	Transport and Diffusion	Dry Deposition	
Atmospheric Diffusion	Planetary Boundary Layer	Radiative Absorption	16. PRICE CODE
17. SECURITY CLASSIFICATION OF REPORT	18. SECURITY CLASSIFICATION OF THIS PAGE	19. SECURITY CLASSIFICATION OF ABSTRACT	20. LIMITATION OF ABSTRACT
UNCLASSIFIED	UNCLASSIFIED	UNCLASSIFIED	SAR

**UNCLASSIFIED**

SECURITY CLASSIFICATION OF THIS PAGE

CLASSIFIED BY:

N/A since Unclassified.

DECLASSIFY ON:

N/A since Unclassified.

## SUMMARY

The atmospheric processes determining the late-time evolution of near-surface dust concentrations from a nuclear burst are examined. Late-time dispersion models, which describe the dust cloud during the period from cloud stabilization to many hours after initiation, have principally focused on wind transport and fallout phenomena. However, some applications require knowledge of the environment near the ground and other processes can play an important role in this region.

The atmosphere near the ground is usually turbulent; the wind blowing over the rough surface produces shear-driven turbulence, and daytime heating of the surface generates buoyancy-driven turbulence. Vertical diffusion of dust particles is therefore a significant effect with vertical velocity fluctuations of the order of  $1\text{ms}^{-1}$  maintaining small particles aloft for long periods, and strongly influencing the vertical distribution of dust. The turbulent layer, known as the planetary boundary layer (PBL), varies in depth from a few hundred meters up to 2km or more during the day, but is usually much shallower under nocturnal conditions. The effects of the PBL are therefore strongly dependent on the time of day and meteorological conditions, and cannot be properly represented by a fixed diffusivity.

The research reported here seeks to provide representations of the boundary layer processes for late-time dispersion models. The parameterization of the PBL turbulence and diffusion is discussed, and the effects of radiative absorption by the dust are also considered. The deposition of particles on the surface through turbulent processes, as distinct from gravitational settling, are examined. This process, known as dry deposition, is important for small particles with diameters less than about  $30\mu\text{m}$ , since the turbulent deposition rates can dominate the overall removal rate. Parameterization schemes exist in the literature, describing the effects of vegetative canopies and rough surfaces, and a general representation for use in late-time models is constructed. The structure of the PBL is considered in the representation, and a new description of the turbulent velocity fluctuations for light wind conditions is obtained.

The existing descriptions of the PBL are generally restricted to homogeneous, i.e., flat, conditions, whereas most land regions of the globe are not flat. A significant part of the research reported here was devoted to extending our understanding of boundary layer processes over complex terrain, and a large number of detailed turbulent simulations were

performed for a range of terrain shapes. Results were obtained for the surface flux of momentum, which determines the mean boundary layer transport velocity, and statistics for the turbulent fluctuations were also examined. A general parameterization for the mean surface drag and boundary layer wind is obtained, which fits numerical results for a wide range of meteorological conditions and terrain shapes. The representation utilizes the r.m.s. terrain slopes and elevation variations, and is constructed with a proper tensor form so that directional effects are correctly described for terrain with dominant ridge-valley axes. Steep slopes induce lee separation, and the dispersion of particles over terrain was found to be strongly enhanced by the large mean velocity gradients. Turbulence levels are also increased by the shear distortions, and simple estimates for use in late-time dispersion models are suggested. In contrast to the dispersion effects, the turbulent deposition of dust particles was much less sensitive to terrain variations. This is because the deposition is dependent on the surface shear stress, while a large component of the force on the terrain is due to the pressure imbalance. The shear stress is increased over hill crests but is reduced in sheltered regions, so that the net change is generally small.

Accession For	
NTIS GRA&I	<input checked="" type="checkbox"/>
DTIC TAB	<input type="checkbox"/>
Unannounced	<input type="checkbox"/>
Justification	
By _____	
Distribution _____	
Availability Codes	
Avail. and/or Dist	Special

**CONVERSION TABLE**  
Conversion Factors for U.S. Customary to Metric (SI) Units of Measure

MULTIPLY TO GET	BY	TO GET DIVIDE
angstrom	1.000 000 X E -10	meters (m)
atmosphere (normal)	1.013 25 X E +2	kilo pascal (kPa)
bar	1.000 000 X E +2	kilo pascal (kPa)
British thermal unit (thermomechanical)	1.054 350 X E +3	joule (J)
calorie (thermomechanical)	4.184 000	joule (J)
cal (thermochemical)/cm <sup>2</sup>	4.184 000 000 X E -2	megajoule/m <sup>2</sup> (MJ/m <sup>2</sup> )
curie	3.700 000 X +	* giga becquerel (GBq)
degree (angle)	1.745 329 X E -2	radian (rad)
degree Fahrenheit	t <sub>K</sub> = (T F + 459.67)/1.8	degree kelvin (K)
electron volt	1.602 19 X E -19	joule (J)
erg	1.000 000 X E -7	joule (J)
erg/second	1.000 000 X E -7	watt (W)
foot	3.048 000 X E -1	meter (m)
foot-pound-force	1.355 818	joule (J)
gallon (US. liquid)	3.785 412 X E -3	meter <sup>3</sup> (m <sup>3</sup> )
inch	2.540 000 X E -2	meter (m)
jerk	1.000 000 X E +9	joule (J)
joule/kilogram (J/kg) (radiation dose absorbed)	1.000 000	Gray (Gy)
kilotons	4.183	terajoules
kip (1000 lbf)	4.448 222 X E +3	newton (N)
kip/inch <sup>2</sup> (ksi)	6.894 757 X E +3	kilo pascal (kPa)
ktap	1.000 000 X E +2	newton-second/m <sup>2</sup> (N·s/m <sup>2</sup> )
micron	1.000 000 X E -6	meter (m)
mil	2.540 000 X E -5	meter (m)
mile (international)	1.609 344 X E +3	meter (m)
ounce	2.834 952 X E -2	kilogram (kg)
pound-force (lbs avoirdupois)	4.448 222	newton (N)
pound-force inch	1.129 848 X E -1	newton-meter (N·m)
pound/force/inch	1.751 268 X E +2	newton/meter (N/m)
pound/force/foot <sup>2</sup>	4.788 026 X E -2	kilo pascal (kPa)
pound-force inch <sup>2</sup> (psi)	6.894 757	kilo pascal (kPa)
pound-mass (lbm avoirdupois)	4.535 924 X E -1	kilogram (kg)
pound-mass-foot <sup>2</sup> (moment of inertia)	4.214 011 X E -2	kilogram-meter
pound-mass-foot <sup>3</sup>	1.601 846 X E +1	kilogram/meter <sup>3</sup> (kg/m <sup>3</sup> )
rad (radiation dose absorbed)	1.000 000 X E -2	** Gray (Gy)
roentgen	2.579 760 X E -4	coulomb/kilogram (C/kg)
shake	1.000 000 X E -8	second (s)
slug	1.459 390 X E +1	kilogram (kg)
torr (mm Hg, O°C)	1.333 22 X E -1	kilo pascal (kPa)

\* the becquerel (Bq) is the SI unit of radioactivity; 1 Bq = 1 event/s.

\*\* The Gray (Gy) is the SI unit of absorbed radiation.

## TABLE OF CONTENTS

Section	Page
SUMMARY .....	iii
CONVERSION TABLE.....	v
FIGURES.....	viii
TABLES .....	xvi
<b>1 INTRODUCTION .....</b>	<b>1</b>
<b>1.1 BACKGROUND .....</b>	<b>1</b>
<b>1.2 PHYSICAL MECHANISMS .....</b>	<b>2</b>
<b>1.2.1 Turbulent Diffusion .....</b>	<b>2</b>
<b>1.2.2 Dry Deposition.....</b>	<b>3</b>
<b>1.2.3 Wet Deposition and Scavenging.....</b>	<b>4</b>
<b>1.2.4 Terrain Effects .....</b>	<b>5</b>
<b>2 PLANETARY BOUNDARY LAYER.....</b>	<b>6</b>
<b>3 RADIATIVE EFFECTS .....</b>	<b>14</b>
<b>3.1 RADIATIVE TRANSFER MODELS.....</b>	<b>14</b>
<b>3.2 DISPERSION EFFECTS.....</b>	<b>19</b>
<b>4 PARTICLE DEPOSITION .....</b>	<b>33</b>
<b>4.1 MODEL REVIEW .....</b>	<b>33</b>
<b>4.2 MODEL DEVELOPMENT .....</b>	<b>39</b>
<b>4.2.1 Bulk Canopy Model.....</b>	<b>40</b>
<b>4.2.2 Canopy Profile Model.....</b>	<b>40</b>
<b>4.2.3 LES Canopy Model .....</b>	<b>48</b>
<b>4.3 DEPOSITION UNDER CONVECTIVE CONDITIONS .....</b>	<b>48</b>
<b>5 TERRAIN EFFECTS .....</b>	<b>52</b>
<b>5.1 GENERAL REMARKS .....</b>	<b>52</b>
<b>5.2 NUMERICAL MODEL DESCRIPTION .....</b>	<b>54</b>
<b>5.3 FLOW PARAMETERS AND FORCE BALANCE .....</b>	<b>62</b>

## TABLE OF CONTENTS (Continued)

Section	Page
5.4 SURFACE FORCE RESULTS .....	65
5.4.1 Terrain Geometry Effects .....	65
5.4.2 Variation With Surface Roughness .....	74
5.4.3 Effect of Boundary Layer Stability.....	78
5.4.4 Variation With Flow Direction .....	83
5.5 SURFACE FORCE PARAMETERIZATION .....	85
5.5.1 Pressure Force.....	85
5.5.2 Tangential Stress Forces .....	92
5.5.3 Extension to Complex Terrain.....	94
5.6 TURBULENCE AND DIFFUSION .....	98
5.6.1 Velocity Variances.....	100
5.6.2 Heat and Momentum Fluxes.....	116
5.6.3 Dispersion Effects.....	121
5.7 PARTICLE DEPOSITION RATES .....	124
5.8 IMPLEMENTATION IN LATE-TIME MODELS.....	125
6 CONCLUSIONS .....	128
7 REFERENCES .....	130

## FIGURES

<b>Figure</b>		<b>Page</b>
2-1 Vertical diffusivity profiles for several combinations of surface friction velocity and convective velocity from (2.9). (a) $w_*=1\text{ms}^{-1}$ , solid line $u_*=0$ , long dash $u_*=0.5\text{ms}^{-1}$ , short dash $u_*=1\text{ms}^{-1}$ ; (b) $u_*=0.5\text{ms}^{-1}$ , solid line $w_*=0$ , long dash $w_*=0.5\text{ms}^{-1}$ , short dash $w_*=1\text{ms}^{-1}$ .....	11	
3-1 Schematic representation of solar radiative flux transfer through dusty layer. ....	15	
3-2 Particle size distribution and particle bin ranges for the calculation of radiative effects on the DICE sweep-up case. ....	20	
3-3 Initial concentration profiles from the pedestal (i.e., $z<500\text{m}$ ) of the DICE sweep-up calculation. The medium loading concentrations are shown. ....	21	
3-4 Concentration profiles after a morning release into a convective boundary layer with $2\text{ms}^{-1}$ wind speed showing the radiative effect of dust loading. Solid line is high loading, long dashes medium loading, short dashes low loading, and very short dashes for low loading case with no radiative effects.....	23	
3-5 Potential temperature profiles after a morning release into a convective boundary layer with $2\text{ms}^{-1}$ wind speed showing the effect of dust loading. Units are $^{\circ}\text{C}$ , and the line patterns are as in Figure 3-4. ....	25	
3-6 Vertical velocity variance profiles after a morning release into a convective boundary layer with $2\text{ms}^{-1}$ wind speed showing the effect of dust loading. Units are $\text{m}^2\text{s}^{-2}$ , and the line patterns are as in Figure 3-4. ....	26	
3-7 Sensible heat flux profiles after a morning release into a convective boundary layer with $2\text{ms}^{-1}$ wind speed showing the effect of dust loading. Units are $^{\circ}\text{Kms}^{-1}$ , and the line patterns are as in Figure 3-4. ....	27	

## FIGURES (Continued)

Figure	Page
3-8 Net radiative flux profiles after a morning release into a convective boundary layer with $2\text{ms}^{-1}$ wind speed showing the effect of dust loading. Units are $^{\circ}\text{Kms}^{-1}$ , and the line patterns are as in Figure 3-4. ....	28
3-9 Profile of the optical depth from the high loading case at $t=6$ hours.....	29
3-10 Concentration profiles after a noon release into a convective boundary layer with $2\text{ms}^{-1}$ wind speed showing the effect of dust loading. Concentration units are $10^{-7}\text{g/cc}$ , and the line patterns are as in Figure 3-4.....	30
4-1 Comparison between Chamberlain (1967) wind tunnel particle deposition data (symbols), Slinn (1982) model (solid line), and bulk canopy model (4.23) (dashed line). ....	41
4-2 Comparison between Chamberlain (1967) wind tunnel particle deposition data (symbols) and explicit one-dimensional canopy model (4.26) (solid line). .....	43
4-3 Assumed grass leaf area density profile for comparison with Chamberlain laboratory data, made non-dimensional by canopy height, $h$ . ....	43
4-4 Assumed leaf area density profile for three forest canopy types, made non-dimensional by canopy height, $h$ . ....	44
4-5 Profiles of mean velocity for three forest types normalized by the velocity above the canopy from Amiro (1990) compared with one-dimensional canopy model and LES. ....	46
4-6 Profiles of turbulent shear stress for three forest types normalized by the value above the canopy from Amiro (1990) compared with one-dimensional canopy model and LES. ....	46

## FIGURES (Continued)

Figure	Page
4-7 Profiles of turbulent velocity fluctuations for three forest types normalized by the value above the canopy from Amiro (1990) compared with one-dimensional canopy model and LES. ....	47
4-8 Variation of the magnitude of the average surface friction velocity with roughness length for free convection conditions. ....	49
4-9 Probability density function for the instantaneous friction velocity. (a) variation with roughness length for free convection conditions; (b) variation with geostrophic wind speed, dimensionless roughness of $10^{-4}$ except where indicated. ....	51
5-1 Schematic geometry of the horizontal and inclined channel. ....	61
5-2 Normalized mean velocity and subgrid Reynolds stress profiles from the two geometries in Figure 5-1. Solid line is the horizontal channel result, symbols indicate inclined channel. ....	61
5-3 Mean flow over 2km ridges with slope 0.5 and $z_0=1\text{m}$ . (a) mean streamlines, contour interval is $200\text{m}^2\text{s}^{-1}$ for positive values, $10\text{m}^2\text{s}^{-1}$ for negative values (shown dashed). (b) mean transverse velocity component, contour interval of $0.4\text{ms}^{-1}$ ....	67
5-4 Instantaneous flow field over 2km ridges with slope 0.5 and $z_0=1\text{m}$ . (a) flow streaklines at $\zeta=10\text{m}$ . (b) vertical velocity component at $\zeta=500\text{m}$ , contour interval of $0.6\text{ms}^{-1}$ , dashed contours denote negative values. ....	68
5-5 Time history of the domain-averaged surface forces for flow over 2km ridges with slope 0.5 and $z_0=1\text{m}$ . Forces are displayed per unit horizontal surface area and per unit fluid density. ....	69

## FIGURES (Continued)

Figure		Page
5-6	Variation of surface forces and mean boundary layer velocity with terrain slope for 2km ridges and $z_0=1\text{m}$ . (a) average pressure force ( $P_x$ ), and tangential stress forces ( $T_x, T_y$ ) per unit area. (b) mean boundary layer velocity components ( $u_B, v_B$ ).....	71
5-7	Mean streamlines for flow over a 4km ridge with slope 0.5 and $z_0=1\text{m}$ . Contour interval is $100\text{m}^2\text{s}^{-1}$ .....	72
5-8	Surface variation of the $\tau_{13}$ stress component for three terrain wavelengths with slope 0.5 and $z_0=1\text{m}$ .. —— $\lambda = 1\text{km}$ , - - - - $\lambda = 2\text{km}$ , ————— $\lambda = 4\text{km}$ .....	73
5-9	Vertical profiles of the mean velocity component normal to the ridge at the crest for three terrain wavelengths with slope 0.5 and $z_0=1\text{m}$ . The vertical scale is normalized by the inversion depth to facilitate comparison. —— $\lambda = 1\text{km}$ , - - - - $\lambda = 2\text{km}$ , ———— $\lambda = 4\text{km}$ .....	74
5-10	Variation of average surface forces with terrain wavelength for slope 0.5 and $z_0=1\text{m}$ .....	75
5-11	Surface variation of the $\tau_{13}$ stress component for three surface roughness lengths and 2km ridges with slope 0.5.. —— $z_0 = 0.01\text{m}$ , - - - - $z_0 = 0.1\text{m}$ , ————— $z_0 = 1\text{m}$ .....	76
5-12	Normalized surface force variation with roughness for flow over 2km ridges with slope 0.5. (a) tangential stress component in the $x$ -direction. (b) pressure force. Solid line and symbol is slope 0.5, dashed line and open symbol is slope 0.25.....	77
5-13	Normalized surface force variation with roughness for flow over 1km ridges with slope 0.25 and small surface heat flux, $H_0=0.0045^\circ\text{Cms}^{-1}$ .....	78

## FIGURES (Continued)

Figure	Page
5-14 Surface force variation with wavelength for flow over ridges with small surface heat flux, $H_0=0.0045^{\circ}\text{Cms}^{-1}$ , and $z_0=1\text{m}$ . Solid line and symbol is $T_x/T_{0x}$ , dashed line and open symbol is $P_x/T_{0x}$ , both for slope 0.5. Open squares are $P_x/T_{0x}$ for slope 0.25; open square with cross is $(P_x + \overline{uw}_{\text{wave}})/T_{0x}$ for slope 0.25. ....	79
5-15 Mean flow over 4km ridges with slope 0.5 and $z_0=1\text{m}$ and surface heat flux, $H_0=0.0045^{\circ}\text{Cms}^{-1}$ . (a) mean $x$ -component of velocity, contour interval of $0.5\text{ms}^{-1}$ . (b) mean vertical velocity component, contour interval of $0.1\text{ms}^{-1}$ , and potential temperature field, contour interval of $0.5^{\circ}\text{K}$ (shown as dotted lines). ....	81
5-16 Vertical profiles of horizontally-average momentum flux for the 4km ridge with slope 0.25 and low surface heat flux. Short dashes represent the subgrid component, long dash-short dash represents the contribution from resolved scale fluctuations. Solid line is the total flux, including the contribution from the steady mean flow. ....	82
5-17 Normalized surface force variation with terrain wavelength for flow over ridges with slope 0.5 and $z_0=1\text{m}$ , at low geostrophic wind speed of $2\text{ms}^{-1}$ ....	83
5-18 Mean streamlines for flow over a 4km ridge with slope 0.5 and $z_0=1\text{m}$ at low geostrophic wind speed of $2\text{ms}^{-1}$ . Contour interval is $100\text{m}^2\text{s}^{-1}$ ....	84
5-19 Variation of surface forces and mean boundary layer velocity with geostrophic wind direction for 2km ridges and $z_0=1\text{m}$ . (a) average pressure force ( $P_x$ ), and tangential stress forces ( $T_x, T_y$ ) per unit area. (b) mean boundary layer velocity components ( $u_B, v_B$ ).....	86
5-20 Mean horizontal velocity components flow over 2km ridges with slope 0.5 and $z_0=1\text{m}$ . (a) $\bar{u}$ and (b) $\bar{v}$ for geostrophic flow at $+45^{\circ}$ . (c) $\bar{u}$ and (d) $\bar{v}$ for geostrophic flow at $-45^{\circ}$ . Contour interval is $0.5\text{ms}^{-1}$ ....	87

## FIGURES (Continued)

Figure	Page
5-21 Bulk mean drag coefficient, $c_{D0}$ , for flow over flat terrain as determined from the LES calculations. Variation is shown for different roughness lengths as a function of boundary layer stability, $S_B$ .....	90
5-22 Comparison between LES results for $P_x$ and the estimate from (5.33). ....	91
5-23 Comparison between LES results for $P_x$ and the estimate from (5.34). ....	92
5-24 Comparison between LES results for (a) $T_x$ and (b) $T_y$ and the estimate from (5.35) with the stability dependent coefficient as in (5.34). ....	93
5-25 Comparison between LES results for (a) $T_x$ and (b) $T_y$ and the estimate from (5.36) with the stability dependent coefficient based on $(u_B^2 + v_B^2)^{1/2}$ .....	95
5-26 Mean $u$ -velocity for convective flow over four ridge shapes. Standard sinusoidal ridge is shown at top, and velocity contours are in $\text{ms}^{-1}$ . Geostrophic wind is $5\text{ms}^{-1}$ , the surface roughness is $1\text{m}$ .....	96
5-27 Comparison between LES pressure forces and the prediction from (5.38) for the range of terrain shapes described in Table 5-1 and the 2d-ridges in Figure 5-26.....	99
5-28 Total velocity variances (resolved + subgrid). Contour increments are $0.1\text{m}^2\text{s}^{-2}$ . Max. slope=0.25: (a) streamwise, (b) transverse, (c) vertical. Max. slope=0.5: (d) streamwise, (e) transverse, (f) vertical. ....	101
5-29 Vertical profiles of velocity variances for max. slope=0.125 at the hill crest and valley. The dashed lines are for the corresponding flat case. Both resolved and total variances are shown.....	105
5-30 Vertical profiles of velocity variances for max. slope=0.5 at the hill crest and valley. The dashed lines are for the corresponding flat case. Both resolved and total variances are shown. ....	106

## FIGURES (Continued)

Figure	Page
5-31 Vertical velocity at $\zeta = 1200\text{m}$ for max. slope=0.5. Contour intervals are $0.5 \text{ ms}^{-1}$ . Dashed contour lines indicate negative velocity.....	108
5-32 Transverse velocity at $z=50\text{m}$ for max. slope=0.5. Contour intervals are $0.5 \text{ ms}^{-1}$ .....	109
5-33 Streamwise component of vorticity for max. slope=0.5. Contour intervals are $0.005 \text{ s}^{-1}$ . (a) at $\zeta=80\text{m}$ , (b) at $x=500\text{m}$ .....	110
5-34 Stretching rate of vorticity aligned with the mean flow for max. slope=0.5. Contour increments are $5 \times 10^{-4} \text{ s}^{-1}$ .....	112
5-35 Transverse velocity at $x=500\text{m}$ , $z=40\text{m}$ as a function of time and $y$ for (a) max. slope=0.25, (b) max. slope=0.5. ....	113
5-36 Vertical profiles at $x=500\text{m}$ of total and resolved transverse velocity variance for max. slope=0.5. Solid lines: $z_0=1\text{m}$ ; long dashes: $z_0=0.1\text{m}$ ; and short dashes: $z_0=0.01\text{m}$ . ....	115
5-37 Vertical profiles at $x=500\text{m}$ of resolved and total transverse velocity variance for max. slope=0.5, $H_0=0.0045^\circ \text{Cms}^{-1}$ . The dashed lines are for the corresponding flat case. ....	116
5-38 Vertical profiles of vertical fluxes for max. slope=0.125 at the hill crest and valley. The dashed lines are for the corresponding flat case. Both resolved and total fluxes are shown. ....	117
5-39 Vertical profiles of vertical fluxes for max. slope=0.5 at the hill crest and valley. The dashed lines are for the corresponding flat case. Both resolved and total fluxes are shown. ....	119
5-40 Vertical profiles of momentum and heat fluxes for max. slope=0.5. Contour intervals are $0.05 \text{ m}^2 \text{s}^{-2}$ for momentum fluxes and $0.01^\circ \text{Cms}^{-1}$ for heat flux. (a) $u$ -momentum, (b) $v$ -momentum, (c) heat. ....	120

## **FIGURES (Continued)**

<b>Figure</b>	<b>Page</b>
5-41 Particle dispersion over 1 hour from a localized release in convective flow over periodic ridges. maximum terrain slope is 0.5, and geostrophic wind is $5\text{ms}^{-1}$ in the $x$ -direction.....	122

## TABLES

<b>Table</b>		<b>Page</b>
3-1	Extinction optical depth for 1km dust layer at uniform concentration.....	19
3-2	Transmitted / absorbed fraction for dust layer.....	19
5-1	Forces for complex terrain shapes.....	97
5-2	Deposition velocity for 10 $\mu\text{m}$ particles over terrain.....	125

# **SECTION 1**

## **INTRODUCTION**

### **1.1 BACKGROUND.**

The fate of dust particles injected into the atmosphere by nuclear explosion has been studied extensively. Most of the studies have concentrated on high altitude effects, where small particles can persist for extended periods with possible climatic impact. Long range radioactive fallout calculations are also principally concerned with atmospheric dispersion phenomena in the upper atmosphere. However, there are a number of applications where the evolution of the dust cloud near the ground is of interest. For example, aircraft missions include extensive flight periods at low altitude, exposing the aircraft to persistent degradation in the near-surface environment. The cumulative effects of exposure to relatively small concentrations of dust are particularly significant, since this can cause engine failure or impair visibility through transparent surfaces. The possibility of accumulated damage over long flightpaths demands the study of the late-time evolution of the dust field, since smaller particles can remain aloft for many hours.

Large masses of dust can be lofted into the atmosphere by a nuclear blast, and there are two major paths for the dust to appear at low levels. First, particles in the main cloud, which can rise many kilometers, will fall out under gravitational acceleration and pass through low levels at some later time. This is the pathway for much of the radioactive fallout and has been studied previously. However, a more persistent threat is posed by the high density pedestal, formed by dust which is lifted from the surface but is not carried upward with the main cloud. The fate of a pedestal particle depends on many factors, both its own size and density, and also meteorological and terrain factors.

The region near the ground surface is often turbulent, forming the planetary boundary layer, which usually extends on the order of 1000m in the vertical. The flow in the boundary layer is influenced by surface processes, including heat and moisture fluxes and turbulent drag on the surface. These processes induce turbulent motions within the boundary layer, and depend on the surface conditions as well as the solar and infra-red

radiative fluxes. The turbulent mixing in the planetary boundary layer can maintain small particles in suspension, while surface features can augment the gravitational deposition process by absorbing particles. In addition, cloud precipitation processes can scavenge the dust from the atmosphere. All these processes depend on the size and type of dust particle, and therefore the initial pedestal formation is critical, since this will depend on soil or surface type as well as the burst type. It is clear that any assessment of low-level dust hazard requires a reliable description of both the pedestal generation mechanism and the late-time boundary layer dispersion and deposition mechanisms.

Current late-time cloud models have not devoted much effort to the near-surface dust. The objective of the research reported here is the development of algorithms to allow the late-time cloud models to describe the late-time processes of turbulent diffusion and deposition in the planetary boundary layer.

## 1.2 PHYSICAL MECHANISMS.

Much attention has been paid to the lofted dust cloud from a nuclear burst, which can carry material up to the stratosphere where it will persist for a very long time. In addition to the main cloud, however, there can also be a significant 'pedestal' of dust swept up from the surface by the initial blast wave, and also by the inflow feeding the rising fireball. There is a potentially large mass of dust lofted only into a shallow (< 100m deep) layer near the surface, which does not become entrained into the rising cloud, and therefore remains close to the surface when only burst-induced dynamics are considered. Following decay of the burst flow field, however, the ambient atmospheric flow effects will begin to dominate and control the low-level dust evolution. The following sections discuss the various phenomena occurring in the boundary layer which affect the concentration of near-surface dust.

### 1.2.1 Turbulent Diffusion.

The atmosphere near the surface of the Earth is usually in turbulent motion. The wind blowing over the rough surface, and the buoyancy effects of daytime surface heating produce turbulent vertical motions that mix airborne material both vertically and horizontally. The surface-generated turbulent layer is often capped by a stable temperature inversion, which marks the vertical extent of the mixing and is formed as the

turbulent boundary layer grows upward into the stably-stratified atmosphere. The depth of the mixing region can vary with meteorological conditions and time of day, but usually reaches between about 500m and 2000m during the daytime. Shallower layers are associated with reduced heating, due to the presence of cloud, for example, or due to large scale subsidence overlying air. Under nocturnal cooling conditions, the surface layer becomes stably-stratified and the mixing depth and turbulence intensities are reduced.

Vertical mixing can play an important role in the late-time dispersion of dust clouds, as demonstrated by Sykes, Parker and Henn (1993). Daytime turbulent velocity fluctuations are on the order of  $1\text{ms}^{-1}$ , and can therefore dominate the vertical transport of particles with gravitational settling speeds smaller than this. Thus, particles smaller than about  $30\mu\text{m}$  will be strongly affected by the mixing and can remain aloft for much longer than under quiescent conditions. Many schemes have been proposed to represent the diffusion processes in the atmospheric boundary layer, and appropriate methods for late-time dispersion modeling will be discussed in Section 2, and the radiative effects of a dust cloud on the turbulent boundary layer are considered in Section 3..

### **1.2.2 Dry Deposition.**

The absorption of a contaminant substance at the surface is known as dry deposition. Dry deposition can include moisture effects, but is distinguished from the direct deposition of dust in precipitation such as rain or snow. The process is complex and is controlled by a number of mechanisms. Idealized relationships have been established for massless scalar contaminants in terms of the surface conditions but these relationships are not directly applicable to the dust particle deposition. The finite-size particles do not precisely follow the air flow and they do not diffuse with the same molecular diffusivity as a scalar contaminant such as a trace gas. The deposition is usually modeled in terms of a sum of resistances for each of the various processes, such as turbulent transfer or molecular diffusion; a rapid transfer rate is represented by a low resistance. Two general types of surface are considered, a smooth surface and a vegetative canopy.

In the atmospheric context, a smooth surface is represented by surfaces such as desert sand or snow. The surface conditions are obtained from the assumption that particles which impact the surface will stick. The flux of material on to the surface

therefore depends on the rate of impact. Very small particles tend to follow the air around surface features, while large particles simply fall rapidly to the ground. Intermediate sizes will be unable to follow the air around small surface features and will be deposited on those features. Small particles can also reach the surface by Brownian motion if they are brought sufficiently close. The deposition is therefore governed by the particle response time, the turbulence acceleration rates, the scale of the surface features, and the Brownian diffusion rate.

A vegetative canopy is distinguished by its three-dimensional nature, i.e., there is a significant flow *through* the canopy. A surface covered by trees in full leaf can provide a large particulate flux onto the surface, since the dust in the canopy layer will be swept past a vast number of individual leaves greatly increasing the chance of impact. The actual deposition process is extremely complex, reflecting the microstructure of the leaf structure of the various species in the canopy. The flux also depends on the rate of which the air sweeps past the leaves, and this is controlled by the drag effects of the canopy. It is well-known that a dense canopy reduces the wind speed, so all these effects need to be modeled if we are to determine the fate of low level dust.

Representations of the deposition process will be discussed in Section 4.

### **1.2.3 Wet Deposition and Scavenging.**

The condensation of water vapor into liquid droplets or frozen ice particles introduces a new range of mechanisms for dust removal. The basic phenomenon requires the incorporation of the dust particle into a water/ice droplet, which can then fall to the ground and remove the dust from the atmosphere. The mechanisms for coalescence are manifold, including collision impact, nucleation, molecular diffusion, electrical effects, or phoretic effects due to local gradients of molecular properties.

The precipitation scavenging process involves hydrometeors falling through the dusty boundary layer, collecting dust particles and depositing them on the surface. In general, the scavenging mechanisms is very efficient in removing small particles, so that a heavy rain can 'clean' the boundary layer relatively quickly (Schwartz, 1992). The collection efficiency does depend on the relative sizes of the dust and the precipitation, and is different for different types of precipitation, e.g. rain, snow, hail.

In general, we do not expect the meteorological input to late-time dispersion models to contain information on precipitation rates. Precipitation is difficult to predict and is usually very intermittent. It is therefore inappropriate to attempt a detailed representation of the microphysical processes involved in precipitation scavenging, and a much simpler approach is recommended. If the meteorological input contains information on the precipitation fields, then the precipitation fall speed can simply be added to the particle fall speed. This assumes a perfectly efficient collection mechanism, i.e., every dust particle is immediately attached to a droplet, but there is evidence that small particles are indeed collected efficiently, and large particles will already have a significant fall speed. At present, this simple treatment of precipitation scavenging is all that can be justified in light of the available meteorological information.

#### **1.2.4 Terrain Effects.**

The earth's surface is generally non-uniform, with changes in surface type and elevation on all scales. The processes described in the previous sections are all local phenomena, and will respond to local features such as hills or forests. Changes in surface roughness, e.g., wheat field to forest, are generally significant only near the surface and can be modeled using purely local analysis, although the non-equilibrium situations in regions of such change can result in large effective deposition rates. For example, the wind speed takes some time to slow down after entering a forest canopy and there is greatly enhanced deposition in the forest edges where the winds are higher than equilibrium.

In contrast to land use variations, topographic features induce large changes in the entire boundary layer and therefore require more careful study. One of the main effects of topography is to cause the near-surface wind to speed up over the hill tops. This can increase dry deposition in these regions, and this may not be balanced by a corresponding decrease in the valley regions. The hills also affect the boundary layer turbulence, modifying the rate at which dust is diffused vertically.

The representation of complex terrain effects is discussed in Section 5.

## SECTION 2

### PLANETARY BOUNDARY LAYER

One of the most important mechanisms operating near the surface of the earth is turbulent diffusion. Mechanical generation of turbulence by surface roughness elements such as forests, and buoyant generation from surface heating during daytime conditions over land, produces a turbulent boundary layer that mixes pollutants throughout its depth. This planetary or atmospheric boundary layer, often referred to as the PBL, has been studied extensively from the point of view of pollutant dispersion, and many of its properties are now well known. There are many references covering the structure and dynamics of the planetary boundary layer, and its dispersion properties. Detailed descriptions can be found in Lumley and Panofsky (1964), Csanady (1973), Pasquill (1974), Panofsky and Dutton (1984), and Wyngaard and Venkatram (1988).

The atmospheric boundary layer over land typically undergoes a strong diurnal variation, with nocturnal cooling of the surface suppressing turbulent activity at night. Surface heating from solar radiation warms the lower layers of the atmosphere in the morning and the turbulent mixing layer deepens. The growth is rapid during the morning transition hours but slower through the rest of the day. The mixing depth typically ranges from 500m to 2000m, depending on local conditions, and turbulent eddy velocities are often a few meters per second. The inversion-capped situation, where the mixed layer depth is limited by an overlying stably-stratified air mass, is very common. The weather under such conditions can be clear skies, shallow cumulus clouds, or a low-level stratus deck. Deep convection conditions represent a breakdown of the surface boundary layer, with low-level air being carried high into the troposphere by the convective cells. In some sense, one can consider the entire troposphere to be part of the boundary layer under these conditions.

The turbulence conditions in the PBL are classified by the relative importance of buoyancy generation, i.e. stable, neutral , or unstable. In unstable conditions, the heating of the surface is the dominant process, causing surface air to rise in turbulent convection eddies through the boundary layer, while stable conditions occur during nocturnal cooling conditions and the mixing process expends energy lifting the heavier surface air. Neutral conditions are shear-dominated, i.e. high wind speeds or very small buoyancy effects, and

turbulence profiles are similar to those found in wind-tunnel boundary layers. The buoyancy effects are characterized by the Monin-Obukov length,  $L$ , and the mixing or boundary layer depth,  $z_i$ . The Monin-Obukov length is the height at which the buoyancy generation of turbulence equals mechanical generation, and therefore provides the appropriate scale for distinguishing between the two mechanisms. A similarity theory for the surface layer has been constructed in terms of  $z/L$ , providing a description of the profiles of various mean quantities. The atmosphere introduces other complicating factors, such as the Coriolis effects due to the Earth's rotation which produce a turning of the wind direction with height known as the Ekman profile. Also moisture transport and condensation effects can release energy in the cloud layer, and modify the turbulence profiles.

Our main purpose in determining the structure of the PBL is the characterization of the mean boundary layer transport and the turbulent diffusion rates. This is accomplished by means of parameterization schemes, i.e., the boundary layer is defined by a small number of parameters, from which the mean flow and diffusion rates can be deduced. The most important parameters for the PBL are

- a) the geostrophic, or free stream velocity,  $U_0$
- b) the surface roughness height,  $z_0$
- c) the surface heat flux,  $H_0$
- d) the boundary layer depth,  $z_i$

These parameters can be used to derive two important velocity scales that define the turbulence levels in the PBL. The first is the surface friction velocity,  $u_*$ , which is defined by the relation

$$\tau_s = \rho_a u_*^2 \quad (2.1)$$

where  $\tau_s$  is the average surface stress, and  $\rho_a$  is the air density. The surface stress depends on the atmospheric stability as well as the surface roughness and free-stream wind speed. We shall discuss the relationship further below.

The second velocity scale characterizes the buoyancy effects, and is known as the convective velocity scale (Deardorff, 1970),  $w_*$ . The definition is

$$w_* = \left( \frac{g}{T_0} H_0 z_i \right)^{1/3} \quad (2.2)$$

and is related to the Monin-Obukov length,

$$L = \frac{u_*^3}{k \frac{g}{T_0} H_0} \quad (2.3)$$

through the equation

$$\frac{z_i}{L} = \frac{k w_*^3}{u_*^3} \quad (2.4)$$

Here,  $k$  is von Karman's constant, which is usually assumed to be 0.4,  $g$  is the gravitational acceleration, and  $T_0$  is a reference temperature for the Boussinesq approximation.  $H_0$  is actually specified as a temperature flux in the above equations, and the relative density flux is then obtained after division by  $T_0$ , which should represent an average temperature for the boundary layer.

Before discussing the determination of  $u_*$  and  $w_*$ , we consider the representation of the turbulent diffusion. Our approach to this problem has been based on second-order closure techniques, which provide an estimate of the diffusion rates in terms of velocity fluctuation correlations. This is a more general and systematic approach than empirical schemes based on curve-fitting experimental dispersion results, but requires the specification of the velocity fluctuation statistics.

The two simplified situations, where profiles are well understood, are provided by neutral conditions and free convection conditions. In neutral flow, the surface heat flux is zero, or at least is negligible in comparison with the mechanical shear effects. The turbulence is characterized by  $u_*$  only in this situation. Free convection occurs under very light wind conditions with a positive surface heat flux, and the turbulence is therefore dependent on  $w_*$  only.

We represent the turbulence velocity correlations as

$$\overline{u'_i u'_j} = u_*^2 F_{ij} \left( \frac{z}{z_i} \right) \quad (2.5)$$

for neutral conditions, and

$$\overline{\bar{u}'_i \bar{u}'_j} = w_*^2 G_{ij} \left( \frac{z}{z_i} \right) \quad (2.6)$$

for free convection. Here, the overbar denotes an average value and the prime denotes a fluctuation from the average.

Neutral profiles are relatively simple linear functions. Wind tunnel studies of the aerodynamic boundary layer (Klebanoff, 1955; Townsend, 1976), and numerical calculations of the neutral Ekman layer (Spalart, 1989, Mason and Thompson, 1987) both support velocity variance profiles proportional to  $(1 - z/z_i)$ . Appropriate dimensionless profiles are

$$\begin{aligned} F_{11} &= 5(1 - z/z_i) \\ F_{22} &= 2.5(1 - z/z_i) \\ F_{33} &= 1.5(1 - z/z_i) \end{aligned} \quad (2.7)$$

Free convection profiles are available from the laboratory experiments of Deardorff (1970), and LES calculations (Mason, 1989; Schmidt and Schumann, 1989), and a reasonably good representation is provided by the expressions

$$\begin{aligned} G_{11} = G_{22} &= 0.13(1 + 1.5e^{-z/z_i}) \\ G_{33} &= 1.1\left(\frac{z}{z_i}\right)^{2/3}(1.05 - z/z_i) \end{aligned} \quad (2.8)$$

These representations approximate the turbulence profiles under the idealized conditions, and the value for general conditions can be estimated as the sum of the two components. For stable conditions, the convective velocity scale is zero and the neutral profile shape is used. However, the surface friction velocity will generally be reduced by the presence of stable stratification near the surface, and the boundary layer depth,  $z_i$ , is estimated as  $5L$ .

The vertical diffusivity,  $K_t$ , can be estimated from the turbulence profiles using the equilibrium version of the second-order closure equations (Lewellen, 1977). This gives

$$K_t = \frac{\Lambda}{Aq} \frac{\left(\overline{w'^2} + \frac{g}{T_0} \frac{\Lambda}{q} \frac{\overline{w'\theta'}}{bs}\right)}{1 + \frac{1}{2Abs} \frac{g}{T_0} \frac{\Lambda^2}{q^2} \frac{\partial \theta}{\partial z}} \quad (2.9)$$

where  $q^2 = \overline{u'_i u'_i}$ , and  $\theta$  is the potential temperature. The heat flux profile can be represented as a linear function

$$\overline{w' \theta'} = H_0 \left( 1 - \frac{z}{z_i} \right) \quad (2.10)$$

and the turbulence length scale is modeled very simply as

$$\frac{1}{\Lambda^2} = \frac{1}{(0.3z_i)^2} + \frac{1}{(0.65z)^2} \quad (2.11)$$

providing a transition from the linear behavior near the surface to a constant value in the mixed layer. The turbulence model constants,  $A$ ,  $b$ , and  $s$ , take the values 0.75, 0.125, and 1.8, respectively.

The potential temperature gradient,  $\frac{\partial \bar{\theta}}{\partial z}$ , can be assumed to be zero for neutral and convective conditions, since the temperature is well-mixed except in a thin superadiabatic layer at the surface. For stable conditions, the potential temperature gradient must be estimated separately.

Several examples of the vertical diffusivity profiles from (2.9) are shown for different values of  $u_*$  and  $w_*$  in Figure 2-1. The profiles are made dimensional by assuming an inversion depth of 1000m. The profile shape shows an elevated maximum, since  $K_t$  goes to zero at the ground, where the length scale vanishes, and at the inversion, where the turbulence levels are low. For free convection conditions,  $u_*=0$ , the diffusivity profile is in good agreement with the values obtained by Wyngaard and Brost (1984) from Large-Eddy Simulations; the simplified representation (2.9) is not able to reproduce the asymmetry between upward and downward diffusion, but the predicted magnitude is representative of the average value. The profiles show an interesting variation as the wind shear is increased from the free convection situation with no wind. The diffusivity is initially reduced as  $u_*$  increases, in spite of the fact that the turbulence intensities are additive in (2.9) and therefore must monotonically increase with  $u_*$ . This anomalous behavior in the diffusivity is actually observed in the Large-Eddy Simulations of Mason (1992), where it is attributed to the reduction in turbulence scale in the presence of wind shear. We do not modify the definition of  $\Lambda$  in our simple parameterization, but the reduction in  $K_t$  is due to a reduction in the turbulence timescale,  $\Lambda/q$ , which reduces the contribution from the heat flux term in (2.9). It is encouraging that the closure model prediction reproduces this observed shear phenomenon.

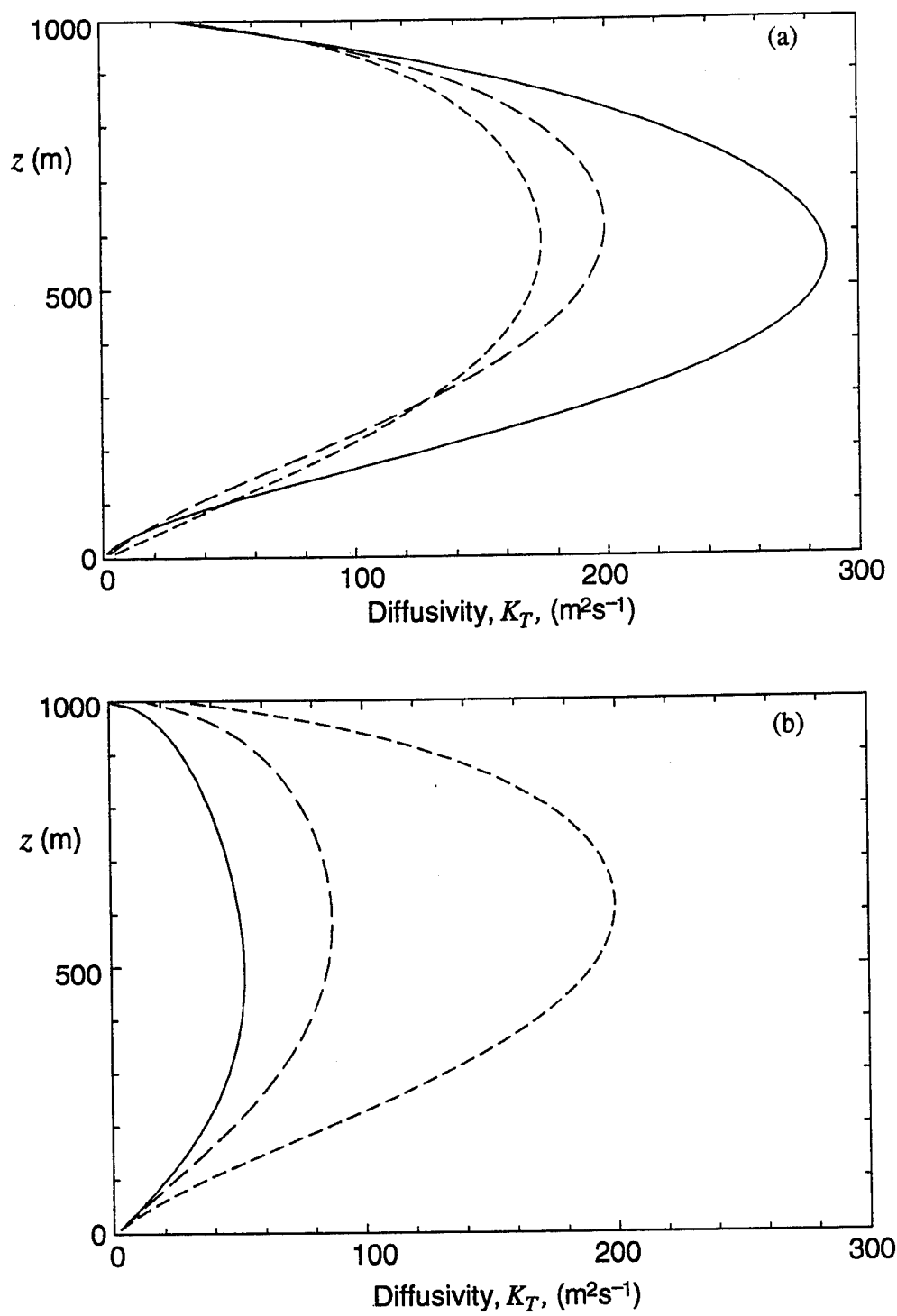


Figure 2-1. Vertical diffusivity profiles for several combinations of surface friction velocity and convective velocity from (2.9). (a)  $w_* = 1 \text{ ms}^{-1}$ , solid line  $u_* = 0$ , long dash  $u_* = 0.5 \text{ ms}^{-1}$ , short dash  $u_* = 1 \text{ ms}^{-1}$ ; (b)  $u_* = 0.5 \text{ ms}^{-1}$ , solid line  $w_* = 0$ , long dash  $w_* = 0.5 \text{ ms}^{-1}$ , short dash  $w_* = 1 \text{ ms}^{-1}$ .

The turbulence and diffusion parameterizations discussed above are predicated on the ability to specify the boundary layer parameters,  $u_*$  and  $w_*$ . In many cases, these parameters will not be available from the meteorological input data, which might consist of a number of wind observations or a gridded three-dimensional wind field. Many dispersion modelers have faced the difficulty of characterizing the PBL using routine observational data, and there are therefore several schemes in existence to perform this task. For example, the CRDEC dispersion model NUSSE (Saucier, 1987) contains algorithms to determine the PBL turbulence levels. However, we have previously used the more general scheme incorporated into METPRO (Paine, 1987), which is the meteorological preprocessor developed for the U.S. Environmental Protection Agency. METPRO is an extension of PREPRO (Paine and Hanna, 1986), which was developed for the Electric Power Research Institute as part of the Plume Model Validation and Development program.

The details of the mathematical modeling in METPRO can be found in the cited reference, but a brief outline of the methodology is provided here. The two surface parameters, characterizing the momentum and heat fluxes, are obtained from a surface layer analysis using the Monin Obukov similarity theory. The surface layer description requires a surface roughness value. Given the wind speed at a reference height, the friction velocity,  $u_*$ , can be obtained if the Monin Obukov length,  $L$ , defined in (2.3), is known. This requires knowledge of the surface sensible heat flux, which is derived from a surface energy balance, if no micrometeorological thermodynamic information is provided. If detailed temperature profile data is available, then surface layer similarity theory can be used to estimate the flux

The surface energy balance is determined by the incident solar radiative flux, the soil heat flux, and the turbulent heat and moisture fluxes into the air. The surface moisture flux is an important practical consideration since a large fraction of the incident radiative heating can be used to provide the latent heating necessary to evaporate water from the surface. This is true not only over open water surfaces, but also over vegetative canopies. The ratio of the sensible heat flux to the latent heat flux in the moisture is known as the Bowen ratio. METPRO estimates the incident radiative flux from the solar elevation angle, which is a function of latitude, time of day and time of year. The flux reaching the ground is reduced by a factor dependent on the cloud cover, if this is available from the observations. The relative magnitude of the soil flux and turbulent

heat and moisture fluxes is based on a parameterization of the soil/canopy moisture content.

## SECTION 3

### RADIATIVE EFFECTS

#### 3.1 RADIATIVE TRANSFER MODELS.

As discussed in the previous section, the structure of the PBL is strongly affected by the surface heat flux, which is largely determined by the incoming solar radiation during the daytime. It is clear that the radiation at the surface depends on natural cloud cover, so we must consider the possibility that a dust cloud might also modify the local boundary layer through changes in the solar radiation reaching the ground.

As a preliminary assessment of the radiative transfer properties of a dust-laden layer, we consider an idealized homogeneous situation. Suppose we have a 1km deep layer of monodisperse dust particles of diameter,  $d$ , and mass concentration of  $c$ . The dusty atmosphere is both an absorbing and a scattering medium for the solar radiation, and we wish to estimate the relative fractions of the solar energy that are reflected back to the sky,  $f_r$ , absorbed by the dust,  $f_a$ , or transmitted through to the surface,  $f_t$ . The incident radiative flux is  $F_0$  at an angle  $\theta_0$  to the vertical, and the surface albedo is  $\alpha_s$ , as illustrated schematically in Figure 3-1. We assume that the clear air is completely transparent for the purposes of a simple calculation. The latter assumption makes the vertical location of the dust layer irrelevant, since radiation is transmitted without loss above and below the layer. Conservation of energy requires that

$$f_a + f_t(1 - \alpha_s) + f_r = 1 \quad (3.1)$$

i.e., the total input from the sun is either absorbed by the dust or the ground, or is reflected back upward. All the quantities discussed in this section refer to broadband averages over the entire spectral region covering the solar flux. A detailed treatment of the spectral variability of the particle properties is beyond the scope of this study, which should be regarded as a bulk parameterization suitable for practical calculation.

Individual particle properties are characterized by a single scattering albedo,  $\omega_0$ , and a scattering phase function,  $P(\mu, \mu')$ , where  $\mu$  and  $\mu'$  represent the incident and scattering directions, respectively. The albedo specifies the fraction of incident energy

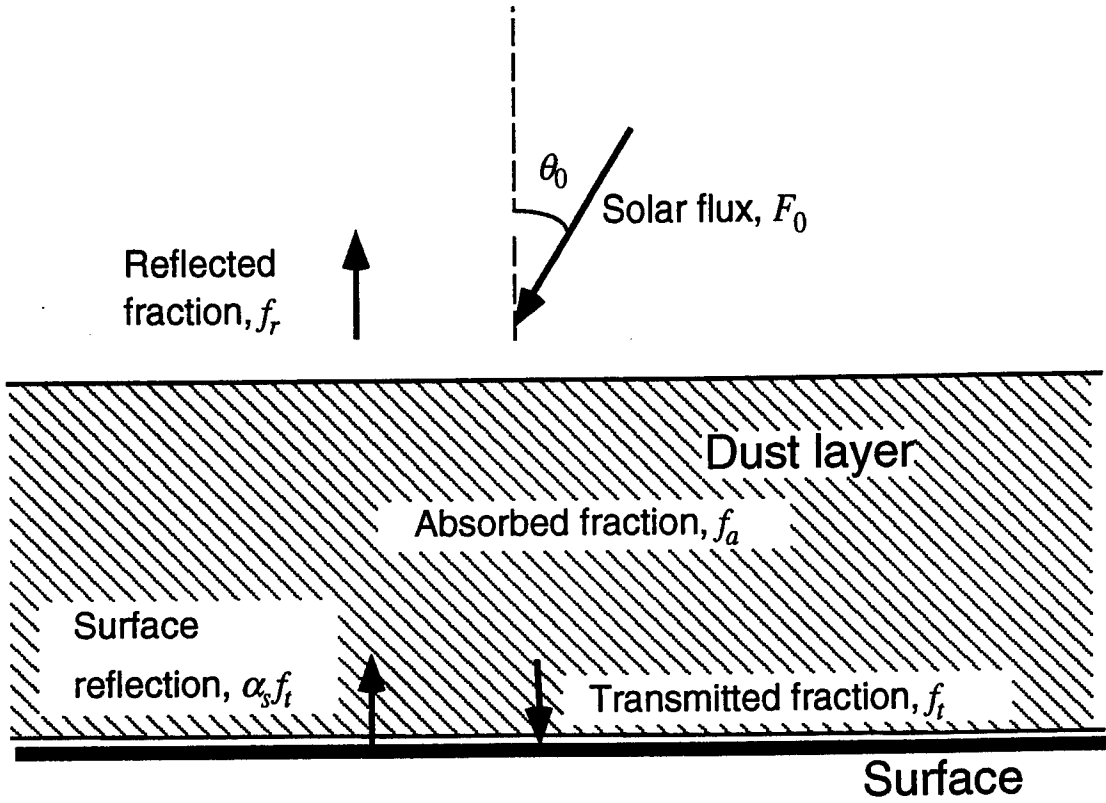


Figure 3-1. Schematic representation of solar radiative flux transfer through dusty layer.

scattered by an individual particle, while the phase function gives the directional dependence of the scattered wave function. For a plane incident wave encountering a horizontally homogeneous scattering medium, the radiative intensity,  $I$ , satisfies the transfer equation

$$\mu \frac{dI}{d\tau} = -I + \frac{\omega_0}{2} \int_{-1}^{+1} d\mu' P(\mu, \mu') I(\tau, \mu') \quad (3.2)$$

where  $\tau$  is the optical depth, and the integral extends over all scattering directions, with  $\mu$  and  $\mu'$  equal to the cosine of the angle between the wave direction and the vertical. The optical depth of the layer is defined as

$$\tau = \int \pi \frac{d^2}{4} K_{ext} N dz \quad (3.3)$$

(Friedlander, 1977) where  $d$  is the particle diameter,  $N$  is the number density, and  $K_{ext}$  is the particle extinction efficiency (sometimes called the attenuation coefficient or turbidity). The extinction efficiency includes both scattering and absorption effects of the particles and depends on the radiation wavelength, but for short waves relative to the particle diameter, Mie theory gives  $K_{ext} = 2$ . This assumption is valid for solar radiation, which peaks around  $0.5\mu\text{m}$  wavelength, interacting with particles larger than  $1\mu\text{m}$  and will be used for all our subsequent calculations. The quantity  $\tau$  is sometimes referred to as the geometric or extinction optical depth, and should not be interpreted as a measure of the absorption in the layer. A proper calculation of the radiative transfer requires treatment of the scattering effects and will be discussed below. The constant efficiency gives a simple relation between the optical depth and the mass concentration of dust particles. If we have a mass loading,  $c$  per unit volume, over a layer of depth  $H$ , then the optical depth of the layer is

$$\tau = \frac{3cH}{\rho_d d} \quad (3.4)$$

where  $\rho_d$  is the particle material density.

The full radiative transfer problem is still extremely complex, even neglecting the wavelength dependence, since a real dust layer involves multiple scattering as radiation encounters many particles in passing through the layer. Each encounter involves the phase function, and a proper treatment requires a sophisticated Monte-Carlo calculation of the multiple interaction or an equivalent technique. We seek a simplified treatment that provides a direct estimate of radiative transfer for the multiple scattering regime.

From a survey of the atmospheric radiation literature, the delta-Eddington two-stream model was selected as the most appropriate for this application (Joseph et al., 1976). This model is an extension of the Eddington model of Shettle and Weinman (1970) to account for strong directional asymmetry that is typically found in particulate scattering. Two-stream models represent the net vertical flux of broadband radiation as a sum of upward,  $F^\uparrow$ , and downward,  $F^\downarrow$ , fluxes. This approximation is suitable for quasi-homogeneous situations in the horizontal direction. The delta-Eddington model approximates the scattering phase function by a delta function in the forward direction, plus a single spherical harmonic, i.e.,

$$P(\mu, \mu') = 2f\delta(\mu - \mu') + (1 - f)(1 + 3g'\mu\mu') \quad (3.5)$$

where  $f$  is the fractional scattering into the forward direction, and  $g'$  is the asymmetry factor of the continuous part of  $P$ . These two quantities can be defined in terms of the overall asymmetry factor,  $g$ , giving

$$f = g^2 \quad (3.6a)$$

$$g' = \frac{g}{1+g} \quad (3.6b)$$

The Eddington approximation assumes that the radiance can be represented as

$$I(\tau, \mu) = I_0(\tau) + \mu I_1(\tau) \quad (3.7)$$

i.e., an expansion of the directional dependence in spherical harmonic functions with truncation at first order. These simplifying assumptions for the phase function and the radiance allow an analytic integration over all forward and backward scattered directions, as required for the two-stream approximation, to give

$$F^\uparrow = \pi \left( I_0(\tau) - \frac{2}{3} \mu I_1(\tau) \right), \quad F^\downarrow = \pi \left( I_0(\tau) + \frac{2}{3} \mu I_1(\tau) \right) \quad (3.8)$$

The expressions for  $I_0$  and  $I_1$  within the layer are from Shettle and Weinman (1970),

$$I_0(\tau) = C_1 e^{-k\tau'} + C_2 e^{+k\tau'} - \alpha e^{-\tau'/\mu_0} \quad (3.9a)$$

$$I_1(\tau) = p(C_1 e^{-k\tau'} - C_2 e^{+k\tau'}) - \beta e^{-\tau'/\mu_0} \quad (3.9b)$$

where

$$k = [3(1-\omega')(1-g'\omega')]^{1/2}$$

$$p = [3(1-\omega')/(1-g'\omega')]^{1/2}$$

$$\alpha = 3\omega' F_0 \mu_0^2 [1 + g'(1-\omega')] / 4(1-k^2 \mu_0^2)$$

$$\beta = 3\omega' F_0 \mu_0 [1 + 3g'(1-\omega')\mu_0^2] / 4(1-k^2 \mu_0^2)$$

where  $\mu_0 = \cos(\theta_0)$ . These expressions are identical to the standard Eddington approximation but use modified definitions of the optical depth and scattering albedo to account for the delta-function component of the phase function, defined as

$$\tau' = (1-\omega_0 f) \tau \quad (3.10a)$$

$$\omega' = \frac{(1-f)\omega_0}{(1-\omega_0 f)} \quad (3.10b)$$

and the coefficients  $C_1$  and  $C_2$  are obtained from the boundary conditions on the radiance, which are

$$F^\downarrow = F_0 \mu_0 \text{ at the upper boundary}$$

$$F^\uparrow = \alpha_s F^\downarrow \quad \text{at the ground}$$

The expressions can be generalized to a multi-layer situation by demanding continuity of the fluxes across each layer interface to obtain a coupled set of equations for the coefficients within each layer (Shettle and Weinman, 1970).

A preliminary estimate of the effect of dust loading on the solar radiation was obtained from a single layer calculation using a homogeneous, monodisperse particulate concentration over a 1km deep layer. The optical depth for a series of particle sizes and concentration levels typical of single and multiple cloud pedestals is shown in Table 3-1, and it is clear that small particles can exist at sufficiently high number density in the pedestal of nuclear clouds to produce a significant optical depth. The quantitative radiative effects are calculated using the delta-Eddington model, which requires an estimate of single scattering albedo and asymmetry factor for dust. A typical value of  $\omega_0$  for pedestal dust is 0.8, lying between the value for soot particles, which is around 0.4, and that for non-carbon dust particles, which have a scattering albedo of roughly 0.95 (Tsay et al., 1991). The asymmetry factor,  $g$ , was taken to be 0.5 for the dust particles; an accurate value is not available but the results are not very sensitive to  $g$ .

Using  $\omega_0 = 0.8$ ,  $g = 0.5$ , and  $\alpha_s = 0$ , the values of transmitted and absorbed fraction for an incident vertical solar flux through a range of optical depths covering Table 3-1 are given in Table 3-2. The transmitted fraction is the fraction of incident flux passing through the dust layer and reaching the ground, and the absorbed fraction is the amount of radiation absorbed within the dust layer which will cause the layer to heat up. The remaining fraction is reflected back from the top of the dust layer. Table 3-2 shows that for optical depths greater than unity, the transmitted flux is greatly reduced below the incident value, and that the bulk of the radiation is absorbed by the dust layer. Thus, a 1km layer of  $10\mu\text{m}$  particles at a concentration of  $10^{-7}\text{g/cc}$  would virtually extinguish the radiative flux at the surface, with only 4% of the solar flux being transmitted, while 79% of the solar radiation would be absorbed within the dust layer itself. These changes in the solar heating effects would dramatically alter the atmospheric boundary layer structure and the vertical mixing rates.

**Table 3-1. Extinction optical depth for 1km dust layer at uniform concentration.**

Concentration	$10^{-9}$ g/cc	$10^{-8}$ g/cc	$10^{-7}$ g/cc
$d = 100\mu\text{m}$	0.0066	0.066	0.66
$10\mu\text{m}$	0.066	0.66	6.6
$1\mu\text{m}$	0.66	6.6	66.6

**Table 3-2. Transmitted / absorbed fraction for dust layer.**

Optical depth	0.066	0.2	0.66	1	2	4	6.6	66.6
Transmitted, $f_t$	0.98	0.93	0.78	0.68	0.43	0.16	0.04	0.00
Absorbed, $f_a$	0.01	0.04	0.14	0.22	0.42	0.67	0.79	0.83

### 3.2 DISPERSION EFFECTS.

In order to assess the dynamic effects of the absorption of solar radiation in a dust-laden boundary layer, we extended the turbulence model described by Sykes, Parker and Henn (1993, Chapter 4) for calculating the evolution of a spectrum of dust sizes in the atmospheric boundary layer. A multi-layer version of the delta-Eddington scheme was added to the one-dimensional turbulence closure model, and the radiative flux divergence was included in the mean temperature equation as a local heating term. The net radiative flux

$$F_N = F^\uparrow - F^\downarrow$$

and the heating rate is computed from the flux divergence as

$$\frac{1}{\rho c_p} \frac{\partial F_N}{\partial z}$$

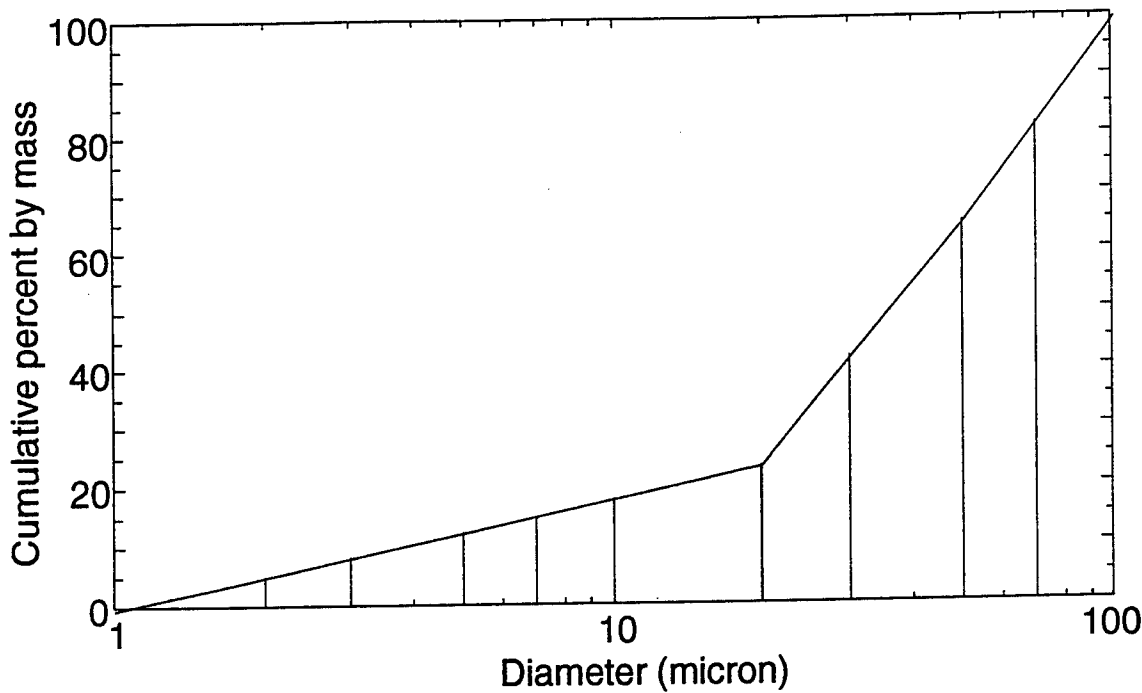


Figure 3-2. Particle size distribution and particle bin ranges for the calculation of radiative effects on the DICE sweep-up case.

The model was initialized with the pedestal dust distribution from a high-resolution DICE calculation of the sweep-up layer at  $t=5\text{min}$ . from a 1 megaton (MT) burst at a scale height of  $200 \text{ ft}/kT^{1/3}$ . The horizontally-integrated DICE loading profile must be scaled to produce the desired concentration distribution, and three arbitrary levels were chosen to examine the boundary layer response. The assumed particle size distribution is shown in Figure 3-2, with the 10 size bins indicated by the vertical lines. The dust distribution for the medium loading level is shown in Figure 3-3, with each line corresponding to the cumulative mass in increasing size bins, i.e., the left-most line represents the concentration in the lowest bin, while the right-most line represents the total over all bins. The calculation uses only the lowest 500m of the dust profile, as was used in Figure 4-9 of Sykes, Parker and Henn (1993). The low and high loading cases are obtained from the medium loading by reducing and increasing the concentrations by a factor of 10, respectively. The optical depth is computed as a sum over the various size bin contributions, i.e.,

$$\tau = \frac{3}{\rho_d} \int \sum_{\alpha} \frac{c_{\alpha}}{d_{\alpha}} dz \quad (3.11)$$

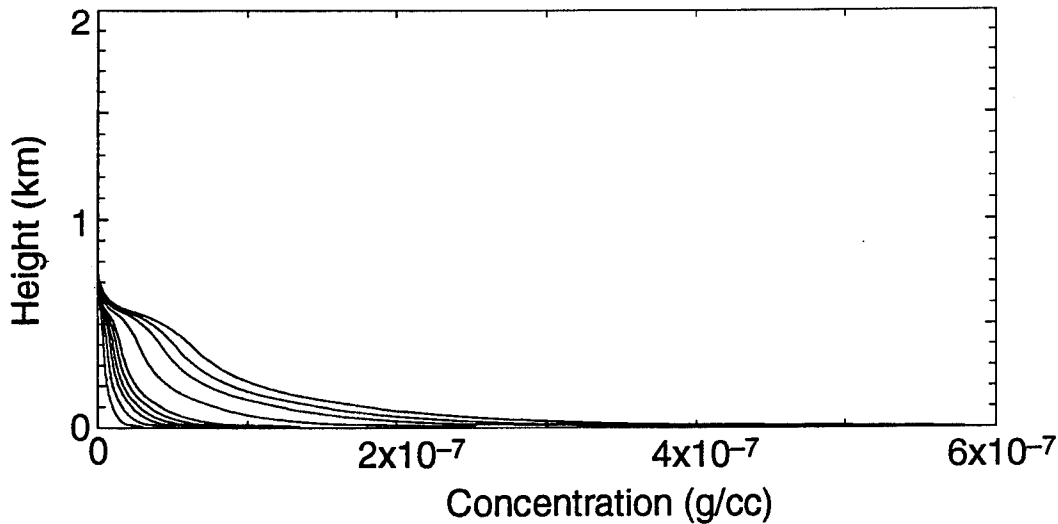


Figure 3-3. Initial concentration profiles from the pedestal (i.e.,  $z < 500\text{m}$ ) of the DICE sweep-up calculation. The medium loading concentrations are shown.

where  $\alpha$  represents the size bin, and  $c$  and  $d$  are the mass concentration and particle diameter, respectively.

The meteorological conditions can vary widely as the time of release, geostrophic wind, surface roughness, etc. are changed. We examined two typical wind speeds,  $10\text{ms}^{-1}$  and  $2\text{ms}^{-1}$ , with a fixed roughness of  $1\text{m}$  (representing forested terrain) and an early morning and a midday release, as described by Sykes, Parker and Henn (1993). The release time affects the solar radiation, and we use a linear variation of  $\theta_0$  between  $-90^\circ$  and  $+90^\circ$  during the daytime hours between 0600 and 1800. This implies a sinusoidal variation of the effective downward radiative flux at the top of the model, and we take the solar constant,  $F_0$ , to be  $1000\text{Wm}^{-2}$ . The surface albedo is arbitrarily taken to be 0.5 for these calculations, implying that 50% of the incident radiation is absorbed at the surface. The surface albedo can vary widely according to the nature of the ground cover, but a specific value is required for the model calculation and 0.5 represents a moderate albedo for illustrative purposes. As discussed in section 2, the sensible heat flux into the atmosphere is obtained from a surface energy balance which determines the fraction conducted into the soil layer and the fraction used to evaporate moisture from the surface. For simplicity in the calculations reported here, we assume that 30% of the radiative flux reaching the surface is emitted as sensible heat flux into the air. This is a

crude approximation, but is sufficient for the purpose of illustrating the dynamic effects of a dust layer on the boundary layer turbulence.

The low, medium, and high dust loadings correspond to initial optical thicknesses of about 0.6, 6, and 60 respectively. We therefore expect the low dust loading to show minimal effect on the boundary layer, while the high loading should produce a large modification. These expectations are confirmed in the results for an 0600 release in a  $2\text{ms}^{-1}$  geostrophic wind as shown in Figure 3-4. The figure shows all three loadings, plus an unperturbed boundary layer calculation (i.e., no radiative effects due to the dust) at several times up to six hours after release. The "no radiation" calculation uses the same initial concentration as the low loading case, so that the small radiative effects can be directly compared. We also show only the total concentration from each run; the particle size distributions are affected somewhat by the radiative effects, but the effects are similar to those described in the boundary layer studies in Sykes, Parker and Henn (1993).

Figure 3-4 shows immediate effects of dust loading after 1 hour. The low dust loading shows only slight differences from the zero absorption case throughout the six hour evolution, but the medium and high loading cases are significantly different. The low loading case is rapidly mixed through the developing convective boundary layer, while the medium and heavy loadings show a strong suppression of the mixing in the lower part of the distribution. The convective turbulence, driven by the surface heating, mixes the pedestal through a depth of 1.5km during the morning period for the zero and low loadings. In contrast, the heavier dust loading prevents the radiation from reaching the ground, so that the surface heat flux is much smaller and the resulting convection is much weaker. The radiation is absorbed in the upper region of the dust layer, especially for the high loading, and loft a tenuous layer of material into the overlying stable region. The bulk of the dust is apparently relatively undisturbed in the region near the surface.

An understanding of the dynamic effects of the radiative flux absorption can be obtained from examination of the turbulence and heating profiles for the different cases. Figures 3-5 through 3-8 show the potential temperature, the vertical velocity variance, the sensible heat flux, and the radiative flux profiles at the same four times as Figure 3-4. The zero case shows the typical morning evolution of the boundary layer; the shallow surface-based inversion is eroded quickly, then the mixed layer grows rapidly through the weakly stratified region marking the extent of the previous day's boundary layer. The surface heating produces a uniformly mixed potential temperature with a strong inversion

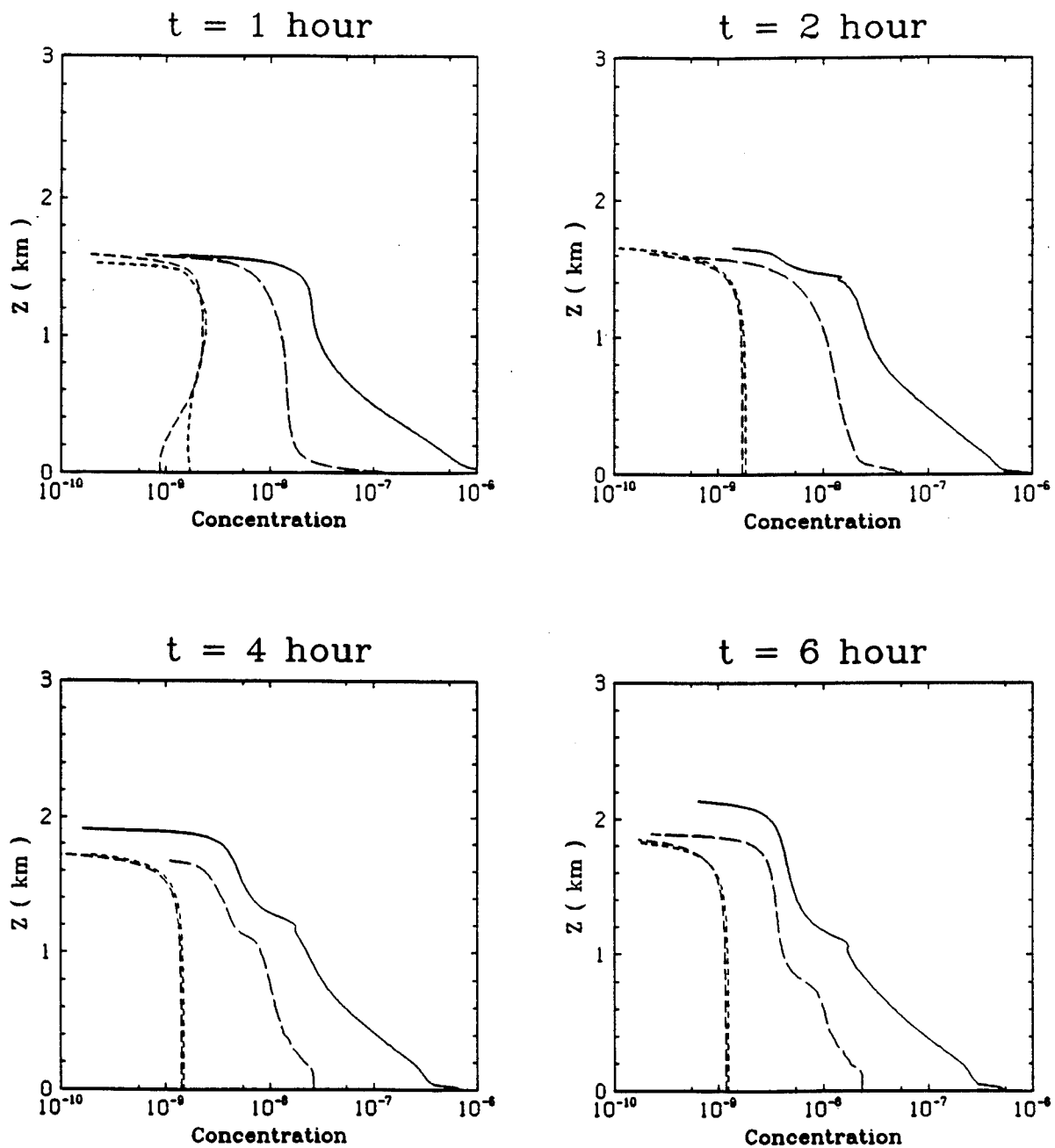


**Figure 3-4.** Concentration profiles after a morning release into a convective boundary layer with  $2\text{ms}^{-1}$  wind speed showing the radiative effect of dust loading. Solid line is high loading, long dashes medium loading, short dashes low loading, and very short dashes for low loading case with no radiative effects.

cap and overlying stable layer. The effect of the dust is to reduce the surface heating, so that the inversion is eroded more slowly, or not at all for the high loading case. However, the dust absorbs the heat directly, so at higher altitude the temperatures are warmer than the zero loading case, and a nearly mixed region is formed above the surface inversion. The higher loading cases show a deeper mixed region due to the higher heating through direct absorption. The vertical velocity variance, shown in Figure 3-6, is a direct measure of the vertical mixing rate and is very much reduced by the presence of the dust. The zero absorption case gives a variance of about  $3\text{m}^2\text{s}^{-2}$  in the middle of the mixed layer, while the high loading case only produces a variance of about  $0.4\text{m}^2\text{s}^{-2}$  in the upper part of the mixed region. Although the dust absorbs more heat, it is not absorbed in such a way as to produce kinetic energy through the release of buoyant energy.

The sensible heat flux is the buoyancy production term for the vertical velocity variance, and the profiles in Figure 3-7 show the standard linear decay from the surface value, with a small negative entrainment flux at the inversion, for the zero absorption and low loading cases. The higher loading cases, however, show that the surface heat flux is eliminated completely by the radiative absorption in the dust layer, and only a very weak heat flux is produced by the absorptive heating. The radiative flux profiles, in Figure 3-8, show that the flux is absorbed over an increasingly deep layer by the high and medium loadings, but the heating rate is uniform over the layer so that there is very little buoyancy production. The flux is just reaching the surface for the medium loading, but is completely absorbed well above the ground by the high loading. The absorbing layer warms at the same rate throughout, as indicated by the constant flux gradient, so there is no temperature contrast within the layer.

It is interesting to note the depth of the radiative flux absorption in the medium and high loading cases in Figure 3-8, about 1800m and 1600m respectively at  $t=6$  hours. The absorption can be understood by reference to the optical depth profile, shown in Figure 3-9 for the high loading case at 6 hours after release. It is clear that the linear absorption profile corresponds to the optical depth increasing from zero up to about 5. This is the optical depth beyond which virtually no radiation penetrates, so this is the layer that absorbs all the available energy. This layer behaves the same for both loading levels; it simply represents the quantity of dust needed to absorb all the radiation. Given a large reservoir of dust in the pedestal, only the amount corresponding to an optical depth of about 5 will be lofted by the heating, and the remainder will remain in the stable inversion near the surface.

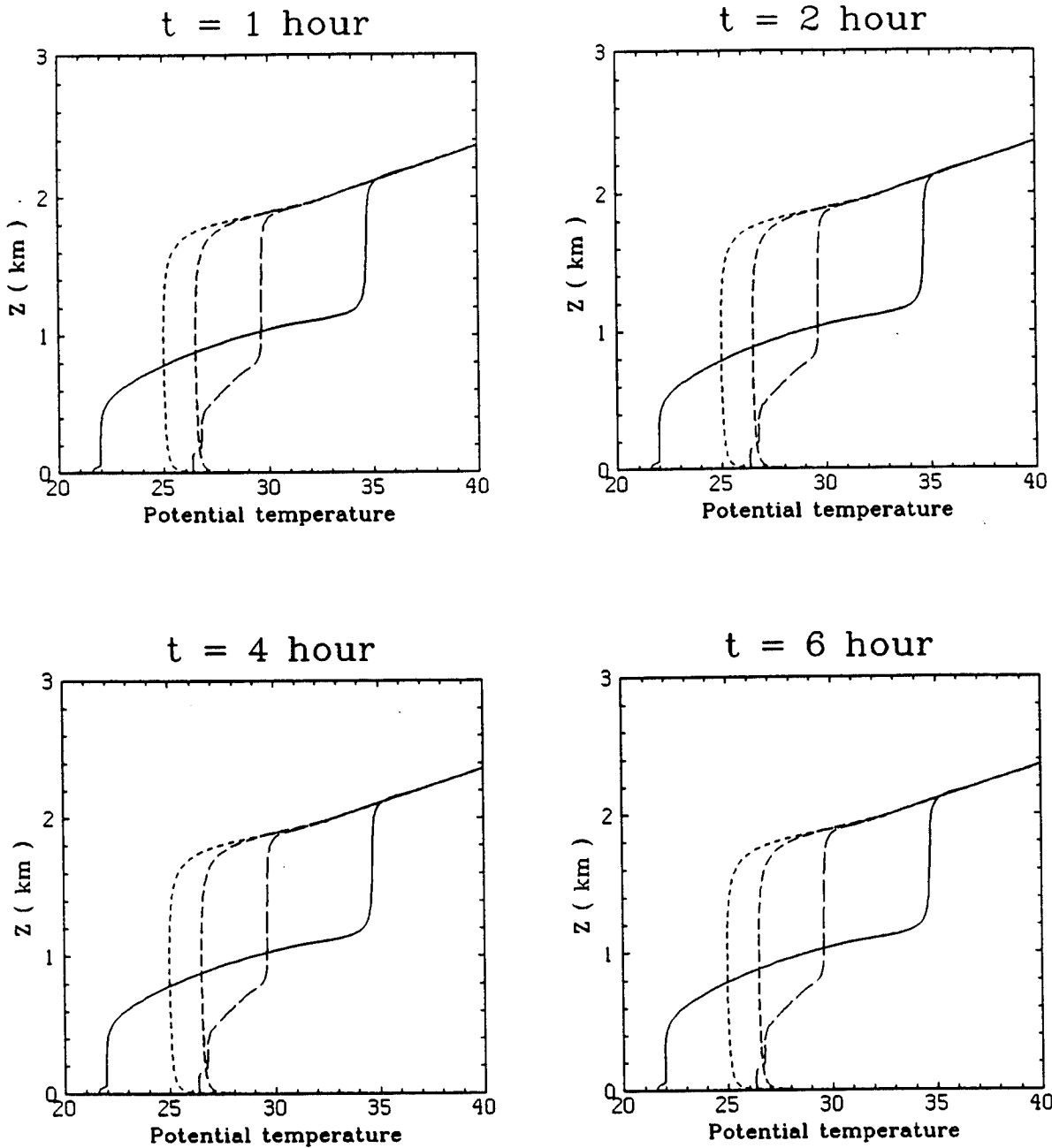


Figure 3-5. Potential temperature profiles after a morning release into a convective boundary layer with  $2\text{ms}^{-1}$  wind speed showing the effect of dust loading. Units are  $^{\circ}\text{C}$ , and the line patterns are as in Figure 3-4.

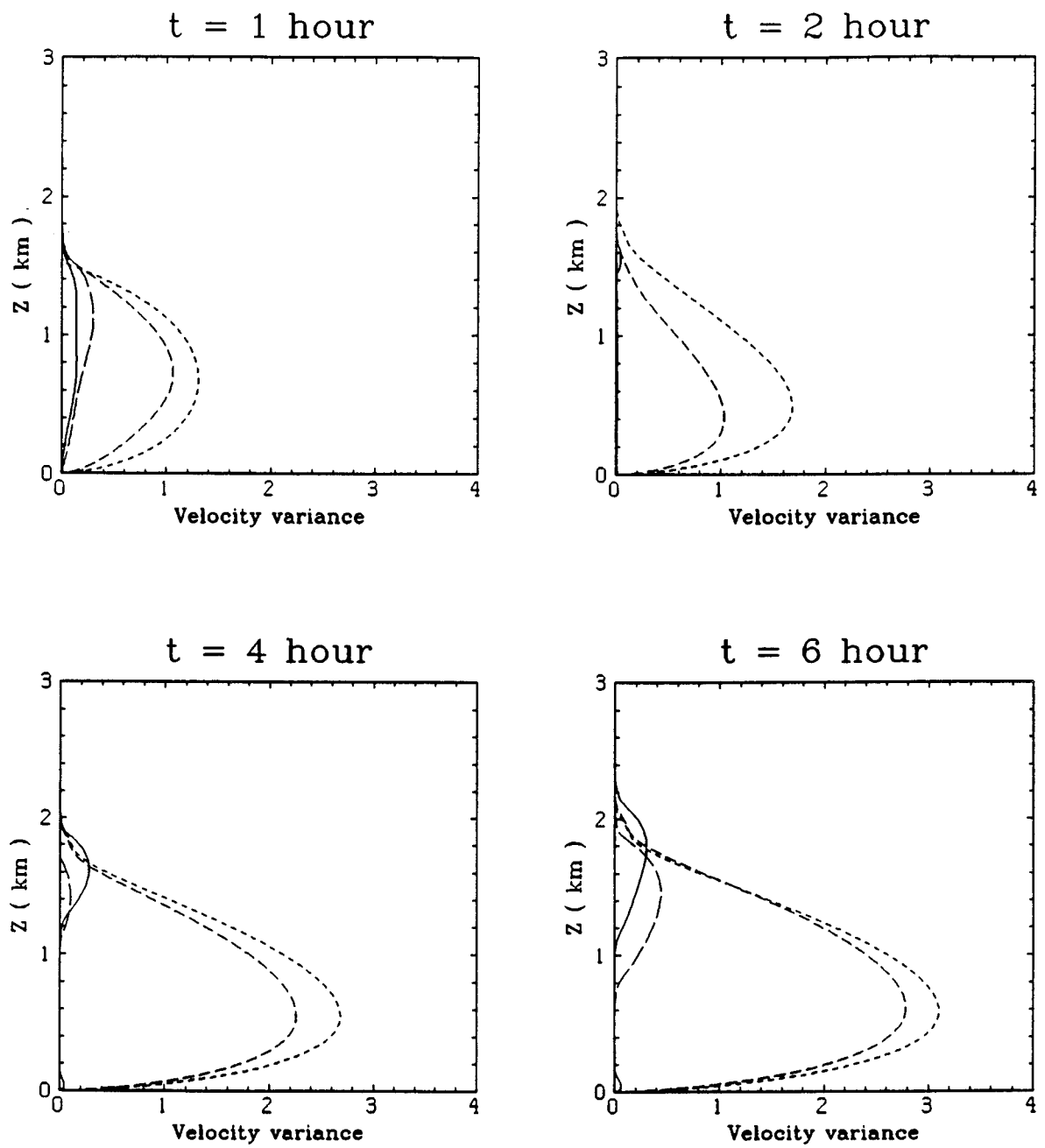


Figure 3-6. Vertical velocity variance profiles after a morning release into a convective boundary layer with  $2\text{ms}^{-1}$  wind speed showing the effect of dust loading. Units are  $\text{m}^2\text{s}^{-2}$ , and the line patterns are as in Figure 3-4.

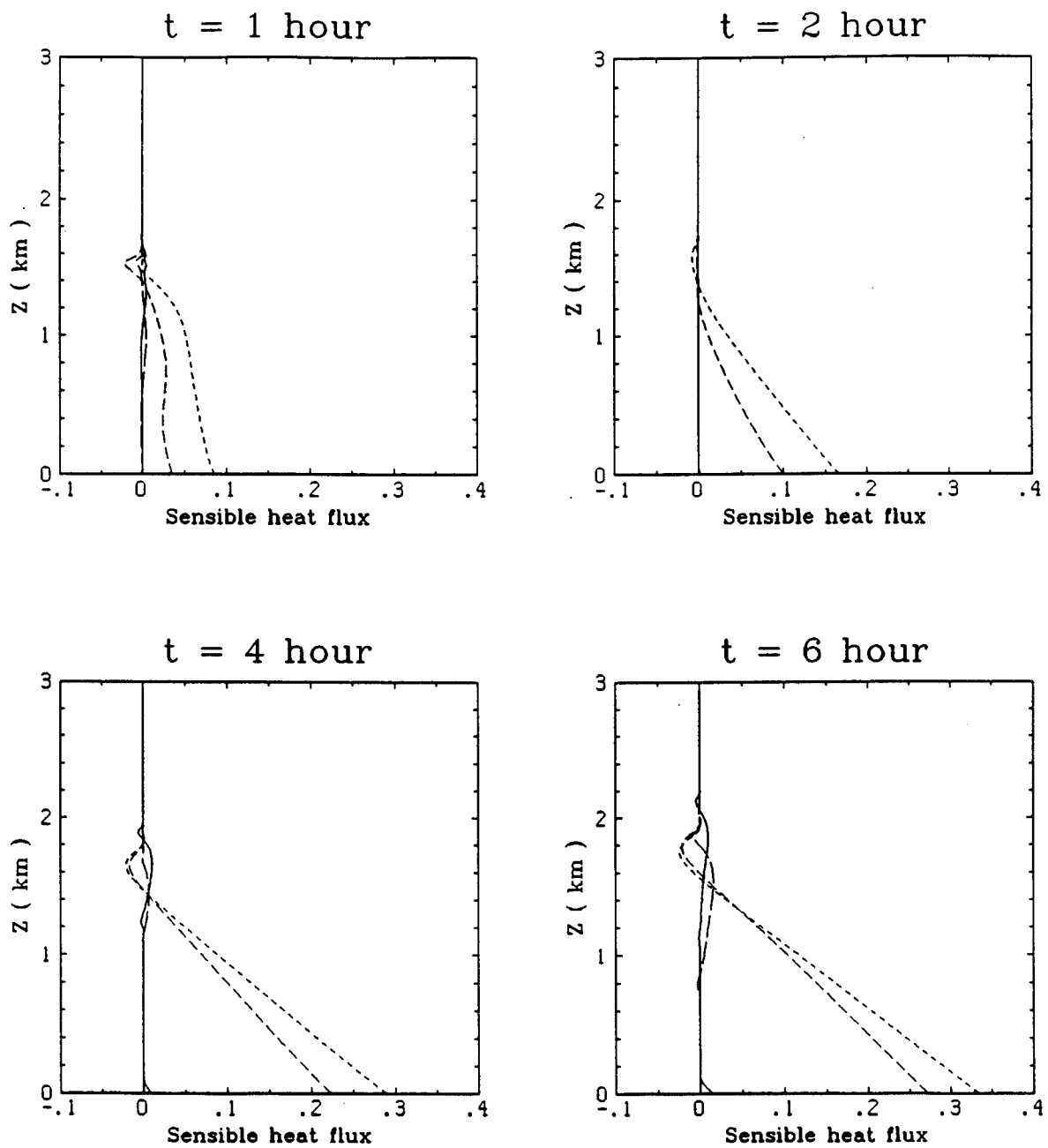


Figure 3-7. Sensible heat flux profiles after a morning release into a convective boundary layer with  $2\text{ms}^{-1}$  wind speed showing the effect of dust loading. Units are  $^{\circ}\text{Kms}^{-1}$ , and the line patterns are as in Figure 3-4.

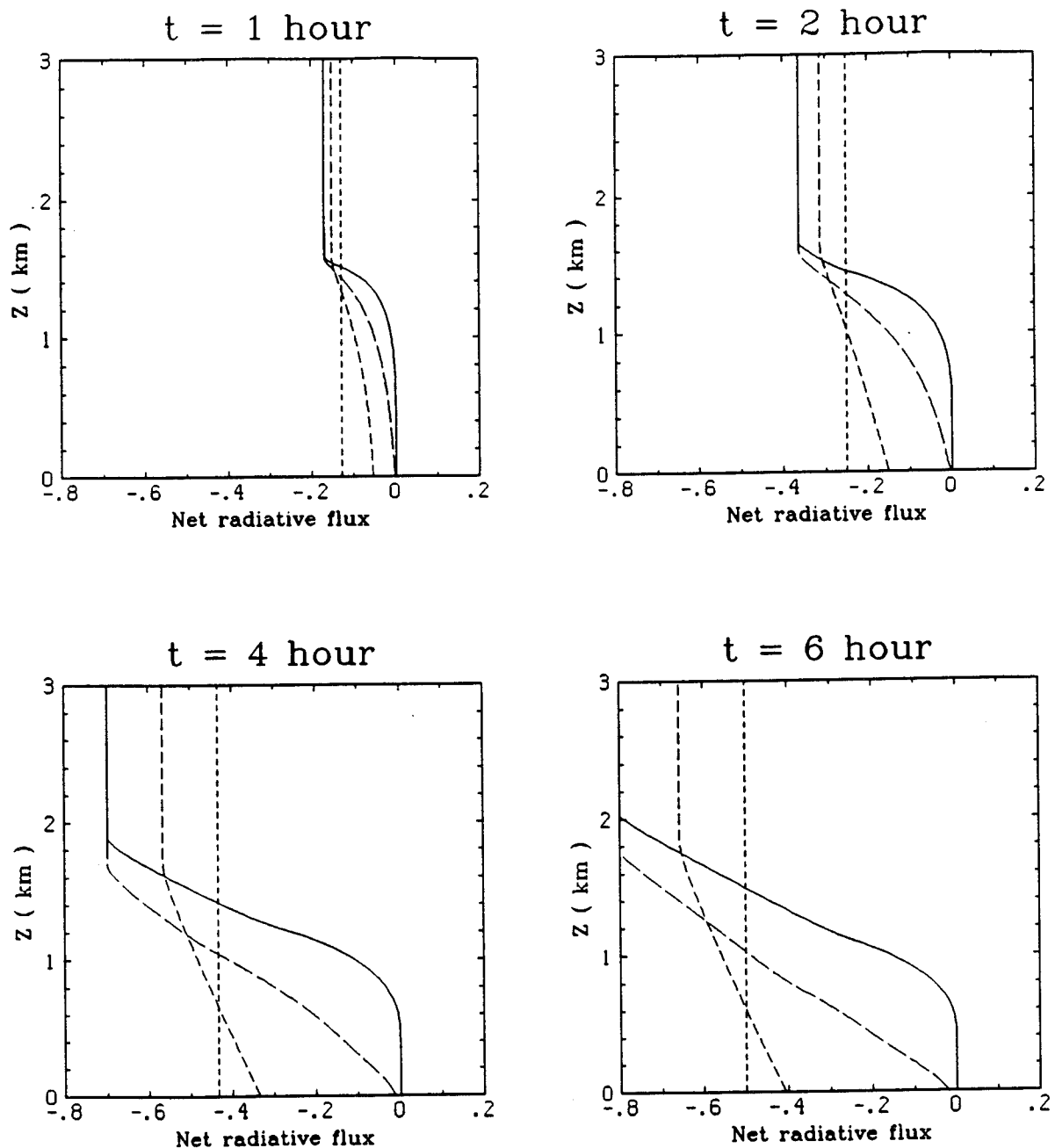


Figure 3-8. Net radiative flux profiles after a morning release into a convective boundary layer with  $2\text{ms}^{-1}$  wind speed showing the effect of dust loading. Units are  $^{\circ}\text{Kms}^{-1}$ , and the line patterns are as in Figure 3-4.

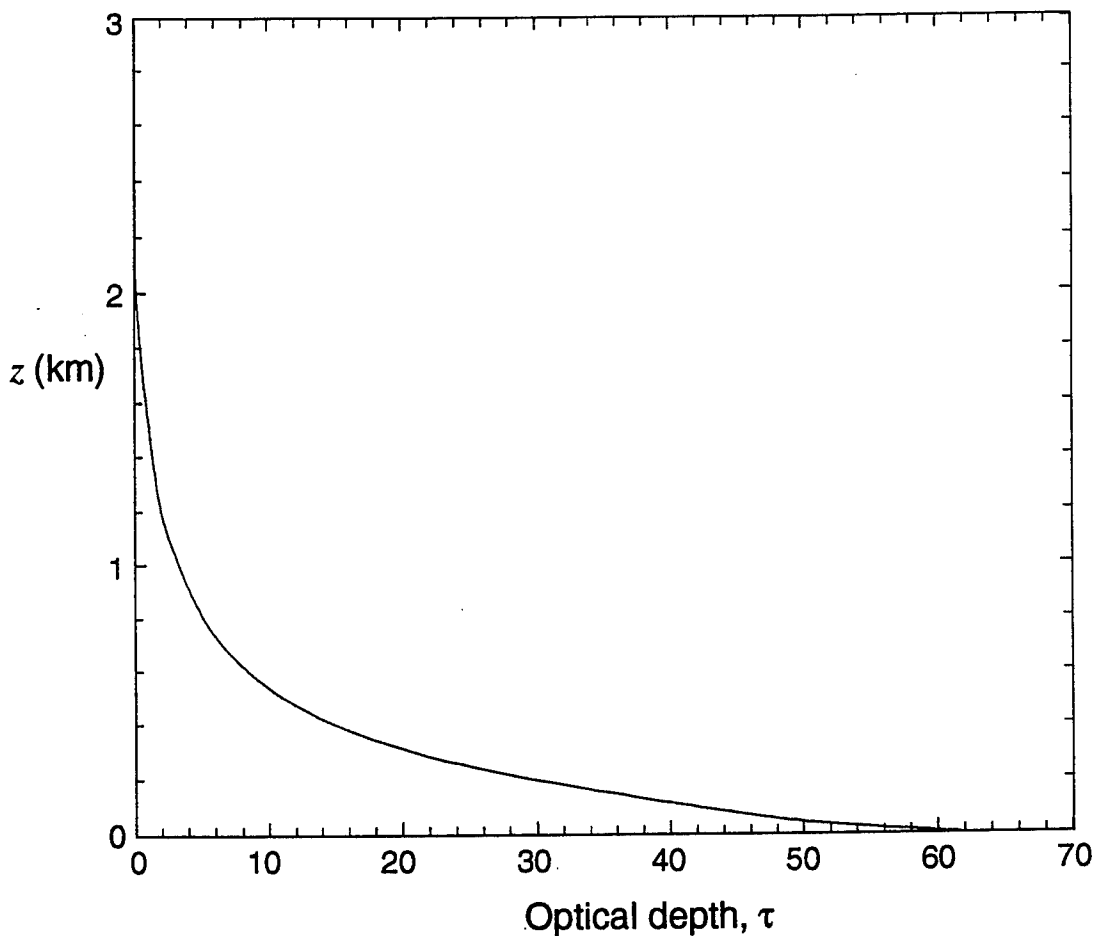


Figure 3-9. Profile of the optical depth from the high loading case at  $t=6$  hours.

The concentration profiles are less sensitive to radiative effects for a noon release, as shown in Figure 3-10. In this case, the turbulent eddies are already in existence at the initial time, and the removal of the surface heating begins a decay process. However, the dust is mixed relatively quickly through the layer, so all four cases show similar results when the initial scale factor is taken into account. The lofting process is visible in the medium and high loading cases in the upper part of the profile, and the mixing has clearly been suppressed in the lower region, but the differences between the cases are much less dramatic than the early morning release.

The representation of the detailed effects of radiative flux modifications due to the presence of dust is clearly a complex issue. The delta-Eddington model gives a relatively simple description of the scattering and absorption properties of a dust cloud, although

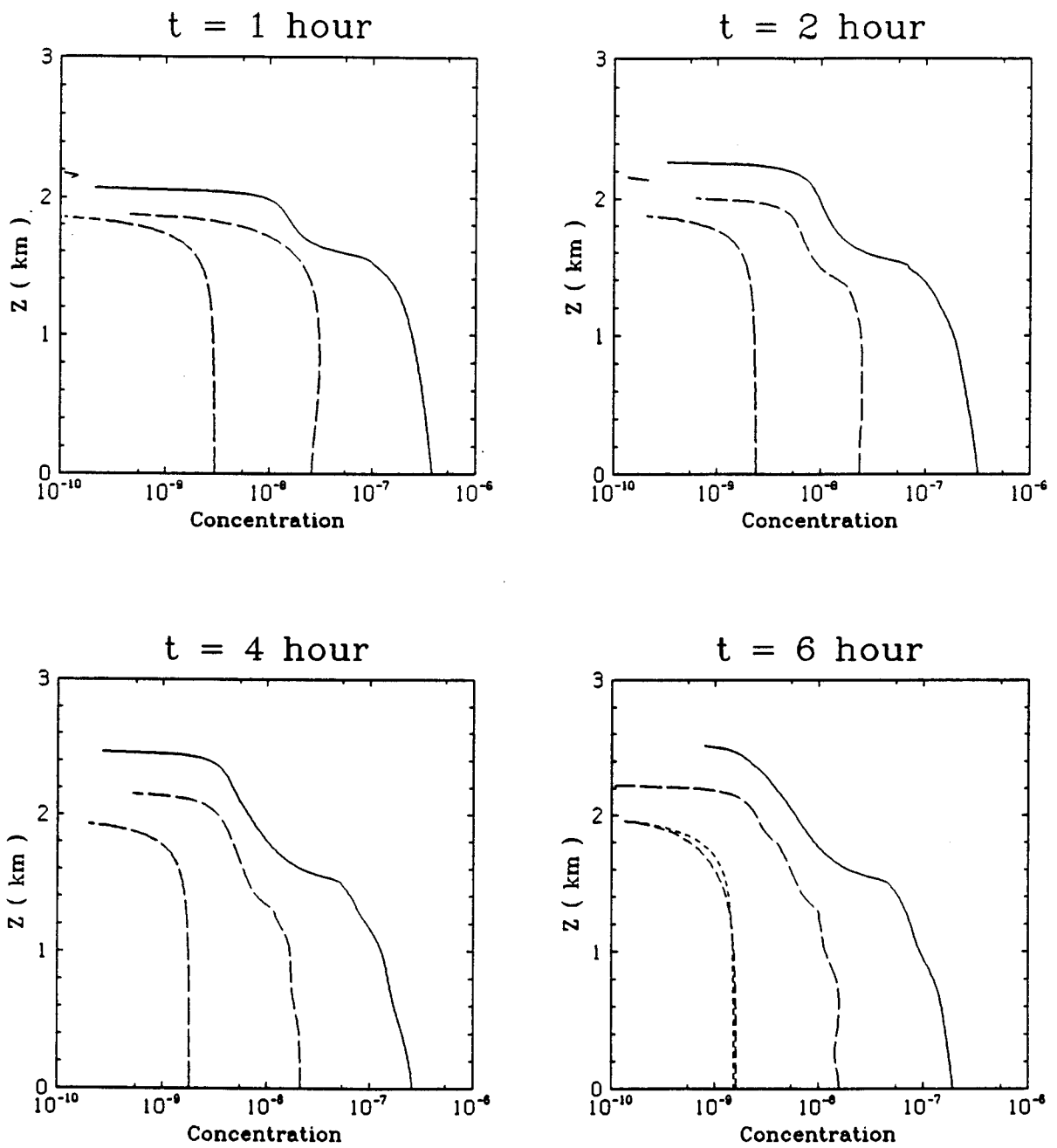


Figure 3-10. Concentration profiles after a noon release into a convective boundary layer with  $2\text{ms}^{-1}$  wind speed showing the effect of dust loading. Concentration units are  $10^{-7}\text{g/cc}$ , and the line patterns are as in Figure 3-4.

we are unable to provide quantitative comparisons between the model predictions and atmospheric observations. The model results depend on the single scattering albedo and the asymmetry factor, and these parameters are not known accurately for dust clouds. There is likely to be a range of values for different dust composition, but the typical value of 0.8 used in our study for the scattering albedo is a reasonable mid-range value. The albedo is not expected to lie outside the range between high-carbon values of 0.5 and silicate values of 0.9. Calculations with a homogeneous layer show that relatively high concentrations of small particles are required to produce a strong effect on the solar radiative flux. A concentration of  $10^{-7}$  g/cc of  $10\mu\text{m}$  particles throughout a 1km deep layer produces an optical depth of 6.67 and only 4% of the solar radiation will penetrate to the surface. Concentrations of this magnitude over a deep layer are unlikely from a single burst, but are certainly possible for a multiburst scenario. The radiative flux model, in conjunction with a second-order closure model of turbulent transport dynamics, has shown how the radiation absorbed by the dust will loft a fraction of the cloud. The lofted fraction corresponds to an optical depth of about 5, which is the depth required to absorb most of the solar flux. No radiation penetrates further into the dust cloud and therefore produces no heating of the lowest regions of the cloud. It is important to remember that the optical depth is simply a geometric quantity, as defined in this discussion, and the actual depth of penetration will depend on the single scattering albedo. A value of 0.8 implies that 80% of the energy is scattered by the particle, so that the absorption is less than  $e^{-\tau}$ ; however, the multiple scattering allows further absorption, so the value is greater than  $e^{-(1-\omega_0)\tau}$ .

The delta-Eddington model could be implemented in a full dynamic meteorological model, but the implementation in a Lagrangian late-time dispersion model is much more difficult. Clearly, the late-time dispersion model does not attempt a detailed description of dynamics, so we must consider the appropriate level of parameterization for the radiative effects. There are two main phenomena to consider in the development of a parameterization scheme. First, the effect of the cloud on the surface fluxes and the resulting boundary layer structure should be modeled. Second, we would like to represent some of the lofting effect of the solar heating on the dust cloud.

The Lagrangian framework means that we have no underlying grid on which to perform the vertical flux calculations required by the delta-Eddington model or a simpler estimation scheme. The surface flux value can be approximated very simply using the total optical depth of the overlying dust, but even this is difficult to obtain from a

Lagrangian collection of cloud elements. We can represent the transmitted fraction crudely as  $e^{-0.5\tau}$ , where the optical depth is defined by (3.11), but this requires a vertical integration. To accomplish this efficiently, a horizontal grid must be defined and the Lagrangian elements assigned to each grid cell. The grid should be large enough to represent the boundary layer scale, i.e., a few kilometers, but also fine enough to resolve the Lagrangian elements. The surface heating only needs to be estimated on the boundary layer evolution timescale, which is on the order of an hour or two.

The dynamic lofting of the dust is a more difficult problem for late-time dispersion codes. Most codes contain no dynamics, although SCIPUFF (Lewellen et al. 1989) does include a simplified treatment of buoyant rise. The description of radiative heating is more complex than that for a buoyant source, however, since the distribution of the heating depends on the dust distribution itself.

## SECTION 4

# PARTICLE DEPOSITION

### 4.1 MODEL REVIEW.

The deposition of particles to the earth's surface is important in determining the dust concentration in the context of late-time dispersion. For large particles ( $>30\mu\text{m}$ ), gravitational settling is the key transport mechanism responsible for deposition. However, for smaller particles, turbulent fluxes and, very near the surface, viscous diffusion are more important in transporting particles to the surface. Deposition to bare surfaces such as water or desert are relatively well understood and is mainly a function of surface roughness and wind speed. However, the situation is typically much more complex since most of the earth's land surface is covered by some type of vegetative canopy, ranging from grasses to crops to forests. In this case, the presence of a canopy not only modifies the turbulent fluxes but also introduces a number of potential "pathways" for depositing particles to the canopy elements. Some of the important deposition processes discussed in the literature are impaction on surface features by turbulent motion, interception by microscale surface features and diffusion by Brownian motion. These will be discussed further in greater detail. But we will note here that the relative importance of these mechanisms depends on particle size. Brownian diffusion, interception and impaction are each of primary importance for increasingly larger particles (but gravitational settling eventually dominates for large particles). The Brownian diffusion of small particles ( $<0.1\mu\text{m}$ ) is fairly well understood from laboratory experiments, but impaction and interception are much more difficult to characterize. See Slinn (1982) for further discussion. Other complications such as phoretic effects, the presence of moisture and particle growth will not be considered.

Particle deposition is typically described in terms of the deposition velocity  $v_d$ , which is defined by,

$$v_d = F_c / c \quad (4.1)$$

where  $c$  is the particle concentration and  $F_c$  is the total vertical particle flux, including the turbulent concentration flux, viscous diffusion and gravitational settling. This expression

is derived from the scalar conservation equation by assuming stationarity and horizontal homogeneity (Businger, 1986). Note that  $c$ ,  $F_c$  and therefore,  $v_d$  need to be defined at a specific reference height, typically 1m to 100m above the surface or vegetative canopy height.

Field observations of deposition velocity for a variety of canopies and particle sizes have been reviewed by McMahon and Denison (1979), Sehmel (1980) and Nicholson (1988). It is evident from these reviews that there is a great deal of inconsistency between different experiments, with variations of two orders of magnitude in the reported values of  $v_d$ . Some of the inconsistencies probably reflect real variability in the environmental conditions, although others might reflect inadequacies in the experimental techniques. Businger (1986) presents a review of the experimental techniques used to measure deposition and identifies a number of corrections and possible error sources by examining the physical processes responsible for deposition.

The variability in the observed values of  $v_d$  indicates that constructing a theoretical model of deposition will be subject to much uncertainty. On the other hand, models which contain most of the deposition physics will be useful in examining parametric variations and uncertainties, e.g., Gould and Davidson (1992), which would be difficult to achieve experimentally and would still be subject to uncontrolled environmental variability. We will not review the many theoretical models which have been presented in the literature. An indication of the various modeling assumptions and varying levels of complexity can be gleaned from the following papers: Lewellen and Sheng (1980), Bache (1979a,b), Davidson, et. al. (1982), Slinn (1982), Wiman and Agren (1985) and Peters and Eiden (1992).

Deposition velocity is often modeled in terms of the resistance of the surface layer to deposition. Resistance is then defined as the reciprocal of the deposition velocity,  $R = v_d^{-1}$ , where the deposition velocity,  $v_d$ , is redefined as the excess over that due to gravitational settling. This concept is convenient since the total resistance can be expressed as the sum of the resistances of various layers through which the particles must pass on the way to the surface (Lewellen and Sheng, 1980). For instance, Lewellen and Sheng consider four regions defining the flow near the surface and give model expressions for their "aerodynamic" resistances. The regions are the outer boundary layer, the constant flux layer (just above a smooth surface or vegetative canopy), the canopy (e.g, crops or forests), and the viscous sublayer close to a smooth surface, be it the

flat plate in a laboratory or the leaf in a forest canopy. We consider the total aerodynamic resistance and a final surface resistance to actually depositing particles after they have been brought close to canopy elements by the turbulent eddies. Thus

$$v_d^{-1} = R = R_a + R_d \quad (4.2)$$

where  $R_a$  is the aerodynamic resistance and  $R_d$  is the final surface resistance.  $R_a$  is typically set equal to momentum resistance (Lewellen, 1985), and so is the reciprocal of the "momentum deposition velocity":

$$R_a^{-1} = u_* / u_r \quad (4.3)$$

where  $u_r$  is the mean velocity at the reference height. As mentioned above, there are multiple pathways to surface deposition. The analogy to resistances in electrical circuits suggests that  $R_d$  consists of parallel resistances:

$$R_d^{-1} = R_B^{-1} + R_{IN}^{-1} + R_{IM}^{-1} \quad (4.4)$$

$R_B$  is the resistance of the viscous boundary layer flow within a millimeter of the canopy element surfaces,  $R_{IN}$  is due to particle interception and  $R_{IM}$  to particle impaction.

Slinn (1982) considers a different, but nearly equivalent, approach to particle deposition. He postulates that deposition velocity is equal to a collection efficiency multiplying the momentum deposition velocity,

$$v_d = E u_*^2 / u_r \quad (4.5)$$

With the same deposition mechanisms considered above, Slinn sets the total collection efficiency,  $E$ , to be

$$E = 1 - (1 - E_B)(1 - E_{IN})(1 - E_{IM}) \quad (4.6)$$

where  $E_B$ , etc. are the individual collection mechanism efficiencies. This approach is also taken by Davidson, et. al (1982). They give an explicit definition of local efficiency  $\eta$  for a canopy as

$$\eta = \frac{\text{particles } s^{-1} \text{ depositing}}{\text{particles } s^{-1} \text{ passing through area } d_f h} \quad (4.7)$$

such that the total particle flux is given as

$$F = N d_f \int_0^h \eta(z) u(z) c(z) dz \quad (4.8)$$

where  $N$  is the number of canopy elements (assumed cylindrical) of diameter  $d_f$  per unit area of ground,  $u$  is the mean velocity and  $h$  is the canopy height.

If the individual collection efficiencies are defined by

$$E_B = R_a / R_B, \quad E_{IN} = R_a / R_{IN}, \quad E_{IM} = R_a / R_{IM} \quad (4.9)$$

it can be shown that the resistance approach and the collection efficiency approach are equivalent for small collection efficiencies. We will continue the analysis of the individual deposition mechanisms in terms of collection efficiency. It should be remembered that canopy efficiencies are, in principle, height dependent and that the overall collection efficiency will involve integration through the depth of the canopy.

In the region very close to a relatively smooth surface such as water, a flat plate or canopy elements such as leaves or grass, Brownian motion can be important in transporting particles to the surface (assuming that surface roughness elements do no protrude through the viscous sublayer). This is particularly so for very small particles (diameter  $< 0.1 \mu\text{m}$ ) which, because of their small inertia, are able to follow small scale velocity fluctuations. Brownian motion results in the diffusion of particles, i.e., transport from high to low concentration regions. As discussed in Lewellen (1985), experimental evidence indicates that the deposition due to Brownian motion can be expressed in terms of the Schmidt number,  $Sc = v / D$ , raised to some power less than 1; thus

$$\frac{R_B}{R_a} \sim Sc^{a_B} \quad (4.10)$$

Here  $v$  is the kinematic viscosity of air and  $D$  is the particle diffusion coefficient; values of  $D$  as a function of particle radius can be found in Friedlander (1977). We follow Lewellen and Sheng in using  $a_B = 0.7$ ; this is close to Slinn's value of 2/3 but does not imply unwarranted precision. Then, in terms of collection efficiency

$$E_B = f_D S_c^{-0.7} \quad (4.11)$$

where  $f_D$  is the ratio of the viscous drag to the total canopy drag including pressure forces. This factor is needed since the particle deposition scales only with the momentum transport due to viscous forces.

Interception is essentially filtration in that particles are deposited when they are within a particle radius of the collecting elements (the characteristic size of the element is much greater than the particle radius). Particle inertia is ignored so that the particles are

moving with the fluid around the collecting element. Many interception models are based on the filtering efficiency of cylindrical fibers in potential flow,

$$E_{IN} = \frac{2a}{a_f} \quad (4.12)$$

where  $a$  is the particle radius and  $a_f$  is the filter fiber radius (Fuchs, 1964). However, for the more complex situation in a canopy, Slinn considers both "small" collectors such as vegetative hairs and "large" collectors such as grass blades and pine needles and proposes

$$E_{IN} = \left[ f \left( \frac{a}{a + A_s} \right) + (1 - f) \left( \frac{a}{a + A_L} \right) \right] \quad (4.13)$$

where  $A_s$  is the characteristic radius of "small" collectors,  $f$  is the fraction of total interception by these collectors and  $A_L$  is the characteristic radius of large collectors. Slinn (1982) shows that this formulation is in good agreement with Chamberlain's (1967) wind tunnel measurements of deposition to grass for his chosen parameters. Thus, we will use Slinn's expression while recognizing that it is crude and requires a number of empirical assumptions. Some models ignore this mechanism completely, e.g., Peters and Eiden (1992) who argue that it is negligible in their particular application to a spruce forest.

Particles are subject to impaction when they are much smaller than the collection elements but large enough so that their inertia prevents them from following the fluid flow around the elements. Collection efficiency by impaction is a function of a Stokes number, which is the ratio of the particle "stop-distance" to a characteristic canopy element length. Slinn (1982) uses a definition involving the friction velocity as do Peters and Eiden (1992). This is in contrast to Davidson et. al. (1982), who use the mean wind velocity. Following Slinn, we define the Stokes number

$$St = \frac{u_* \tau_g}{cA_L} = \frac{u_*(v_g/g)}{cA_L} \quad (4.14)$$

where  $c$  is an empirical constant set to 1 and  $\tau_g$  is the particle relaxation time. The impaction efficiency is given by Slinn as

$$E_{IM} = \frac{St^2}{1 + St^2} \quad (4.15)$$

This is a rather simple relationship compared to, for instance, Davidson and Friedlander (1978), who give

$$E_{IM} = \frac{St^3}{St^3 + 0.753St^2 + 2.796St - 0.202} \quad (4.16)$$

based on a fit to laboratory filtration data. Another model, used by Bache (1979b), Wiman and Agren (1985) and Peters and Eiden (1992), is

$$E_{IM} = \left( \frac{St}{St + a_{im}} \right)^{b_{im}} \quad (4.17)$$

where  $a_{im}$  and  $b_{im}$  are constants (set to 0.8 and 2 respectively in Peters and Eiden (1992)). Again, we follow Slinn's model in view of the demonstrated fit with Chamberlain's data.

In situations where there is no canopy, e.g., deposition to water, bare soil or rock, some modifications to the collection efficiency terms are necessary. Naturally, there is no interception, so  $E_{IN}=0$ . For  $E_B$  and  $E_{IM}$ , we use a generalization of Lewellen and Sheng's model for particle deposition to a smooth flat surface. Thus, we set

$$E_B = 0.8Sc^{-0.7} \quad (4.18)$$

and

$$E_{IM} = \frac{A_{IM}}{1 + A_{IM}} \quad (4.19)$$

where

$$A_{IM} = 0.08St(1 - e^{-0.42St}) \quad (4.20)$$

In this case, the Stokes number is given by

$$St = \frac{u_*^2 \tau_g}{\nu} \quad (4.21)$$

Predictions from this model compare favorably with Sehmel's (1973) experimental data on deposition to a smooth brass surface. It should be noted that in modifying Lewellen and Sheng's expression, we have used the quasi-equilibrium assumption  $q^2 = 5.66u_*^2$ , where  $q^2$  is twice the turbulent kinetic energy. Also, Lewellen and Sheng suggest that for particle diameters larger than about  $10\mu\text{m}$ , (4.20) should be divided by a factor  $(1 + K_4 q \tau_g / \Lambda)^2$  to account for the inability of the particles to follow the turbulent eddies. Here,  $\Lambda$  is the length scale of the turbulent eddies and  $K_4 \approx 1$ . If  $\Lambda$  can be estimated, we suggest including this factor, but it is usually very close to unity and can often be ignored.

A further complicating phenomenon is particle rebound, which reduces the deposition efficiency. It is quite dependent on surface characteristics and is not well understood (Slinn 1982). Slinn defines a rebound fraction which multiplies the total deposition efficiency. He suggests a simple function given by

$$F_{rbnd} = e^{-b\sqrt{St}} \quad (4.22)$$

where  $b$  is a constant. Since the understanding of rebound is quite poor, we typically set  $b=0$ , except in the case of Chamberlain's (1967) wind tunnel data, described below, where  $b=2$  as in Slinn (1982).

## 4.2 MODEL DEVELOPMENT.

To compute the actual deposition flux, the collection models just discussed must be coupled with models or measurements of momentum flux within the canopy. Three approaches commonly taken are

- 1) assume shapes for the velocity and eddy diffusivity profiles, e.g., Slinn (1982) and Davidson, et. al. (1982),
- 2) use measurements of velocity and make assumptions about the diffusivity, e.g., Bache (1984) and Peters and Eiden (1992) and
- 3) compute the velocity and eddy diffusivity given canopy characteristics, e.g., Lewellen and Sheng (1980).

The first approach is a kind of bulk parameterization of the flow through the canopy while the second is obviously only feasible if experimental data is available. For the typical situation where the complete deposition model must include some prediction of the flow through the canopy, we consider three types of models of increasing complexity: a simple bulk parameterization of the canopy, a one dimensional model (horizontally averaged) of the canopy which resolves the vertical profiles of mean velocity and turbulence, and a three-dimensional model, which is basically a number of one-dimensional models driven by the three-dimensional velocity field above the canopy. They all include in some way the deposition mechanisms described above.

#### 4.2.1 Bulk Canopy Model.

The bulk canopy model is the simplest and gives deposition velocity as a function of total surface momentum flux. As mentioned above, this type of model involves assumptions about the velocity profile and turbulent diffusivity in the canopy. For example, Slinn's (1982) model requires the specification of parameters such as shape factors, the ratio of canopy-top velocity to the velocity at the reference height and zero-plane displacement. However, given the capability of one-dimensional second-order turbulence closure models, such as that to be described shortly, to compute these profiles without making such gross assumptions, we suggest that models such as Slinn's be further simplified, making them appropriate for use in large-area (e.g. continental scale) three-dimensional models. For instance, if we make the assumption that  $E$  is small (say 0.1 or less), then Slinn's model can be simplified to the form

$$v_d = \frac{E}{(1-\beta)E + \beta} \frac{u_*^2}{u_r} + g\tau_g \quad (4.23)$$

where  $\beta$  is a parameter which in general will vary for different canopies and velocity profiles. This is effectively defining an overall collection efficiency for the canopy. Slinn gives some data which indicate that the range of  $\beta$  is approximately 0.1 to 0.3. Fits to the data of Chamberlain (1967) using (4.23) with  $\beta=0.16$ , along with the full Slinn model (see Slinn (1982) for the full expression), are shown in Figure 4-1. It is seen that the agreement between the simple model and the full model is quite good; both models are in good agreement with the data as well. The results are not very sensitive to changes of  $\pm 0.05$  in  $\beta$ . It remains to be determined if this simple model can be applied to other canopies and under a variety of atmospheric conditions.

#### 4.2.2 Canopy Profile Model.

The horizontally-averaged canopy model solves for the vertical profiles of mean velocity, particle concentration (or some other scalar), temperature, humidity and turbulent fluctuations using the full second-order turbulence closure scheme of Lewellen (1977). The modifications required to model the flow in a canopy are discussed in Lewellen and Sheng (1980) and will only be briefly summarized here. The total drag force is modeled as

$$D_i = \left[ c_f A_w + c_p A_f \left( 1 + u_j^2 / q^2 \right)^{1/2} \right] qu_i \quad (4.24)$$

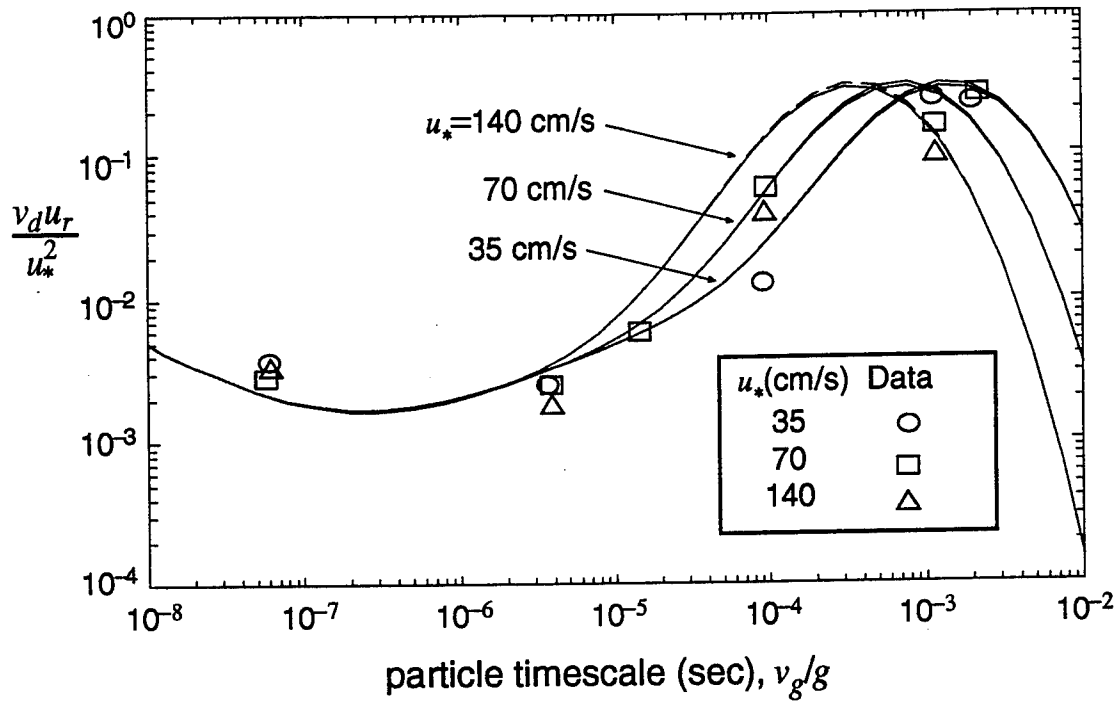


Figure 4-1. Comparison between Chamberlain (1967) wind tunnel particle deposition data (symbols), Slinn (1982) model (solid line), and bulk canopy model (4.23) (dashed line).

where  $c_f$  and  $c_p$  are the skin friction and pressure drag coefficients, respectively,  $A_w$  is the total wetted area (per volume),  $A_f$  is the frontal area (per volume),  $q^2$  is twice the turbulent kinetic energy and  $u_i$  denotes the mean velocity vector.  $c_f$  is modeled as

$$c_f = c_1 \left( \frac{v}{q\Lambda} \right)^{1/4} \quad (4.25)$$

where  $\Lambda$  is the turbulence dissipation length scale and  $c_1$  is a constant set to 1.

There are sink terms in the turbulent energy, temperature, humidity and particle concentration equations which are modeled simply by scaling the friction drag term by an appropriate function of the Prandtl number. The Reynolds stress equations are also modified by adding a source term to account for the creation of wake turbulence due to pressure drag and a sink term which models the dissipation of turbulent fluctuations by skin friction. Further details can be found in Lewellen and Sheng (1980).

The one-dimensional particle deposition model as given here uses much of Slinn's formulations in place of those given in Lewellen and Sheng, although it should be

emphasized that the full particle concentration profile through the canopy is being solved for. Thus, we are merely modifying the sink term in the conservation equation of Lewellen and Sheng, which is written as

$$\frac{Dc}{Dt} = -Ec_d A_w c - \frac{\partial}{\partial z} (F + v_g c) + \frac{\partial}{\partial z} K \frac{\partial c}{\partial z} \quad (4.26)$$

Here,  $c_d$  is the total drag coefficient such that the momentum flux due to the canopy is  $-c_d u$ ,  $E$  is the total collection efficiency as discussed above and  $K$  is the eddy diffusivity. It should be noted that collection efficiencies are local, i.e., height dependent, as in the model of Davidson, et. al. (1982) and Peters and Eiden (1992). In this context we define the local Stokes number for use in  $E_{IM}$  to be

$$St = \frac{\tau_g (q^2 + u_j^2)^{1/2}}{c A_L} \quad (4.27)$$

Davidson, et. al. (1982) use the local mean velocity while Peters and Eiden (1992) define a "local"  $u_*$ .

The results of the one-dimensional model for the grass canopy of Chamberlain (1967) are shown in Figure 4-2, along with Chamberlain's data. The vertical extent of the computational domain is twice the canopy height of 6cm and is resolved by 18 grid points. The assumed distribution of  $A_f$  is shown in Figure 4-3. The ratio  $A_w/A_f$  is assumed to be 3. The agreement with the data is good, indicating that the model is correctly including much of the physical processes occurring in the canopy. The simpler bulk canopy model matches the data somewhat better, but it should be noted that the adjustable parameters in Slinn's model and the related parameter  $\beta$  were tuned to agree with the data. The extension to other canopies and/or different wind profiles must be made with caution. The one-dimensional model, on the other hand, is more general in principle since it has fewer adjustable parameters (or at least fewer "critical" parameters). The second-order closure turbulence model parameters are determined from fits to standard laboratory flows. The canopy terms require an estimate of the pressure drag coefficient (and canopy area density which, ideally, is measured in-situ). Although the drag coefficient is undoubtedly not the same for all canopies, Lewellen and Sheng (1980) show that  $c_p=0.16$  gives reasonable results for both corn and forest canopies. (The foregoing applies principally to modeling mean velocity. The deposition mechanisms are much less well understood and are subject to greater uncertainty.) Thus it can be applied to other canopies with some degree of confidence, as we now show.

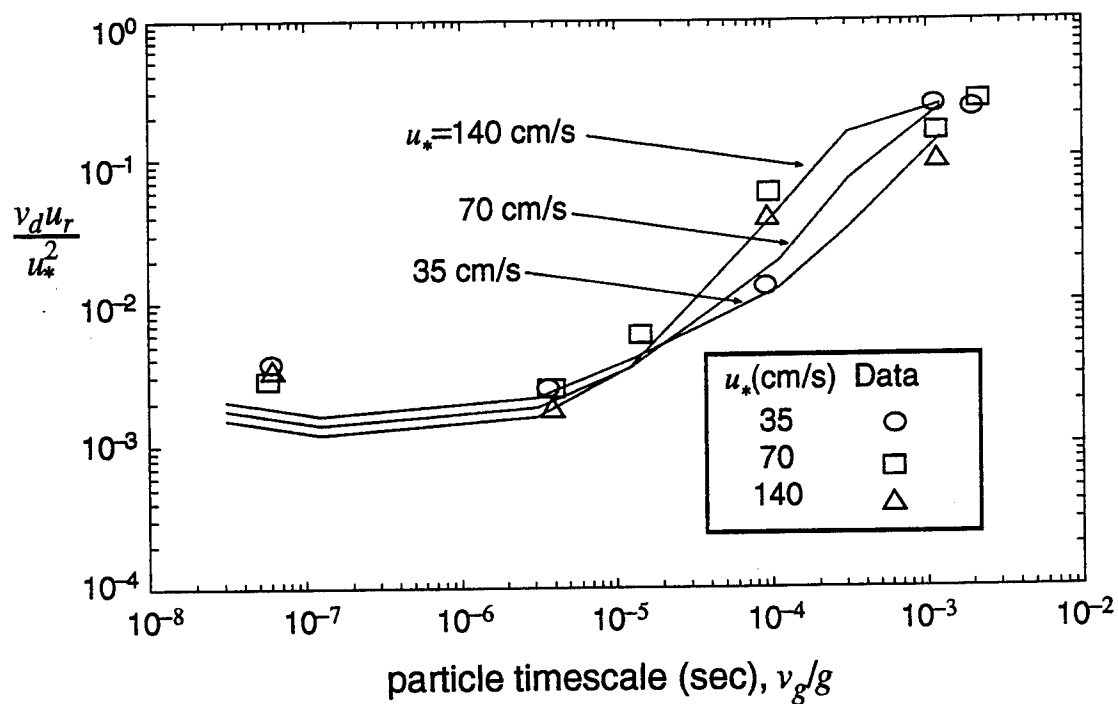


Figure 4-2. Comparison between Chamberlain (1967) wind tunnel particle deposition data (symbols) and explicit one-dimensional canopy model (4.26) (solid line).

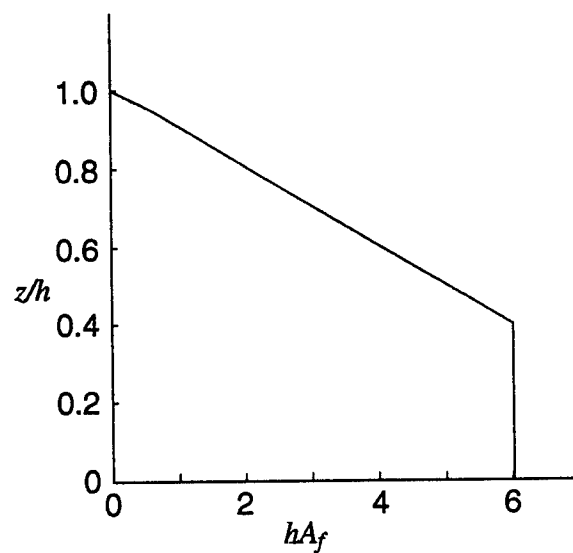


Figure 4-3. Assumed grass leaf area density profile for comparison with Chamberlain laboratory data, made non-dimensional by canopy height,  $h$ .

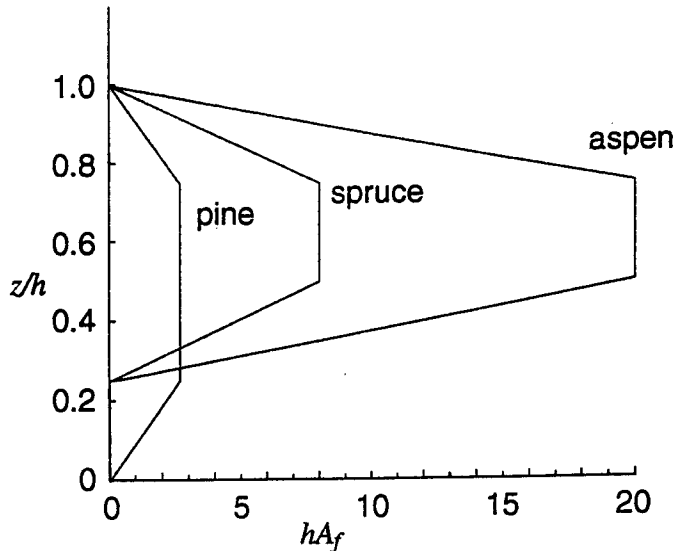


Figure 4-4 Assumed leaf area density profile for three forest canopy types, made non-dimensional by canopy height,  $h$ .

Although we are not aware of any other deposition measurements comparable to Chamberlain's there are quite a few measurements of mean velocity and turbulence statistics presented in the literature. We have chosen to compare with Amiro's (1990) data for three boreal forest canopies, pine, spruce and aspen. Based on Amiro's measurements of canopy foliage, we constructed idealized profiles of the canopy area densities which are shown in Figure 4-4. In all cases it is assumed that  $A_w/A_f = 4$ . The computational domain is the same as for the grass calculation (suitably scaled by canopy height). It should be noted that the calculations were made with a different turbulence dissipation length scale equation than that of Lewellen and Sheng (1980). An analysis of the data indicated that the length scale should be modeled as

$$\Lambda = \frac{0.05(LAI + \varepsilon)}{c_p A_f(z)} \quad (4.28)$$

where  $\varepsilon$  is a small number set to 0.1,  $c_p$  is the pressure drag coefficient, and LAI, the leaf area index, is defined as

$$LAI = \int_0^h A_f(z) dz \quad (4.29)$$

This formulation differs from that given in Lewellen and Sheng, where

$$\Lambda = \frac{\alpha}{c_p A_f(z)} \quad (4.30)$$

and  $\alpha=0.1$ . In both cases,  $\Lambda$  is constrained by the condition

$$\left| \frac{d\Lambda}{dz} \right| \leq 0.65$$

as suggested by Wilson and Shaw (1977). The original length scale (4.30) was used in Lewellen and Sheng's calculation for a corn canopy and found to be quite satisfactory. However, the formulation (4.28), based on Amiro's forest data, is not entirely satisfactory since it relates the local scale to a gross canopy measure, LAI. It is equivalent to setting the constant  $\alpha$  in the original formulation to  $0.05 * \text{LAI}$ . (The values of LAI for the pine, spruce and aspen canopies are 2, 4 and 10, respectively (Amiro, 1990).) It was found, though, that the corn canopy model calculations with (4.28) did not differ much from those with the original expression. In contrast, calculations of the forest canopy with (4.30) were quite different and showed poor agreement with the data.

Figure 4-5 shows a comparison between the one-dimensional model and Amiro's measurements of mean velocity profiles. Despite the fact that there was some "tuning" in the length scale equation to match the experiment, it is encouraging that the model predicts the mean velocity so well for different types of forest canopies. The vertical shear stress profiles in Figure 4-6 are also in good agreement with the data. In particular, the model predicts nearly uniform velocity and small shear stress seen in the bottom half of the three canopies and even suggests the presence of a local velocity maximum near the surface for the spruce and pine forests. Regions of small shear or local velocity maxima have been frequently observed in canopies with reduced foliage density near the surface (Shaw, 1977). Thus, although this effect will depend on our assumed canopy area distribution, it is nonetheless a critical result since it cannot be predicted by simple mixing-length models (Shaw, 1977) and is certainly difficult to fit into a framework requiring velocity profile assumptions as in Slinn (1982).

Figure 4-7 shows model predictions and experimental measurements of the normal velocity turbulent fluctuations in the three forest canopies calculation. The vertical velocity variance shows good agreement with the data. The horizontal components show somewhat larger discrepancies, but are still in reasonable agreement. The calculation of higher-order turbulence statistics is generally more sensitive to modeling assumptions than the mean velocity. It should be noted, however, that it is also

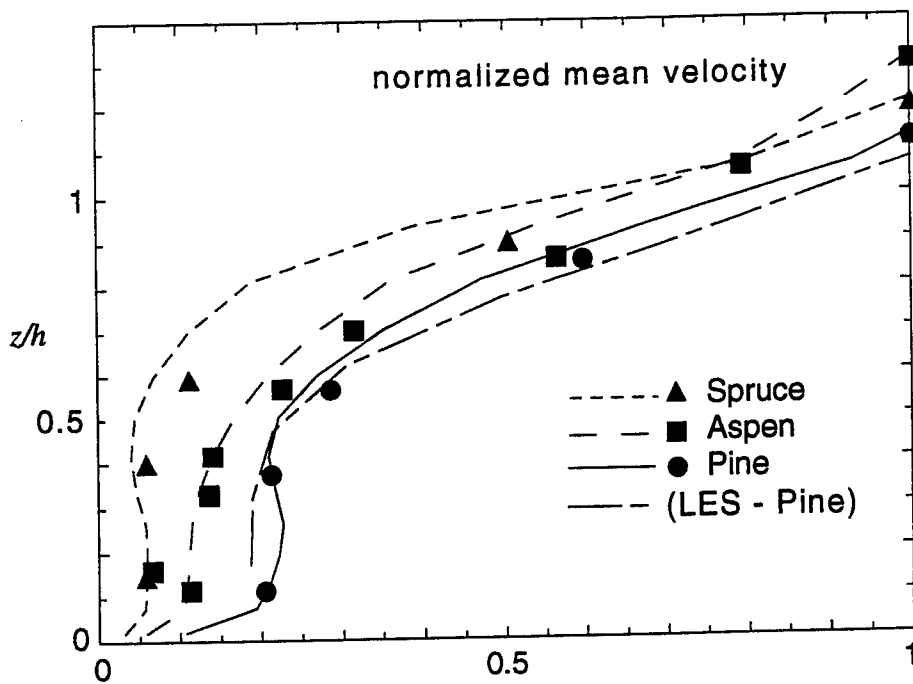


Figure 4-5. Profiles of mean velocity for three forest types normalized by the velocity above the canopy from Amiro (1990) compared with one-dimensional canopy model and LES.

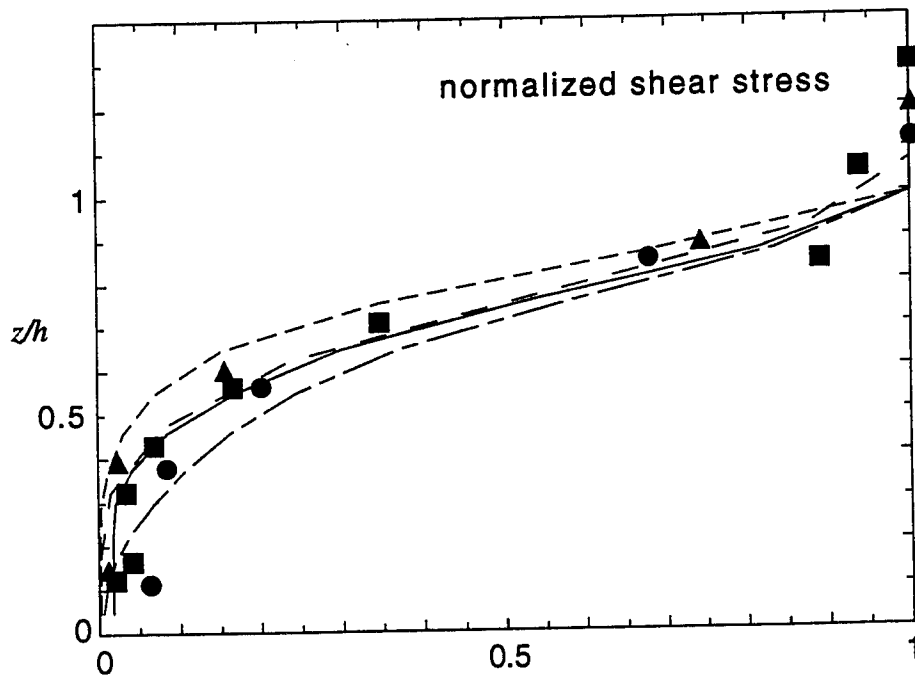


Figure 4-6. Profiles of turbulent shear stress for three forest types normalized by the value above the canopy from Amiro (1990) compared with one-dimensional canopy model and LES.

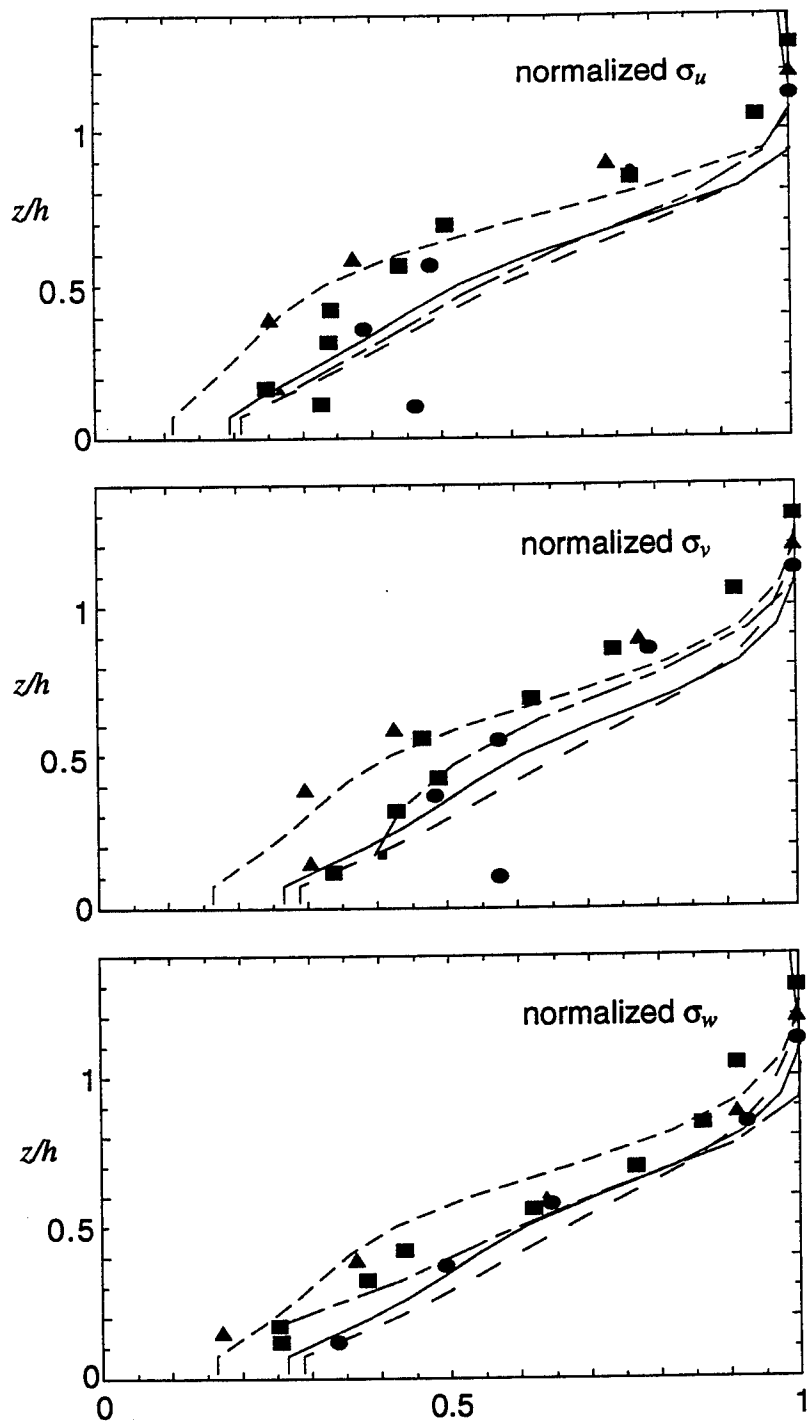


Figure 4-7. Profiles of turbulent velocity fluctuations for three forest types normalized by the value above the canopy from Amiro (1990) compared with one-dimensional canopy model and LES.

difficult to obtain reliable measurements as well and this is reflected in the large uncertainties associated with the data; typical standard deviations are about 0.1 to 0.2. It is possible that canopy inhomogeneities, non-stationarity and/or stability effects may result in measurement uncertainty.

#### 4.2.3 LES Canopy Model.

The canopy equations have also been implemented in a three-dimensional model, where the presence of the canopy effectively modifies the surface boundary conditions. The results from large-eddy simulations for the pine forest are also shown in Figures 4-5, 4-6 and 4-7. Here, the canopy is resolved by about 10 points in the vertical. The horizontal grid spacing is about eight times the canopy height. It can be seen that the one-dimensional and three-dimensional calculations are fairly close. There are some differences in  $\sigma_v$  and  $\sigma_w$  in the lower half of the canopy, where the LES predicts greater transverse fluctuation and reduced vertical fluctuations. It should be noted that we are not resolving small scale eddies, e.g., on the scale of the canopy height or less, but the large scale eddies from the atmosphere above the canopy effectively impose local mean wind boundary conditions at the canopy top.

### 4.3 DEPOSITION UNDER CONVECTIVE CONDITIONS.

LES with an explicit, vertically resolved canopy is a computationally expensive model. Late-time atmospheric dispersion calculations will be performed with a bulk canopy model as described above, and only mean velocities will be available (as opposed to the explicit turbulence of LES). The bulk deposition model requires, at a minimum, the surface momentum flux,  $u_*^2$ , which will be determined by the mean wind above the canopy and the surface roughness height as a function of canopy height and foliage density, etc. However, under free convection conditions,  $u_*$  vanishes since the mean wind is zero and so no deposition will be predicted. This is obviously not the case in reality since individual convective eddies will transport momentum (and particles) to the surface. It is possible, however, to define the average local friction speed,  $\bar{v}_*$ , as a measure of the surface momentum flux. As part of this study, we have used the LES technique to calculate the dependence of  $\bar{v}_*$  on the surface roughness and convective velocity scale  $w_* = (Hz_i g / T_0)^{1/3}$ , where  $H$  is the surface temperature flux,  $T_0$  is the reference temperature (300°K), and  $z_i$  is the convective boundary layer height. This work

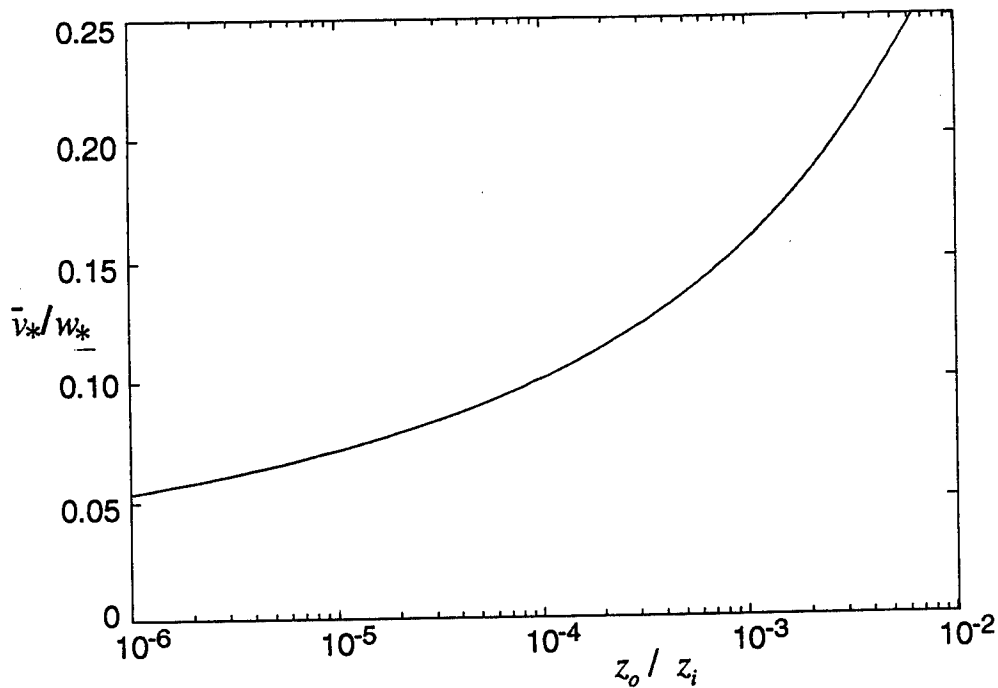


Figure 4-8. Variation of the magnitude of the average surface friction velocity with roughness length for free convection conditions.

has been published in the peer-reviewed literature (Sykes, Henn and Lewellen, 1993). By postulating a balance between inertial terms due to the large scale eddies, which scale with  $z_i$  and the vertical stress gradients across a thin surface layer (typically on the order of  $10^{-2} z_i$ ), a simple algebraic scaling relationship is obtained. The required constants are determined using LES with explicit ensemble averages of instantaneous friction velocity being calculated. The resulting relationship is

$$\frac{\bar{v}_*}{w_*} \left( 2 \ln \frac{\bar{v}_*}{w_*} - \ln \alpha_2 \frac{z_0}{z_i} \right) = \alpha_1 k \quad (4.31)$$

where  $z_0$  is the roughness height and  $k$  is von Karman's constant. The empirical constants,  $\alpha_1 = 1$  and  $\alpha_2 = 2$ , are determined from a least-squares fit to the LES ensemble averages. The resulting curve is plotted in Figure 4-8. This curve can be used to determine a mean friction velocity under free convection conditions, which can then be used in a simple deposition model. A simple curve fit to this transcendental equation is given by

$$\frac{\bar{v}_*}{w_*} = 0.46 \left( \frac{z_0}{z_i} \right)^{0.16} \quad (4.32)$$

Probability distributions of the instantaneous friction velocity normalized by the ensemble mean value are shown in Figure 4-9(a). The shapes are very similar for different roughness lengths and are nearly symmetric about their means. It appears that distributions are very nearly Gaussian, with the standard deviations being approximately one third of the mean (but decreasing slowly with increasing roughness). Figure 4-9(b) shows probability distributions for cases with mean geostrophic wind, but which are still dominated by convective eddies. It is evident that the distributions become narrower about the mean as the geostrophic wind increases. It is also interesting to note that these simulations indicate that for even small mean winds,  $u_*$  is very close to  $\bar{v}_*$ . Thus it is most likely that the free convection  $\bar{v}_*$  can be used as a minimum on the friction velocity:

$$u_* = \max(\bar{v}_*, u\Psi^{-1}) \quad (4.33)$$

where  $\Psi$  is the normalized velocity profile given by

$$\Psi = k^{-1} \left[ \ln \frac{z}{z_0} - \Phi_m \right] \quad (4.34)$$

and  $\Phi_m$  is a stability correction to the neutral logarithmic profile based on Monin-Obukov similarity theory (Businger, 1973).

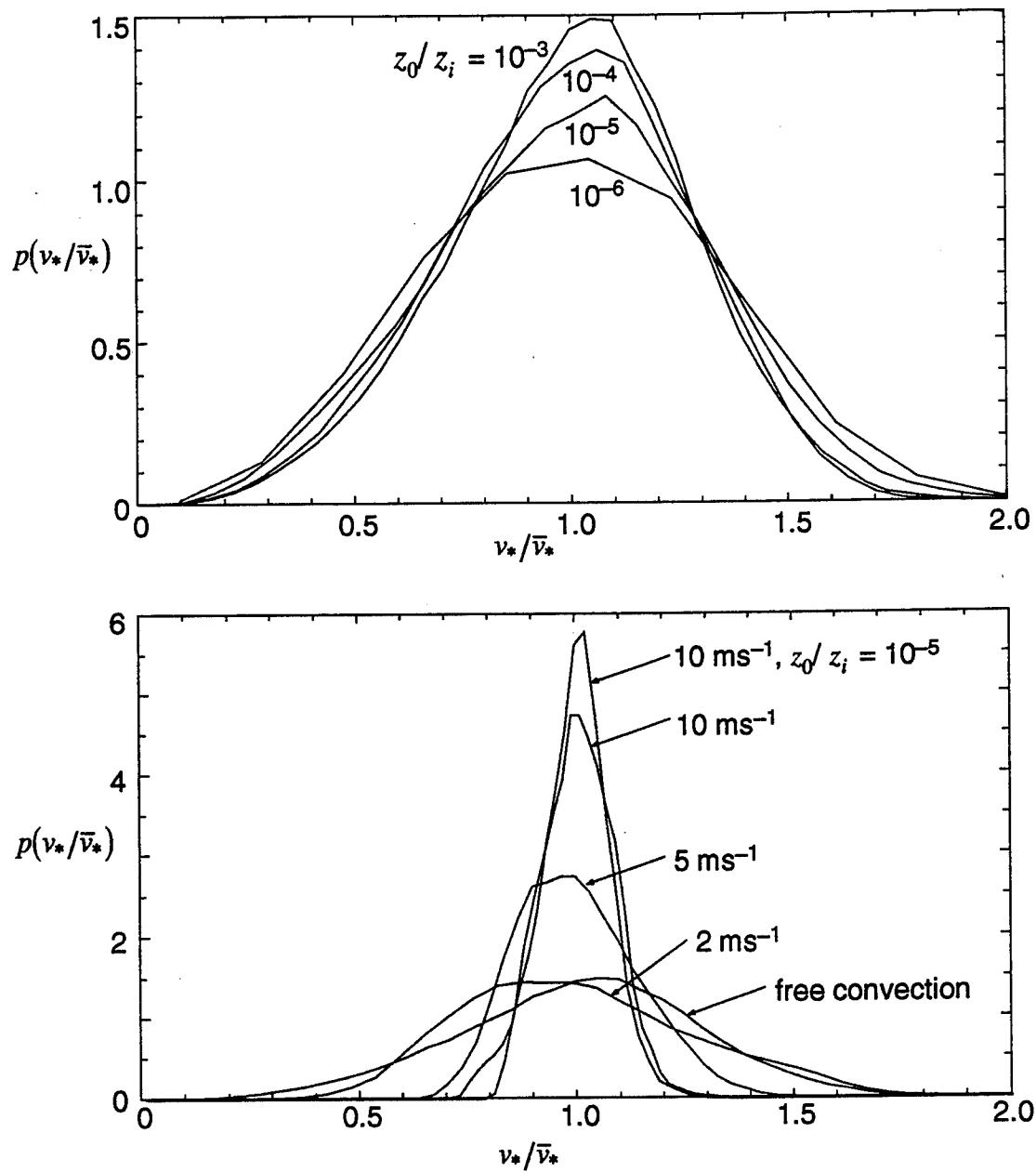


Figure 4-9. Probability density function for the instantaneous friction velocity.  
 (a) variation with roughness length for free convection conditions;  
 (b) variation with geostrophic wind speed, dimensionless roughness of  $10^{-4}$  except where indicated.

## SECTION 5

### TERRAIN EFFECTS

#### **5.1 GENERAL REMARKS.**

The PBL representation discussed in Section 2 is appropriate for a homogeneous, flat surface. The dynamics of the planetary boundary layer under these conditions are generally well understood, at least for neutral and unstable conditions, and the mean flow, turbulence, and dispersion characteristics can be determined in terms of a few important PBL parameters. The turbulence generation mechanisms, namely shear and buoyancy, are adequately represented by current parameterization methods using boundary layer quantities such as the surface friction velocity and the convective velocity scale, (Deardorff, 1972). Research continues to reveal details of the turbulence structure, but the main features of the flow are now well accepted.

The actual situation in the atmosphere is rarely ideal, however. The surface is not usually homogeneous, but contains variations in character and elevation on all length scales. The distinction between the surface roughness and the surface elevation variations is somewhat arbitrary, but the roughness is usually taken to refer to complex surface features much smaller than the boundary layer depth. The local surface roughness is therefore determined by the surface coverage, e.g., type of vegetation, density of buildings, water surface, etc. The surface coverage is generally inhomogeneous on scales of interest for meteorological prediction models, both synoptic and mesoscale, so representations are required for larger scale area-averages. Recent efforts to describe the effects of non-uniformity in local surface roughness have been made by Mason (1988), Vihma and Savijarvi (1991), and Wood and Mason (1991).

The effects of terrain elevation variations have often been represented using the same framework of surface roughness specification as the smaller scale features. Many studies of neutral boundary layer flow over terrain features have been conducted, and Taylor et al. (1989) present a synthesis of several numerical modeling approaches to determine a parameterization of the drag forces. All of the models employ empirical closure techniques for the turbulent flow, although there is some insensitivity to the level

of closure in the drag results. There are also a number of theoretical analyses of neutral flow over idealized terrain, e.g., Jackson and Hunt (1975), Sykes (1980), Hunt et al (1988), which have helped to delineate the important phenomena in the flow. In general, however, there are no reliable parameterizations of the boundary layer over complex terrain. We attempt to improve the situation by means of numerical simulation of the turbulent processes over hilly terrain.

Our approach to the problem is to use the best available turbulence modeling technique to calculate boundary layer flow over idealized terrain shapes for a range of meteorological conditions. The numerical technique is Large Eddy Simulation (LES), which involves a three-dimensional, time-dependent integration of the equations of motion, using a finite-difference grid of sufficient resolution that the energy-containing turbulent eddies can be represented explicitly (Rogallo and Moin, 1984). This allows a direct computation of the dynamics of the large eddies and avoids any empirical closure assumption. It is impossible to resolve the entire spectrum of motions in the atmosphere, so the LES requires a subgrid closure to represent the effects of eddies too small to appear on the finite-difference grid. However, the subgrid closure is only important for the small-scale features and becomes less important as the grid is refined.

We use LES to obtain detailed results for simple terrain and develop parameterizations based on these idealized cases. We shall examine the effects of terrain slope, wavelength, height, surface roughness, and atmospheric stability. The parameterizations will be written in terms of general terrain characteristics, so that the results can be extended to more complex topography. We shall then test the parameterizations by actual computation with different terrain shapes.

The technique of Large-Eddy Simulation allows a more reliable representation of the turbulent processes than one-point closure models, provided that the dominant eddies can be resolved by the calculation. This requirement is much easier to achieve in the case of convective boundary layer flows, where the turbulence generation mechanism produces large-scale eddies directly. Studies of free convection flows (Mason, 1989; Schmidt and Schumann, 1989; Sykes and Henn, 1989) have demonstrated the capability of LES for these flows. The neutral flow situation is more difficult to calculate with LES, since the shear generation mechanisms are concentrated in the small scales near the surface where the shear is highest. LES has difficulty representing this region reliably (Mason and Thompson, 1992). In contrast to the LES limitations, the theoretical

approaches used for neutral boundary layer flow are not easily extended to the convective case. The theories rely on a linearization about the undisturbed boundary layer flow, but the effects of surface heating over a sloping surface can produce vertical motions in convective cells with preferential alignment. The convective flow situation thus presents a suitable candidate for LES investigation.

Free convection over a wavy surface has been studied recently by Krettenauer and Schumann (1992) and Walko et al. (1992) using LES. The conclusions from these studies are generally concerned with the modification of the convective cell structure by the terrain slopes, which are two-dimensional with no variation in the  $y$ -direction. In the absence of any mean wind, the terrain can preferentially lock the updrafts in the form of rolls aligned with the surface terrain in the lower part of the mixed layer, although the general turbulence profiles do not appear markedly different from convection over a uniform surface.

In the present study, we are interested in the effects of two-dimensional terrain variations on convective boundary layer flow with a mean geostrophic wind. We shall restrict attention to a simple sinusoidal terrain shape and attempt to determine the variations with terrain wavelength and slope. The principal features of interest are the mean flow and turbulence modifications. The integrated momentum deficit (relative to the geostrophic wind) must balance the surface forces in the steady state, and this balance will be used to check the steadiness of the solutions. The dependence of the drag forces on terrain and surface parameters will be determined from the LES results.

## 5.2 NUMERICAL MODEL DESCRIPTION.

The basic model used for this study is an extension of the Cartesian model of Sykes and Henn (1989). The model is a second-order accurate, finite difference representation of the filtered equations of motion for an incompressible, Boussinesq fluid. A terrain-following coordinate transformation was introduced using the techniques of Clark (1977). The vertical coordinate used in the model,  $\zeta$ , is defined as

$$\zeta = \frac{z - h}{J} \quad (5.1)$$

where

$$J = 1 - \frac{h}{D} \quad (5.2)$$

Here  $h(x,y)$  is the local terrain elevation,  $z$  is the Cartesian vertical coordinate, and  $D$  is the depth of the model domain. Following Clark, we retain the Cartesian velocity components for the momentum and Reynolds stress representations and define a transformed vertical component,  $\omega$ , which simplifies the advective transport computation. Thus,  $(u,v,w)$  are the velocity components in the  $(x,y,z)$  directions respectively, and  $\omega$  is defined as

$$\omega = w - G_x u - G_y v \quad (5.3)$$

where

$$G_x = \left(1 - \frac{\zeta}{D}\right) \frac{\partial h}{\partial x}, \quad G_y = \left(1 - \frac{\zeta}{D}\right) \frac{\partial h}{\partial y} \quad (5.4)$$

The momentum equations can be written

$$\frac{Du}{Dt} = -\frac{\partial}{\partial x}(Jp) - fJ(v - v_g) + \frac{\partial}{\partial x}(J\tau_{11}) + \frac{\partial}{\partial y}(J\tau_{12}) + \frac{\partial}{\partial \zeta}(\tau_{13} + G_x \tau_{11} + G_y \tau_{12} - G_x p) \quad (5.5a)$$

$$\frac{Dv}{Dt} = -\frac{\partial}{\partial y}(Jp) + fJ(u - u_g) + \frac{\partial}{\partial x}(J\tau_{12}) + \frac{\partial}{\partial y}(J\tau_{22}) + \frac{\partial}{\partial \zeta}(\tau_{23} + G_x \tau_{12} + G_y \tau_{22} - G_y p) \quad (5.5b)$$

$$\frac{Dw}{Dt} = -\frac{\partial p}{\partial \zeta} + \frac{g\theta}{T_0} J + \frac{\partial}{\partial x}(J\tau_{13}) + \frac{\partial}{\partial y}(J\tau_{23}) + \frac{\partial}{\partial \zeta}(\tau_{33} + G_x \tau_{13} + G_y \tau_{23}) \quad (5.5c)$$

where the material derivative is defined as

$$\frac{D\phi}{Dt} = \frac{\partial}{\partial t}(J\phi) + \frac{\partial}{\partial x}(Ju\phi) + \frac{\partial}{\partial y}(Jv\phi) + \frac{\partial}{\partial \zeta}(\omega\phi) \quad (5.6)$$

In the above equations,  $g$  is the gravitational acceleration,  $\theta$  is the potential temperature,  $T_0$  is the Boussinesq reference temperature,  $p$  is the dynamic pressure, and  $\tau_{ij}$  is the subgrid stress tensor. The geostrophic wind is  $(u_g, v_g)$  and  $f$  is the Coriolis parameter, which we take to be  $10^{-4}s^{-1}$  in all the calculations reported below. The mass conservation equation is simply

$$\frac{\partial}{\partial x}(Ju) + \frac{\partial}{\partial y}(Jv) + \frac{\partial \omega}{\partial \zeta} = 0 \quad (5.7)$$

The potential temperature equation is

$$\frac{D\theta}{Dt} = \frac{\partial}{\partial x}(JH_1) + \frac{\partial}{\partial y}(JH_2) + \frac{\partial}{\partial \zeta}(H_3 + G_x H_1 + G_y H_2) \quad (5.8)$$

where  $H_i$  is the subgrid heat flux.

The subgrid turbulence model uses a turbulent kinetic energy transport equation based on the second-order closure model of Lewellen (1977). The subgrid velocity variance,  $q^2$ , is obtained from the following conservation equation

$$\frac{Dq^2}{Dt} = 2J\tau_{ij}\frac{\partial u_i}{\partial x_j} - 2\frac{g}{T_0}JH_3 + \frac{\partial}{\partial x}(JF_1) + \frac{\partial}{\partial y}(JF_2) + \frac{\partial}{\partial \zeta}(F_3 + G_x F_1 + G_y F_2) - 2bJ\frac{q^3}{\Lambda} \quad (5.9)$$

where  $F_i$  is the subgrid flux, and  $\Lambda$  is the subgrid turbulence length scale. The first two terms on the right hand side represent shear and buoyancy production respectively, and the last term is the dissipation rate. The empirical turbulence model constant,  $b$ , is 0.125 (Lewellen, 1977).

Subgrid fluxes are modeled as

$$H_i = \kappa \frac{\partial \theta}{\partial x_i} \quad (5.10)$$

similarly for  $F_i$ , and

$$\tau_{ij} = \nu \left( \frac{\partial u_i}{\partial x_j} + \frac{\partial u_j}{\partial x_i} \right) \quad (5.11)$$

for the subgrid stresses. The subgrid diffusivities are obtained from the equilibrium second-order closure results,

$$\kappa = S_H q \Lambda, \quad \nu = S_m q \Lambda \quad (5.12)$$

with the stability-dependent coefficients,  $S_H$  and  $S_m$ , are given by

$$S_H = \frac{(1-2b)/3}{A + Ri(2 + 1/b\sigma)} \quad (5.13a)$$

$$S_m = \frac{(A^2 + (A/b\sigma - 1)Ri)}{A + Ri} S_H \quad (5.13b)$$

The subgrid turbulent Richardson number is defined as

$$Ri = \frac{g}{T_0} \frac{\partial \theta}{\partial z} \frac{\Lambda^2}{q^2} \quad (5.14)$$

Finally, the subgrid length scale is defined as

$$\frac{1}{\Lambda^2} = \frac{1}{\Lambda_0^2} + \frac{1}{\Lambda_{\max}^2} \quad (5.15)$$

where  $\Lambda_0 = \min(\alpha n, q/2N)$ ,  $n$  is the normal distance from the lower boundary,  $z = h(x,y)$ .  $N$  is the Brunt-Vaisala frequency and the turbulence constants  $\alpha=0.65$ ,  $s=1.8$  and  $A=0.75$  are chosen to match the log-layer profile with a von Karman's constant of 0.4. This formulation follows the philosophy of Mason and Callen (1986) in distinguishing between the filter scale,  $\Lambda$ , and the numerical grid scale. The specification of  $\Lambda_{\max}$  is problem-dependent and will be given below.

The finite-difference representations are similar to those used in the Cartesian model of Sykes and Henn (1989). Temporal differencing uses the second-order leapfrog scheme with a small amount of smoothing, usually 1%, to couple the two time levels and prevent time-splitting. The advective terms use the 'absolutely-conserving' scheme of Piacsek and Williams (1970) to maintain conservation of momentum and energy. Diffusion terms use central differencing with the du Fort-Frankel approximation to provide a stable integration.

The elliptic equation for the pressure field is obtained by application of the finite-difference divergence operator to the partially advanced velocity field, i.e., including all terms except the pressure gradient. The pressure field is then computed from the non-separable equation to maintain zero divergence of the velocity field. The presence of the terrain terms prevents the use of the orthogonal decomposition methods of the Cartesian model, so an iterative scheme is employed. The pressure equation is written in the form

$$L_0(p) = N(p) + S \quad (5.16)$$

where  $L_0$  represents the Cartesian finite-difference operator (i.e., the case  $h = 0$ ),  $N$  represents the terrain transform terms, and  $S$  is the divergence source term. The solution is obtained using the Cartesian solver for each iteration of the system

$$L_0(p^{(n+1)}) = N(p^{(n)}) + S \quad (5.17)$$

using the previous timestep value as the first guess for  $p^{(0)}$ . The iteration is continued until the maximum change in  $p$  is less than  $10^{-5}$  times the maximum value of  $p$ . The convergence rate depends on the terrain slopes, since  $N(p)$  is generally proportional to the square of the slope. This limits the maximum slope to about unity, although a practical limit is 0.75, since the convergence becomes unacceptably slow. For slopes of 0.5, the procedure requires about 5-7 iterations for convergence.

The accuracy of the pressure solution is improved by the removal of the hydrostatic pressure field. This is accomplished in the transformed coordinate model by averaging the potential temperature field horizontally, i.e., temperatures are interpolated onto a horizontal level before averaging; the average value is then computed on the transformed grid and subtracted from the local value when used in the  $w$ -equation. This procedure is applied at each timestep to minimize the hydrostatic contribution.

### ***Boundary conditions***

Lateral boundary conditions are periodic for all variables and therefore need no further description. The domain should be sufficiently large that the artificial periodicity does not influence the results, and several calculations were made to check the sufficiency of the domain size. The upper boundary,  $z = D$ , is a rigid, stress-free lid but a Rayleigh damping is applied to the vertical velocity over the top 6 grid levels. The damping increases toward the boundary and provides an effective non-reflecting boundary for the propagating gravity waves. Thus

$$\omega = \tau_{13} = \tau_{23} = H_3 = F_3 = 0 \quad \text{at } \zeta = D \quad (5.18)$$

Surface boundary conditions in the transformed coordinate system require careful consideration, however, since we are specifically interested in the surface forces. The normal velocity component is easily specified, namely

$$\omega = 0 \quad \text{at } \zeta = 0 \quad (5.19)$$

The momentum fluxes are obtained from a surface layer analysis using Monin-Obukhov similarity to relate the surface stress to the velocity at the first grid point. For a flat surface, this gives  $\tau_{13}$  and  $\tau_{23}$  at  $z = 0$  from the relations

$$\tau_{13} = u_*^2 \frac{u_1}{(u_1^2 + v_1^2)^{1/2}} , \quad \tau_{23} = u_*^2 \frac{v_1}{(u_1^2 + v_1^2)^{1/2}} \quad (5.20)$$

and

$$u_* = (u_1^2 + v_1^2)^{1/2} \phi\left(\frac{z_1}{z_0}, \frac{z_1}{L}\right) \quad (5.21)$$

where  $u_1$  and  $v_1$  are the velocity components at the first grid point above the surface, at height,  $z_1$ . The roughness length is  $z_0$ ,  $u_*$  is the friction velocity, and  $L$  is the Monin-Obukhov length, defined as

$$L = -\frac{u_*^3 T_0}{kgH_0}$$

Here,  $k$  is von Karman's constant with a value of 0.4, and  $H_0$  is the surface heat flux. The function  $\phi$  is a standard representation of the Monin-Obukhov profiles (Businger et al., 1971).

The surface stress derivation has been described explicitly for the flat surface, since we shall extend the definition to the terrain case by assuming the same surface layer relations in the local tangent plane. This is not strictly accurate since the buoyancy effects are controlled by the vertical gravity direction and do not simply rotate with the inclined surface. However, sufficiently close to the surface the profile is logarithmic so if the lowest grid level is close enough to the surface the errors will be negligible. In the calculations reported below, the first grid level is less than 5m above the surface. Clark (1977) uses a simplified treatment of the lower boundary condition, considering only the two vertical flux components for the horizontal momentum, but points out the need for a more careful analysis. The formulation developed below is a more complete representation of the surface layer, and is consistent with the subgrid stress model employed in the LES.

We can use the flat surface relations to determine the tangential stress on the ground, but we must rotate the stress tensor into the Cartesian frame since the momentum equations use the Cartesian velocity components. This procedure requires a definition of the full tensor in the local frame defined by the tangent plane and the direction of the tangential velocity, which we take as

$$\bar{\tau} = u_*^2 \begin{pmatrix} 0 & 0 & 1 \\ 0 & 0 & 0 \\ 1 & 0 & 0 \end{pmatrix} \quad (5.22)$$

with  $u_*$  obtained from the tangential velocity at the lowest grid level. The neglect of the other tensor components is consistent with the subgrid stress model, since the diagonal stress components become isotropic near the wall. The frame rotations do not change the isotropic part of the tensor and it can therefore be neglected. In a real flow, the stress tensor is not isotropic near a wall but the description of these effects requires a more sophisticated subgrid closure model. We expect the tangential stress to provide the dominant momentum transfer, but the detailed Reynolds stress behavior near the wall should be a topic for future study.

When the stress tensor is rotated into the Cartesian frame, we obtain

$$\tau_{ij} = u_*^2 (\hat{u}_i n_j + \hat{u}_j n_i) \quad (5.23)$$

where  $\hat{u}$  is the unit vector aligned with the wind (parallel to the surface) and  $n$  is the unit normal to the surface.

The consistency and accuracy of the surface boundary condition was tested by means of a simple flow solution for a plane channel. The solution involves a slight modification to the terrain transformation described above, so that the flow in the two geometries shown in Figure 5-1 could be calculated. The turbulence scale,  $\Lambda_{\max}$ , was set equal to  $H$  so that there are no resolved eddies and we compute a standard mixing length solution for the channel profile. The flow equations involve no buoyancy or Coriolis terms but are driven by a streamwise pressure gradient, giving a horizontally homogeneous solution with no velocity component normal to the walls. By arranging for the normal distance between the two plates to be identical, the two solutions should be related via a simple rotation.

Profiles of the mean velocity and the subgrid Reynolds stress components for the two solutions are shown in Figure 5-2. The predictions from the rotated channel have been rotated into the frame of the Cartesian solution and show very good agreement throughout the flow. Correct prediction of the subgrid kinetic energy close to the wall required careful treatment of the shear production term at the lowest grid location where

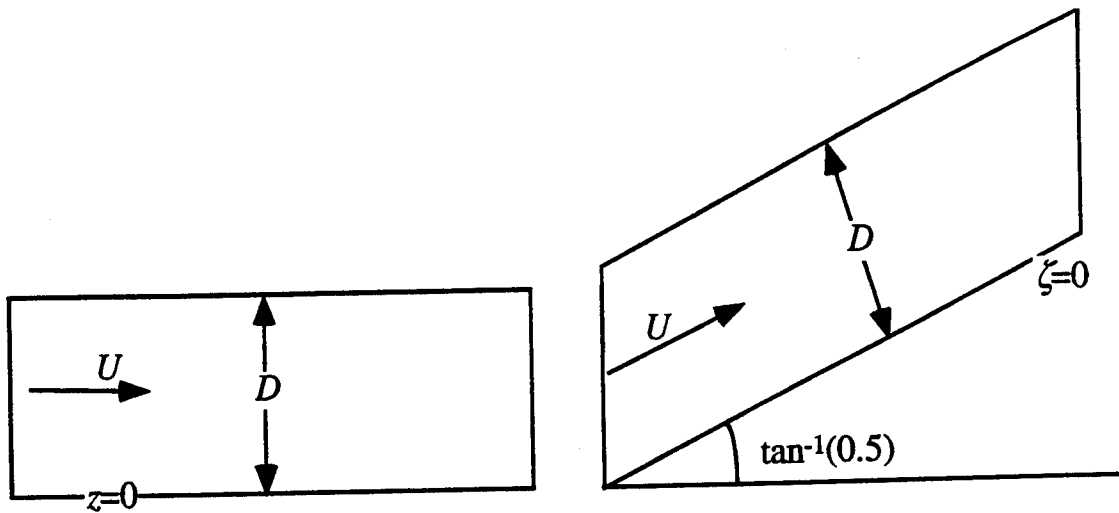


Figure 5-1. Schematic geometry of the horizontal and inclined channel.

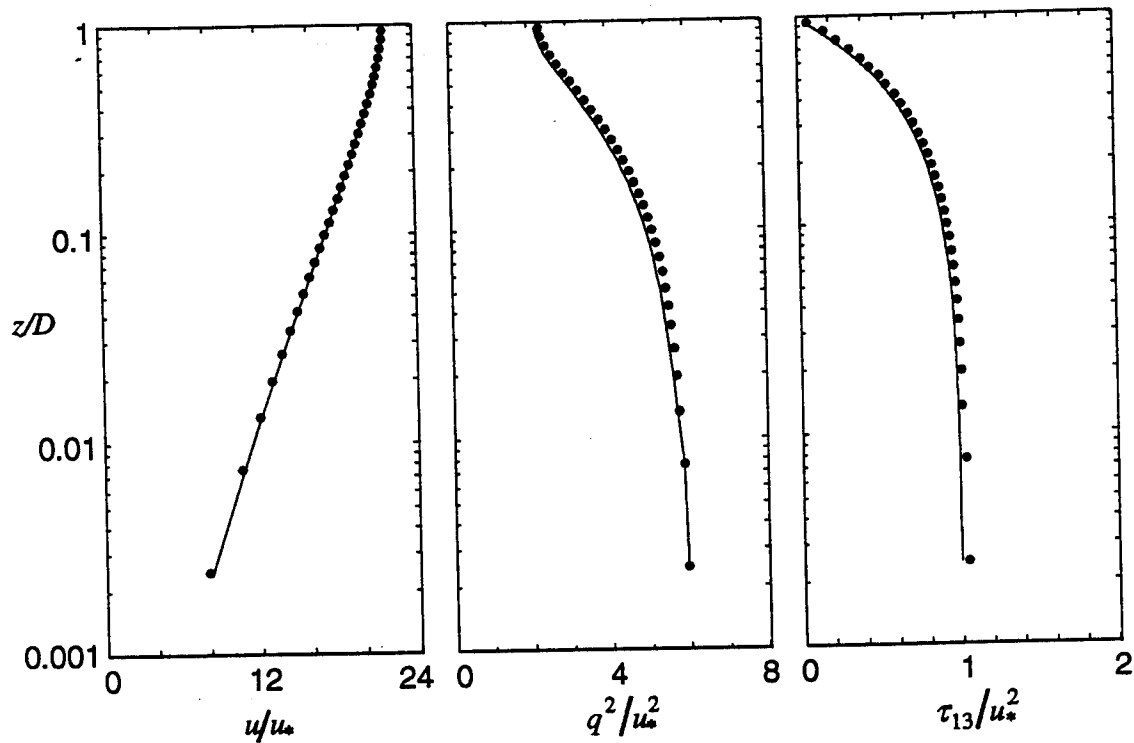


Figure 5-2. Normalized mean velocity and subgrid Reynolds stress profiles from the two geometries in Figure 5-1. Solid line is the horizontal channel result, symbols indicate inclined channel.

velocity derivatives at the surface must be estimated. The estimate was obtained from an extrapolation of the derivative in the flow to maintain consistency with the log-layer profile. In summary, consideration of the rotated Reynolds stress shows that all the tensor components are important at the surface, and the idealized solution for a rotated channel demonstrates that the model boundary conditions and finite-difference approximations provide a consistent representation of the log-layer solution on an inclined surface, with a smooth match to the surface conditions.

The surface heat flux is simpler to deal with, since we only need consider rotations of a vector. We have chosen to apply a constant heat flux condition at the surface, and interpret the flux as being specified for a unit surface area. This implies a slightly higher heat input through the distorted terrain surface due to the area increase. In fact, a zero slope condition is applied to the horizontal temperature fluxes at the surface, and the entire normal flux is input through the  $H_3$  component at  $\zeta = 0$ . Zero slope conditions are also applied to the turbulent kinetic energy equation, although this is not critical since the surface layer is dominated by the balance between shear production and the dissipation.

### 5.3 FLOW PARAMETERS AND FORCE BALANCE.

The topography used in this study is a simple sinusoidal ridge, i.e.

$$h(x, y) = \frac{h_0}{2} \left( 1 - \cos \frac{2\pi x}{\lambda} \right) \quad (5.24)$$

where  $\lambda$  is the wavelength and  $h_0$  is the maximum height. The maximum slope of this terrain is  $\pi h_0 / \lambda$  in the  $x$ -direction, and the flow is statistically homogeneous in the  $y$ -direction. We restrict attention to this idealized terrain for our initial studies, and hope to develop a general framework of understanding that can be extended to more complex terrain.

The specification for the domain of integration is a horizontal square of dimension  $L$ , and a vertical range from  $z=h(x,y)$  up to  $z=D$ . All of the integrations reported here use  $L=D=4\text{km}$  and were chosen to represent a mixed layer depth,  $z_i$ , of roughly 1km. The vertical grid extends far enough for the upper wave-damping layer to have no significant effect on the flow. The numerical grid is uniform in the horizontal, with 48 points in each

direction, but non-uniform in the vertical. Most of the integrations used 61 points in the vertical, with 10m spacing near the surface, 40m in the mixed layer, and an expanding mesh above  $\zeta=1200\text{m}$ .

The flow was initialized with the geostrophic wind and a uniform vertical temperature gradient of  $5^\circ\text{Ckm}^{-1}$  above  $\zeta=800\text{m}$ ; a constant temperature and a specified 'boundary layer' horizontal wind were prescribed below  $\zeta=800\text{m}$ . The initial conditions were chosen to provide an initial well-mixed layer with an average boundary layer velocity close to the final steady state. The initial conditions are not critical, but we need to maintain an appropriate resolution during the evolution of the flow, so we require the initial mean fields to be reasonably close to the final state. The flow is maintained through the constant geostrophic wind vector  $(u_g, v_g)$  in (5.5). The turbulence is initiated by a small random perturbation of the temperature field, and the surface heat flux is linearly increased from zero to its specified value over the first 2000s of the integration. Vertical velocities are initialized to zero, but the pressure solution ensures zero divergence after one time-step so mass continuity is assured. This procedure does induce an initial transient response but this does not persist long in the presence of the convective eddies. The convective circulations generally require about 3000s to reach statistical equilibrium (for the parameters considered in these calculations), but the overall boundary layer profiles take much longer to achieve the balance between Coriolis and friction effects. The details of the initialization procedure are virtually eradicated during the initial growth of the convective eddies.

One of the most important effects of non-uniform terrain on the large-scale atmospheric flow is the surface momentum flux balance over small-scale features. For the periodic conditions of the large-eddy simulation domain, integration of the momentum conservation equation over the entire volume yields

$$\int_V \frac{\partial u}{\partial t} dV = -f \int_V (v - v_g) dV + L^2 F_x \quad (5.25a)$$

$$\int_V \frac{\partial v}{\partial t} dV = +f \int_V (u - u_g) dV + L^2 F_y \quad (5.25b)$$

where  $F_x$  and  $F_y$  are the average surface momentum fluxes of  $x$ - and  $y$ -momentum per unit area (and per unit fluid density since we have ignored the density in the Boussinesq

equation). The surface momentum fluxes are composed of a shear stress component and a pressure component, so that  $F_x = T_x + P_x$ , and  $F_y = T_y$ , where

$$T_x = \frac{1}{L^2} \int_S (\tau_{11}n_1 + \tau_{13}n_3) dS \quad (5.26a)$$

$$T_y = \frac{1}{L^2} \int_S (\tau_{12}n_1 + \tau_{23}n_3) dS \quad (5.26b)$$

$$P_x = -\frac{1}{L^2} \int_S p n_1 dS \quad (5.26c)$$

Here  $\underline{n}$  is the unit normal at the surface,  $S$  where  $\zeta=0$ . Momentum fluxes at the lateral boundaries cancel due to periodicity, and the stress-free rigid lid at  $\zeta=D$  implies zero flux through the upper boundary.

If we define a boundary depth,  $z_i$ ; then we can also define a mean boundary layer velocity deficit.

$$u_B - u_g = \frac{1}{z_i L^2} \int_V (u - u_g) dV \quad (5.27)$$

and similarly for  $v_B$ .

The velocity  $(u_B, v_B)$  will be representative of the bulk mean boundary layer velocity provided that most of the deficit occurs below  $z = z_i + h_0 / 2$ . The displacement,  $h_0/2$ , is the average displacement of the terrain. Given the sharp inversion cutoff for the turbulent stresses, the perturbations above  $z_i$  are small and are only maintained by gravity wave transports. In the steady state situation, a simple geostrophic balance is obtained,

$$f z_i (v_B - v_g) = T_x + P_x \quad (5.28a)$$

$$f z_i (u_B - u_g) = -T_y \quad (5.28b)$$

This balance between the Coriolis force and the momentum flux is well-known in oceanographic transport, e.g. Gill (1982). We use this steady-state relation to determine the validity of our numerical solution, continuing the calculation until the balance is achieved within a specified tolerance.

Integrations have been made for a range of external parameters, including surface roughness ( $z_0$ ), terrain wavelength ( $\lambda$ ), terrain height ( $h_0$ ), and flow stability and direction. This large number of independent parameters prevents a detailed investigation

of the entire parameter space, but some variation of each has been considered. The flow stability is measured by the ratio  $w_*/U_g$ , where

$$U_g^2 = u_g^2 + v_g^2$$

and

$$w_*^3 = \frac{g}{T_0} H_0 z_i$$

$w_*$  is the usual convective velocity scale (Deardorff, 1972) and  $H_0$  is the surface flux of potential temperature. The nominal inversion height,  $z_i$ , for all the runs presented below is 1000m.

## 5.4 SURFACE FORCE RESULTS.

The series of runs was designed to provide information for a range of atmospheric flow conditions. We examine the various effects of terrain geometry, surface roughness, atmospheric stability, and wind direction, although the breadth of the parameter space prevents exhaustive definition. The major features to be presented will be the changes in the surface force balance and mean boundary layer flow induced by the terrain. The standard flow situation will be a  $5\text{ms}^{-1}$  geostrophic wind perpendicular to the ridges, with a surface heat flux of  $0.03^\circ\text{Cms}^{-1}$  and a surface roughness of 1m; variations from these values will be specified where appropriate.

### 5.4.1 Terrain Geometry Effects.

Since we are considering only sinusoidal ridges, there are two defining parameters which we choose as the horizontal wavelength,  $\lambda$ , and the maximum slope,  $s=\pi h_0/\lambda$ . We consider wavelengths of 1km, 2km, and 4km relative to the normal inversion height of 1km, and slopes up to 0.5. We first examine the mean flow characteristics in the quasi-steady state, where the average Coriolis force is nearly balanced by the surface stresses.

Figure 5-3 shows the mean flow over ridges with maximum slope of 0.5 and  $\lambda=2\text{km}$ . The mean streamlines show a clear reversed flow in the valley and acceleration over the ridge crests, as expected, but the separated flow regions in the two valleys are different. The difference between the two waves indicates the reliability of the averaging

procedure and shows that the reversed flow region contains large variability. The streamlines show little evidence of any disturbance in the overlying atmosphere; the flow separation effectively allows the boundary layer to accommodate the vertical displacements without significantly disturbing the stable region. The transverse velocity component,  $v$ , shows a relatively well-mixed profile with little response to the local terrain. This is to be expected, since the transverse velocity is forced by the Coriolis terms which act on a slow timescale in comparison with the hill transit times. The  $v$ -component therefore represents an average response and does not exhibit much correlation with the local terrain variations.

An example of the instantaneous flow structure that contributed to the average fields in Figure 5-3 is given in Figure 5-4. The near-surface streaklines, obtained by calculating trajectories in the instantaneous  $(u,v)$ -field at 10m above the surface, show the distinct separation region between the two ridges. The predominant flow near the surface is in the positive  $y$ -direction, except over the hill crests where the  $u$ -component is accelerated. As noted in the mean flow, the  $v$ -component is relatively constant over the ridges so the low velocity reversed flow in the  $x$ -direction results in flow along the valley axis. The separation and reattachment lines are readily visible in the instantaneous plot over most of the domain. The lines are meandered by the large eddies and become very indistinct in places, but the mean flow is clearly evident.

The instantaneous vertical velocity field at  $\zeta=500\text{m}$ , is also shown in Figure 5-4, and resembles the mid-level convective velocity field over flat terrain. There is some suggestion of alignment of the convective updrafts but no visible effect of surface terrain variations. The statistics of the velocity fluctuations are described in Section 5.6.

The surface forces determine many general features of the boundary layer, as discussed previously, and we now examine the variation of the forces with slope and wavelength. We attempt to calculate steady-state forces, although there is always a slow growth of the boundary layer due to the surface heat input. The achievement of steady conditions requires long integration times since the balance between the Coriolis terms and the Reynolds stress gradients is only reached after times of  $O(f^{-1})$ . The actual requirement depends on the choice of initial conditions, but we typically integrate for about  $4f^{-1}$ , i.e. 40,000s. Over this period, the growth in  $z_i$  is significant, so we artificially reduce  $z_i$  during the integration to maintain an inversion height of about 1000m relative to the mean terrain. The procedure simply involves resetting the

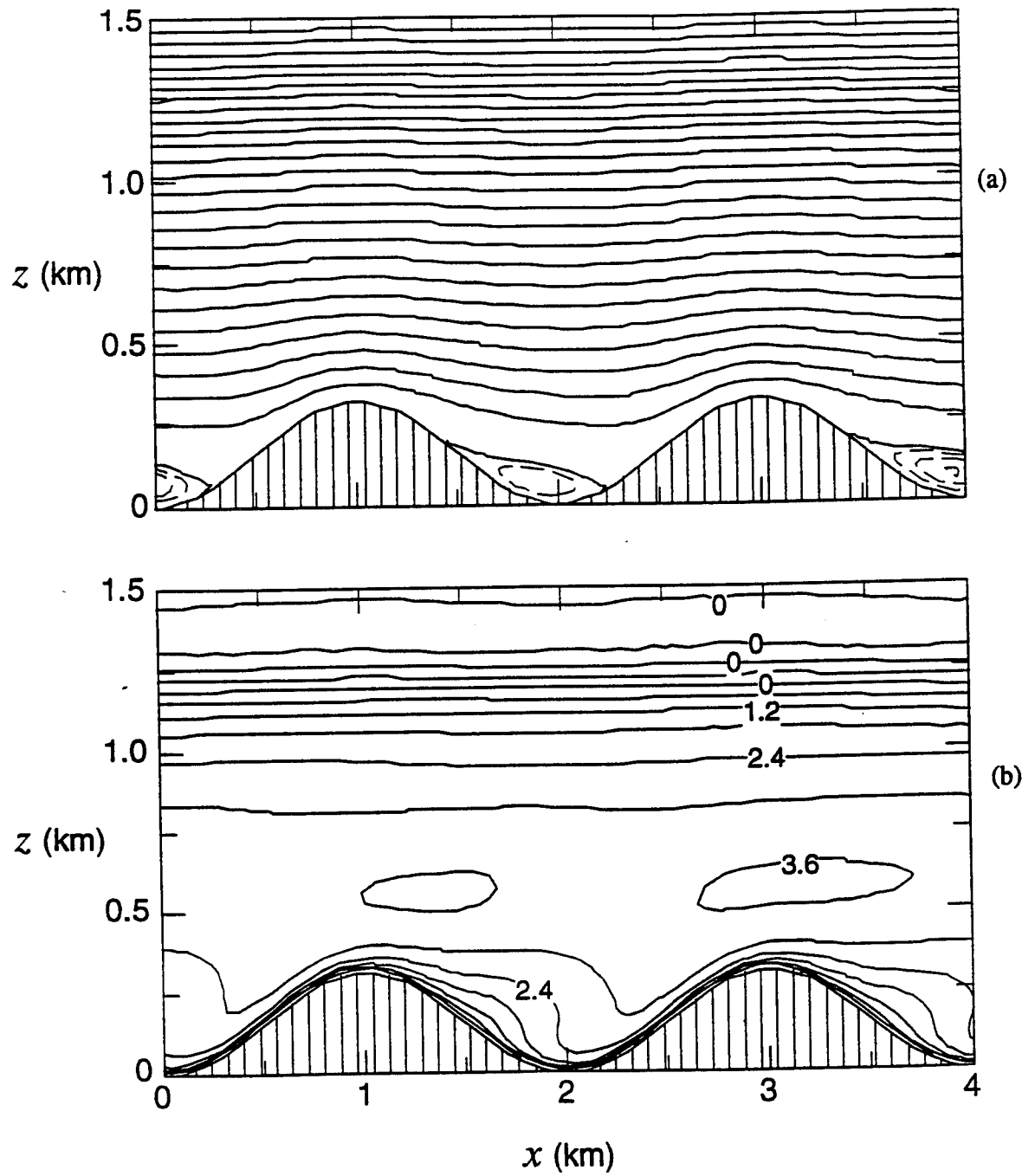


Figure 5-3. Mean flow over 2km ridges with slope 0.5 and  $z_0=1\text{m}$ . (a) mean streamlines, contour interval is  $200\text{m}^2\text{s}^{-1}$  for positive values,  $10\text{m}^2\text{s}^{-1}$  for negative values (shown dashed). (b) mean transverse velocity component, contour interval of  $0.4\text{ms}^{-1}$ .

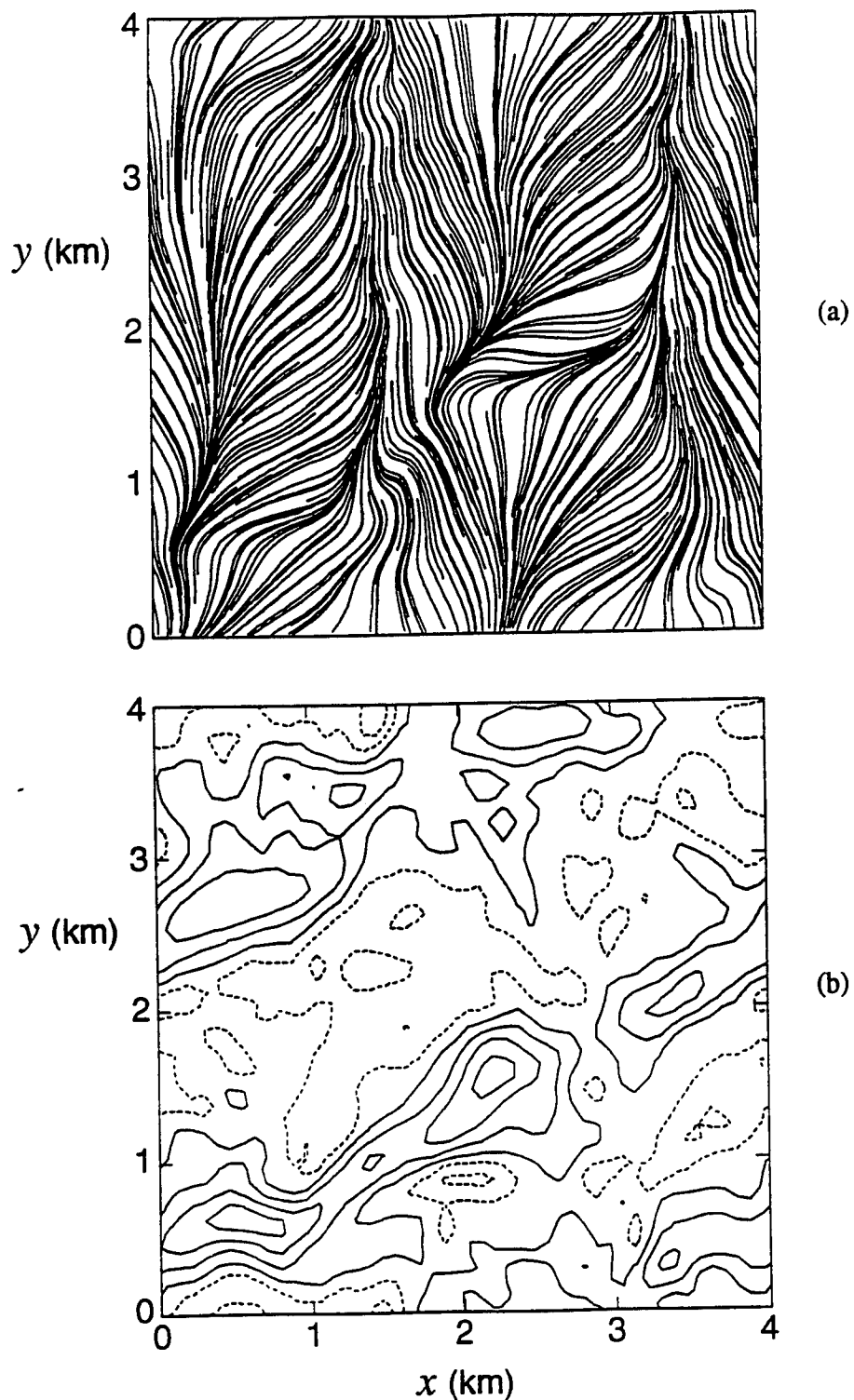


Figure 5-4. Instantaneous flow field over 2km ridges with slope 0.5 and  $z_0=1\text{m}$ .  
 (a) flow streaklines at  $\zeta=10\text{m}$ . (b) vertical velocity component at  $\zeta=500\text{m}$ ,  
 contour interval of  $0.6\text{ms}^{-1}$ , dashed contours denote negative values.

temperature field to the initial, undisturbed condition without changing the velocity fields. This introduces a transient response as the flow readjusts to the new temperature distribution, but allows the mean boundary layer profile to achieve accurate balance over the longer timescale.

Figure 5-5 illustrates the evolution of the instantaneous surface forces over the duration of an integration; the pressure and tangential shear stress components are shown for the  $\lambda=2\text{km}$  terrain with a slope of 0.5 and a reduction in  $z_i$  at  $t=24000\text{s}$ . The forces are averaged over the domain but there are significant temporal fluctuations on the timescale of the large eddies. The surface force results used in the subsequent analysis are averaged over the last 3000s of the run. There is a visible discontinuity in the forces

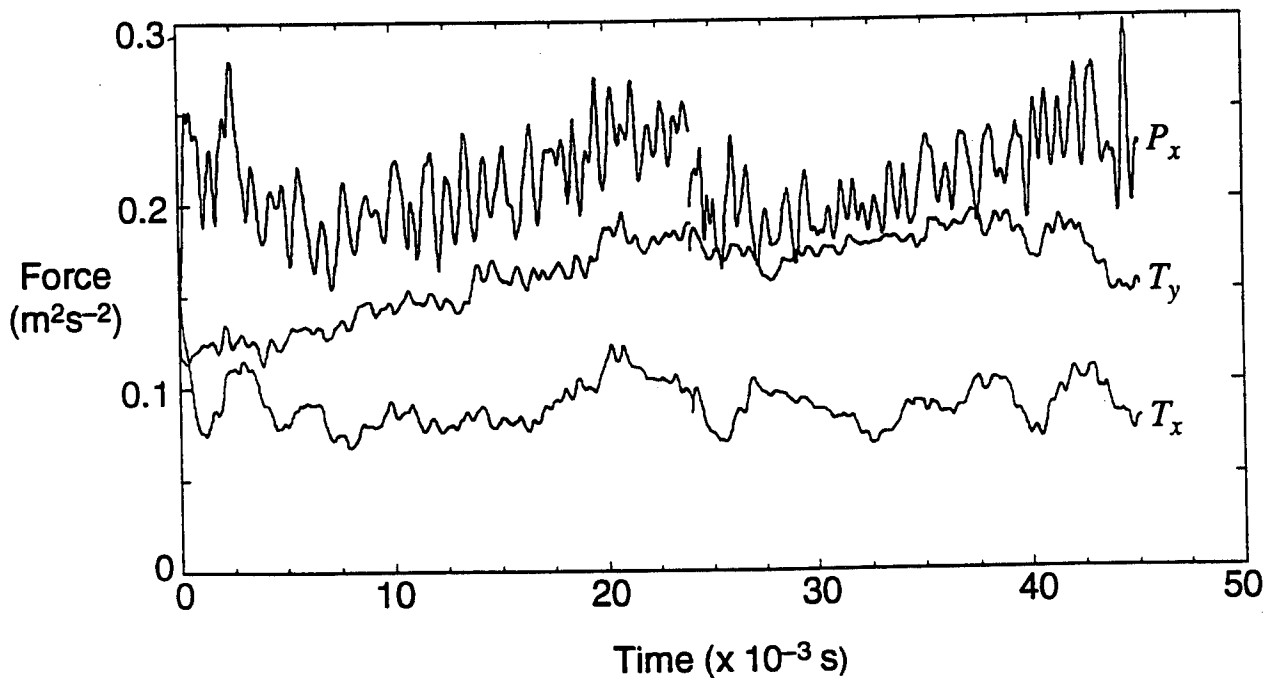


Figure 5-5. Time history of the domain-averaged surface forces for flow over 2km ridges with slope 0.5 and  $z_0=1\text{m}$ . Forces are displayed per unit horizontal surface area and per unit fluid density.

induced by resetting the temperature field at  $t=24000$ s, but this is not large compared with the turbulent fluctuations. The pressure force decreases following the reduction in inversion height, but the forces recover and reach a reasonably steady state. The integrations were generally continued until the balanced state (5.28) was achieved with a tolerance of 10%, i.e., the difference between the left and right sides of (5.28) was less than 10% of the total force magnitude  $(F_x^2 + F_y^2)^{1/2}$ .

The variation of the surface forces with terrain slope for the 2km wavelength ridges is shown in Figure 5-6(a). The trends are clearly evident; the pressure force increases with slope, as does the lateral stress,  $T_y$ , while the streamwise surface stress,  $T_x$ , tends to decrease with increasing slope. The pressure force is approximately proportional to the square of the slope; each doubling of the slope gives roughly a four-fold increase in  $P_x$ . This is a well known result for small slopes in the linear perturbation regime, but is accurately maintained in the nonlinear flow with a slope of 0.5. However, there seems to be a somewhat fortuitous balance of conflicting trends responsible for this quadratic behavior since there are significant changes in the boundary layer flow for the larger slopes. The variation of the mean boundary layer velocities,  $(u_B, v_B)$  as defined in (5.27), is shown in Figure 5-6(b), where we have used a value of  $z_i=950$ m for the calculation. The large increase in surface drag over steep terrain has reduced the mean boundary layer velocity from  $4.2 \text{ ms}^{-1}$  with no topography to  $3.3 \text{ ms}^{-1}$  in the  $x$ -direction, while the  $v$ -component increases from  $1.8 \text{ ms}^{-1}$  to  $3.5 \text{ ms}^{-1}$ . This increased deflection of the boundary layer flow due to the Coriolis effect is responsible for the increase in  $T_y$  seen in Figure 5-6(a).

The proportionality between  $P_x$  and the square of the slope is surprising in light of the reduction in  $u_B$ , since we would expect the pressure to vary with the square of the streamwise velocity. However, the increasing height of the terrain with slope introduces two flow effects which act to increase the pressure force. First, there is some tendency for the mean velocity to increase with height above the surface, so that a higher terrain will be exposed to a higher velocity for a fixed bulk mean velocity. Second, the capping inversion acts almost like a rigid lid, as shown in the mean flow in Figure 5-3. This implies an increased speed-up for higher terrain due to the constriction effect, and a correspondingly larger pressure force. The combination of these conflicting effects to produce a quadratic variation with slope must be regarded as somewhat fortuitous. We

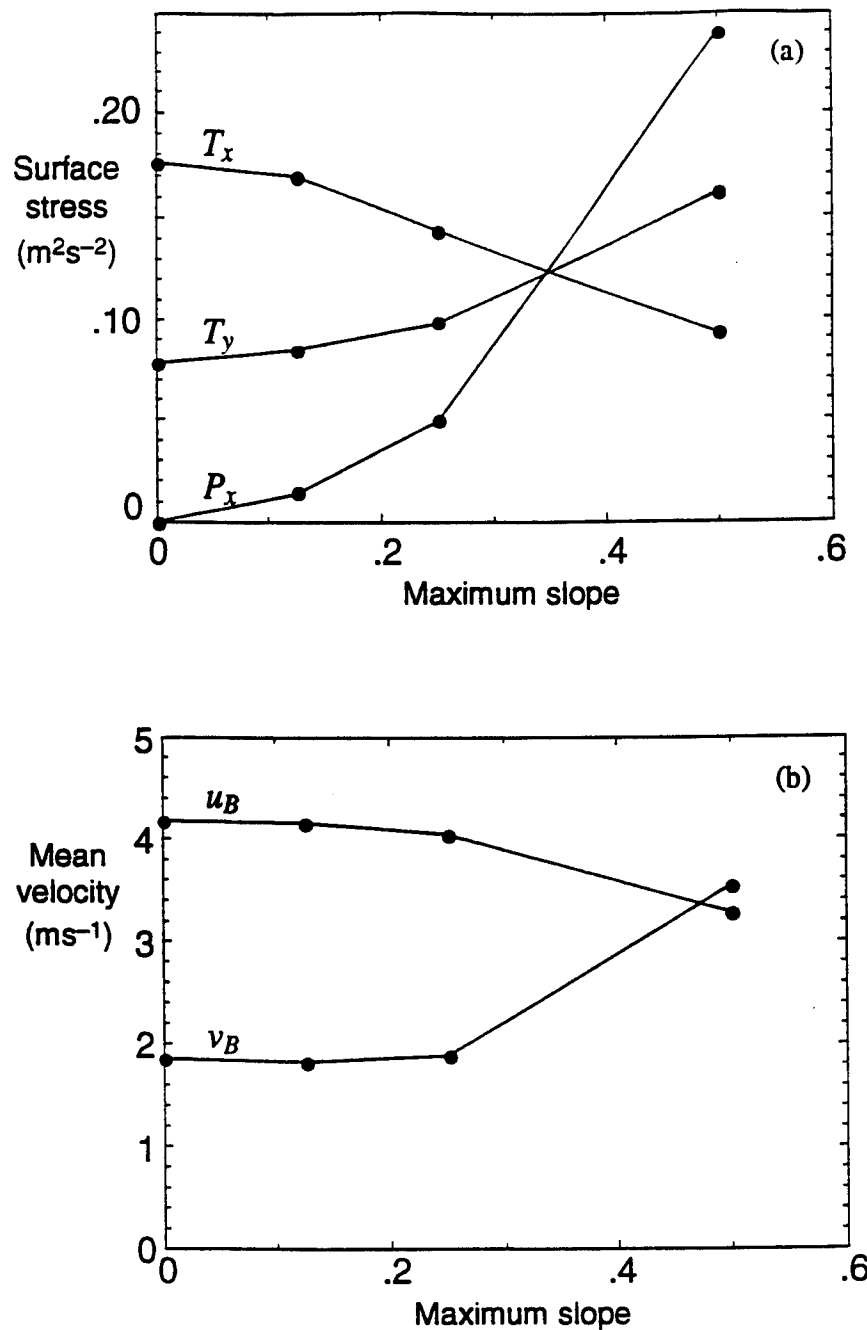


Figure 5-6. Variation of surface forces and mean boundary layer velocity with terrain slope for 2km ridges and  $z_0=1m$ . (a) average pressure force ( $P_x$ ), and tangential stress forces ( $T_x$ ,  $T_y$ ) per unit area. (b) mean boundary layer velocity components ( $u_B$ ,  $v_B$ ).

shall return to the problem of parameterizing the forces on ridges after we have examined the results for other parameter variations.

The flow dependence on the height of the terrain, measured by the ratio,  $h_0/z_i$ , is more clearly examined by varying the wavelength of the ridges but holding the slope constant. Runs were made with wavelengths of 1, 2, and 4km at a maximum slope of 0.5 and surface roughness length of 1m. This implies maximum terrain heights,  $h_0$  of 159m, 318m, and 636m respectively. The mean streamlines for the 4km wavelength ridge are shown in Figure 5-7. It is clear that the blockage effect of the ridge induces a significant acceleration of the flow over the crest relative to that over the valley, although the large separation zone reduces the effective vertical displacement of the streamlines. The  $\tau_{13}$ -component of the surface stress is shown in Figure 5-8 for all three wavelengths, and illustrates the variation of the stress perturbation with wavelength. The separation region is more extensive for the 4km ridges but the peak stress at the crest is actually lower than the shorter wavelengths. This is a result of the reduction in  $u_B$  in combination with a larger constriction effect for the 636m hill. Profiles of the mean  $u$ -component over the

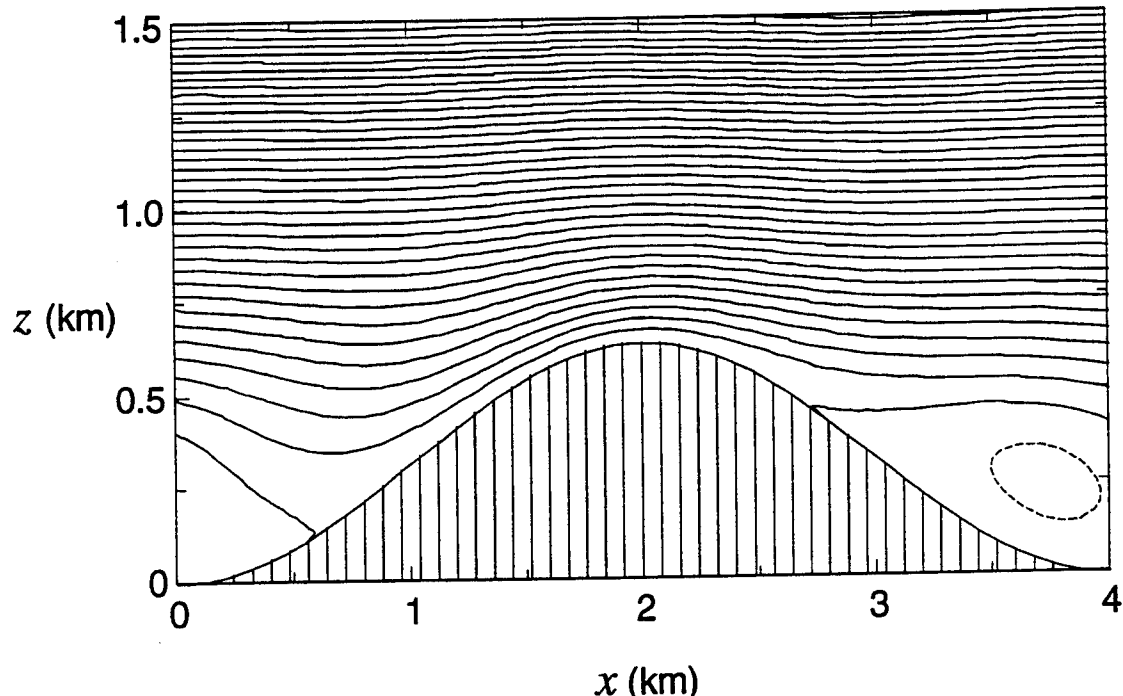


Figure 5-7. Mean streamlines for flow over a 4km ridge with slope 0.5 and  $z_0=1\text{m}$ . Contour interval is  $100\text{m}^2\text{s}^{-1}$ .

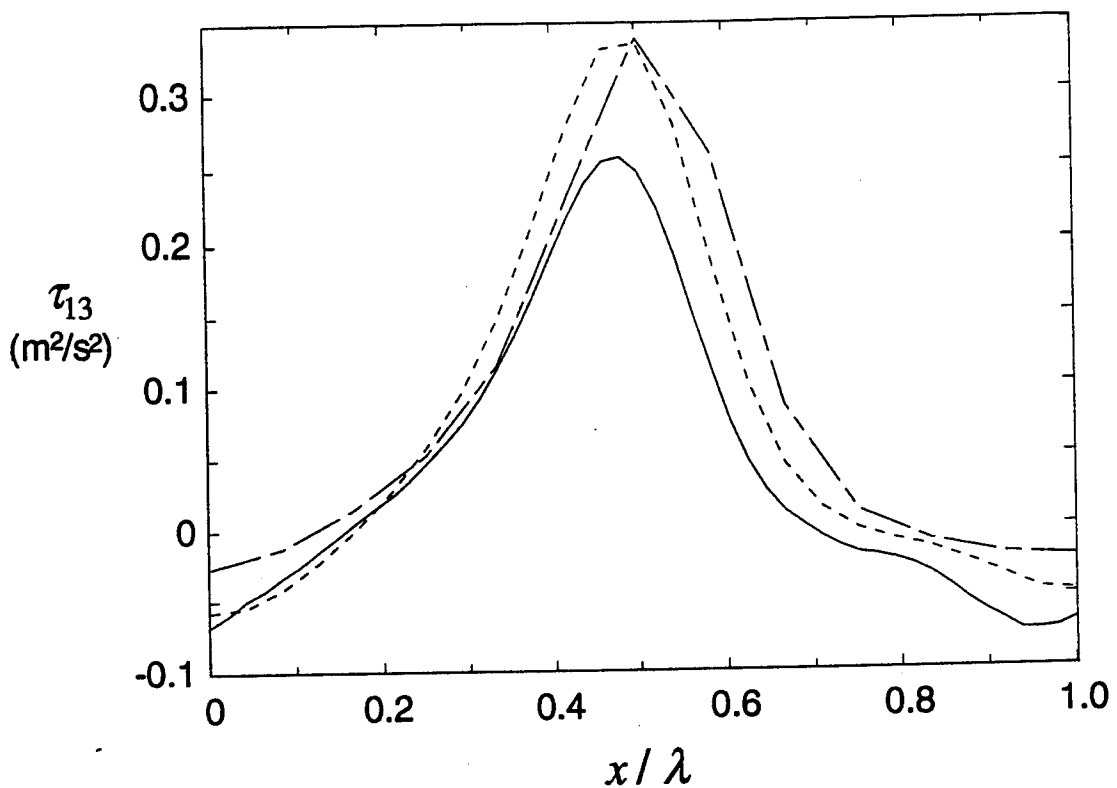


Figure 5-8. Surface variation of the  $\tau_{13}$  stress component for three terrain wavelengths with slope 0.5 and  $z_0=1\text{m}$ . — — —  $\lambda = 1\text{km}$ ,  
- - - - -  $\lambda = 2\text{km}$ , — — —  $\lambda = 4\text{km}$ .

hill crest for the three wavelengths are shown in Figure 5-9. The shorter wavelength hills produce an accelerated flow close to the surface, which is responsible for the larger surface stress at the crest, while the 4km wavelength shows no evidence of a low-level maximum but has a higher speed in the main boundary layer. The limited vertical extent of the aerodynamic pressure gradient, being controlled by the horizontal wavelength, is probably responsible for the localized acceleration over the shorter wavelength ridges.

The variation of the area-averaged surface forces is illustrated in Figure 5-10. The pressure force increases significantly with wavelength as a result of the increased velocity over the crests of the higher ridges, while the shear stress force decreases due to the enhanced sheltering effect. The total force in the  $x$ -direction increases with wavelength. These results suggest a parameterization of the forces in terms of effective boundary layer velocities, and we shall pursue the specification of the appropriate velocity in Section 5.5.

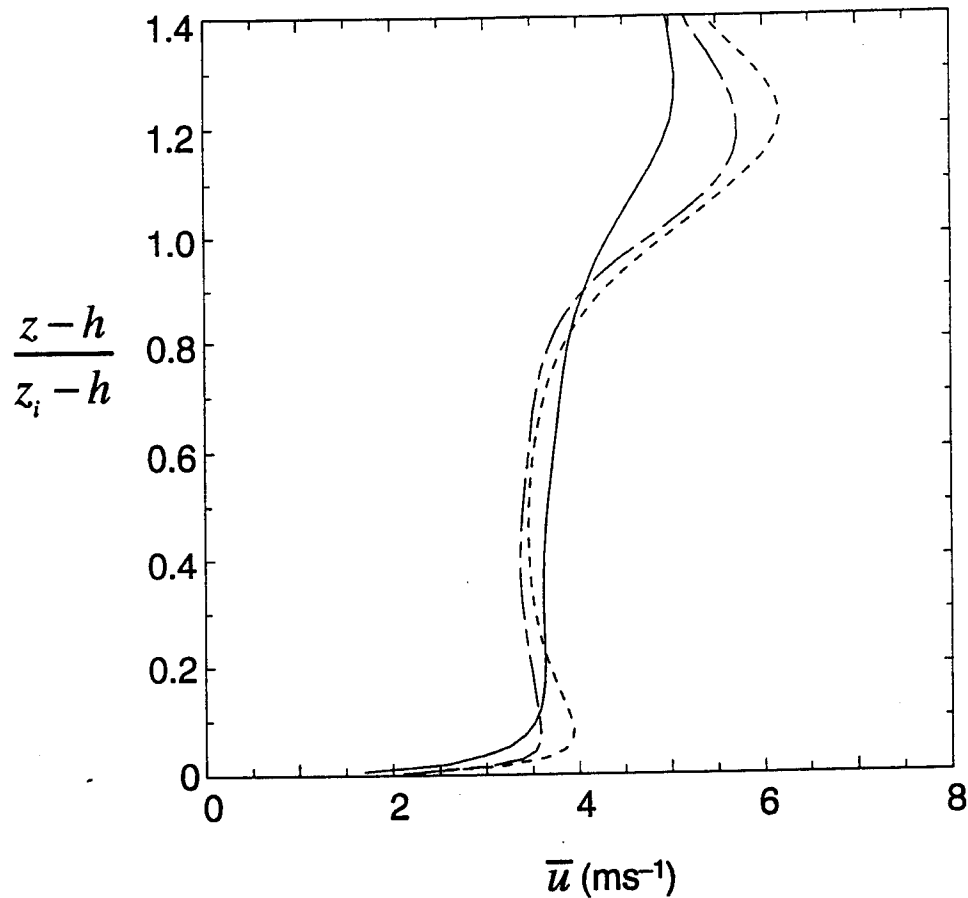


Figure 5-9. Vertical profiles of the mean velocity component normal to the ridge at the crest for three terrain wavelengths with slope 0.5 and  $z_0=1\text{m}$ . The vertical scale is normalized by the inversion depth to facilitate comparison.

———  $\lambda = 1\text{km}$ , - - - - -  $\lambda = 2\text{km}$ ,  
 —————  $\lambda = 4\text{km}$ .

#### 5.4.2 Variation With Surface Roughness.

The character of the local surface affects the details of the surface layer profile and has a strong influence on the surface momentum flux for flat terrain. In the case of free convection, however, surface roughness has a limited influence in the near-surface region; the bulk of the boundary layer turbulence is unaffected (Schumann, 1988; Sykes, Henn and Lewellen, 1993). We examine the flow over 2km wavelength ridges at a slope of 0.5 with  $z_0=0.01\text{m}$ ,  $0.1\text{m}$ , and  $1\text{m}$ , to determine the response of the flow field and the surface forces.

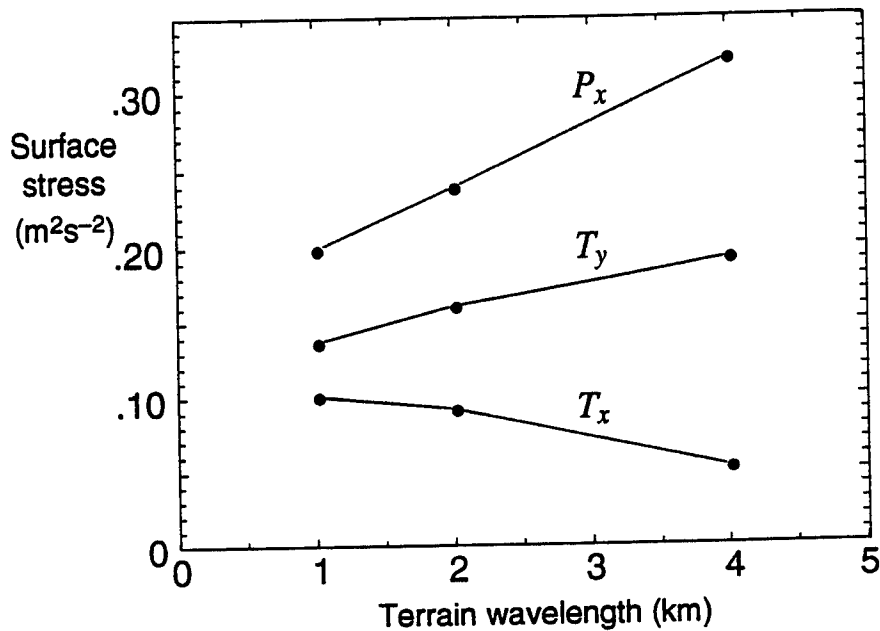


Figure 5-10. Variation of average surface forces with terrain wavelength for slope 0.5 and  $z_0=1\text{m}$ .

Figure 5-11 presents the streamwise surface stress component normalized by the flat terrain value,  $T_{0x}$ , and shows the effects of surface roughness.  $T_{0x}$  is the value of  $T_x$  for flow over flat terrain with the same geostrophic wind and surface heat flux. Flow separation is sensitive to surface roughness, with a pronounced region of reversed flow over the  $z_0=1\text{m}$  surface but no separation over the lower roughness terrain. The peak stresses are also reduced over the large roughness ridges, but this is probably due to the reduction in  $u_B$  in this case. The trend with roughness seems consistent with the dependence derived by Hunt et al. (1988) for neutral flow, where shear effects were shown to enhance the surface stress response for larger roughness lengths. A slope of 0.5 is relatively steep, and the attached flow for the smaller roughness cases is probably due to the mixing effect of the unstable temperature profiles. The turbulent eddy viscosity in the convective layer is larger than the neutral case, and therefore reduces the effective Reynolds number of the flow and inhibits separation.

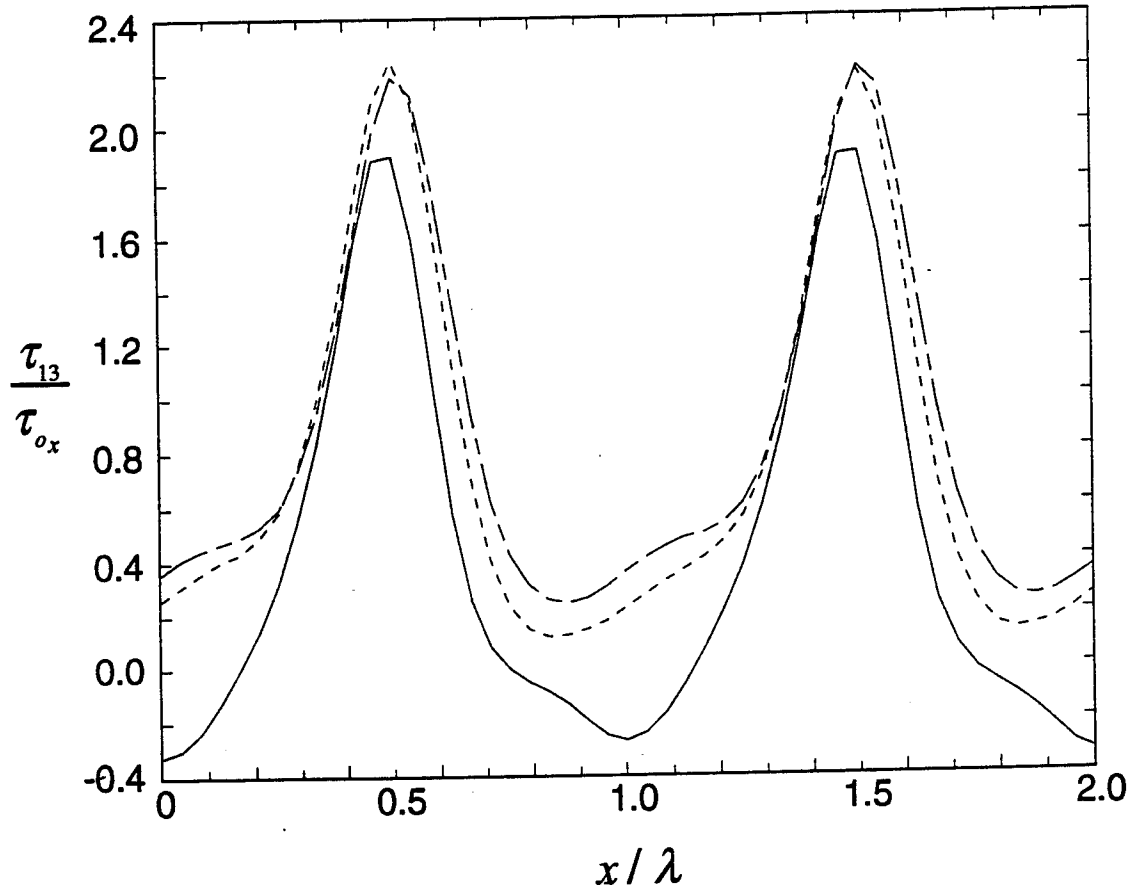


Figure 5-11. Surface variation of the  $\tau_{13}$  stress component for three surface roughness lengths and 2km ridges with slope 0.5.. —  $z_0 = 0.01\text{m}$ , - - -  $z_0 = 0.1\text{m}$ , —  $z_0 = 1\text{m}$ .

The surface forces, normalized by the equivalent flat terrain force, are shown in Figure 5-12. The normalized pressure force is strikingly independent of  $z_0$  for slopes of both 0.25 and 0.5, while the shear stress force shows a slight reduction at the higher roughness value. This result is in contrast to the various model studies for neutral flow over ridges (see e.g., Taylor et al., 1989), which show a significant dependence on roughness. The roughness effect, however, is thought to be due to shear-enhancement (Hunt et al., 1988) and is not present in the asymptotic theory of Sykes (1980). We hypothesize that the shear is reduced under the strongly convective conditions of the LES, and hence there is less variation of the forces with surface roughness. We should note, however, that the surface stress variation shown in Figure 5-11 does exhibit a

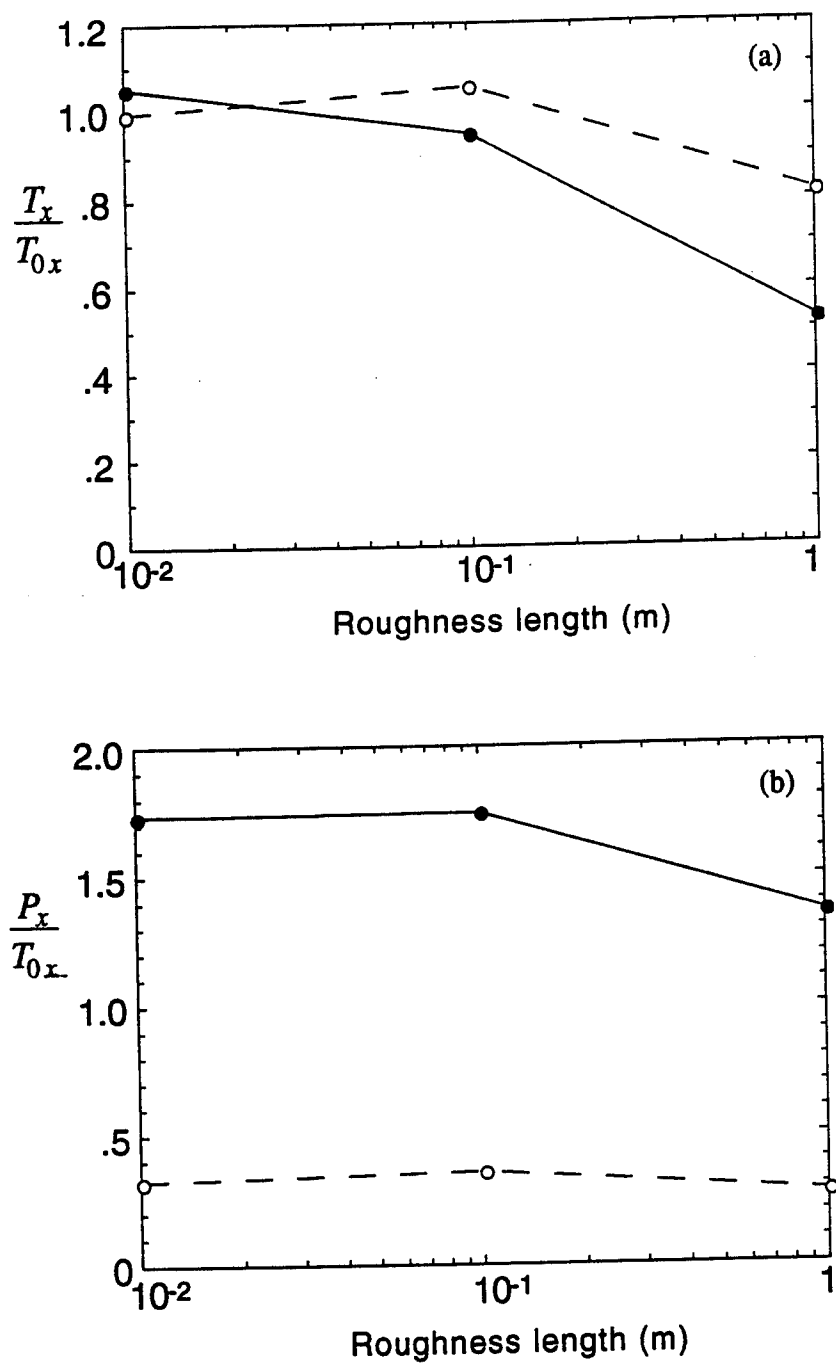


Figure 5-12. Normalized surface force variation with roughness for flow over 2km ridges with slope 0.5. (a) tangential stress component in the  $x$ -direction. (b) pressure force. Solid line and symbol is slope 0.5, dashed line and open symbol is slope 0.25.

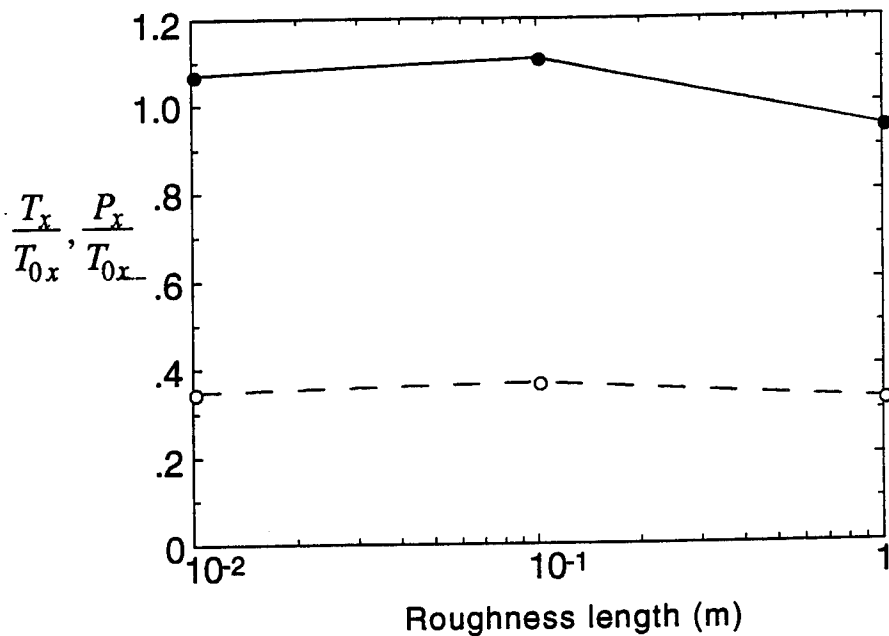


Figure 5-13. Normalized surface force variation with roughness for flow over 1km ridges with slope 0.25 and small surface heat flux,  $H_0=0.0045^{\circ}\text{Cms}^{-1}$ .

roughness dependence. We have performed a small number of calculations with smaller surface heat flux and these results will be examined in the next section to determine the effect of stability.

#### 5.4.3 Effect of Boundary Layer Stability.

The flow parameters of the previous sections are generally close to free convection conditions. The average friction velocity for the flat terrain cases was between  $0.28\text{ms}^{-1}$  and  $0.4\text{ms}^{-1}$  while the convective velocity scale,  $w_* = 1\text{ms}^{-1}$ . A number of integrations were made with  $w_* = 0.5\text{ms}^{-1}$  to examine the dependence on stability. These flows still have significant buoyancy effects, so are expected to be different from the neutral case, but we expect shear-induced phenomena to be comparable with the convective dynamics.

A series of runs was made with  $\lambda = 1\text{km}$  and a maximum slope of 0.25 to investigate the effects of surface roughness. The surface force results are presented in Figure 5-13, normalized by the flat surface  $x$ -stress value, and show close agreement with the higher heat flux force values. The flat stress value is  $0.119\text{m}^2\text{s}^{-2}$ , as compared with

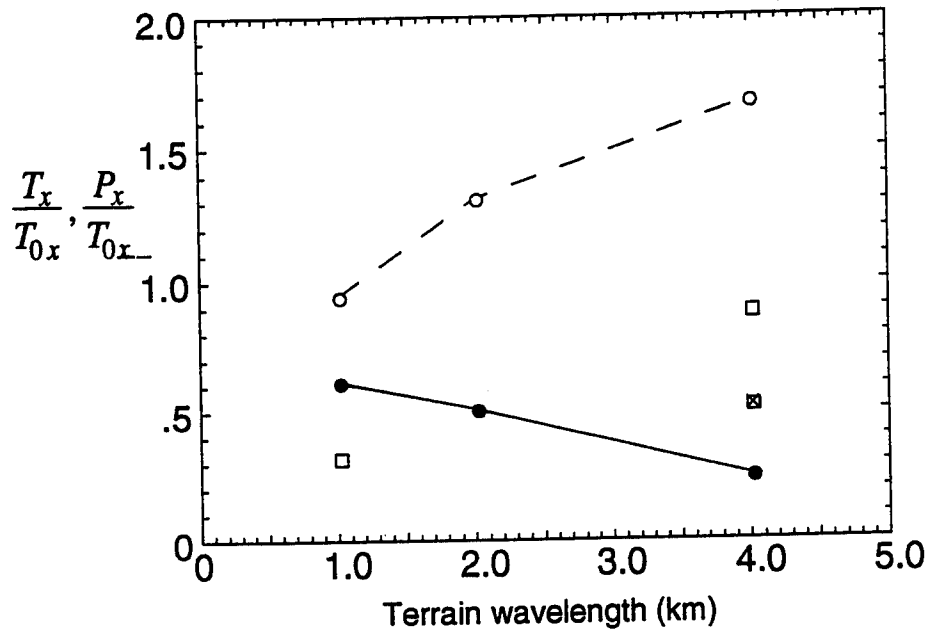


Figure 5-14. Surface force variation with wavelength for flow over ridges with small surface heat flux,  $H_0=0.0045^{\circ}\text{Cms}^{-1}$ , and  $z_0=1\text{m}$ . Solid line and symbol is  $T_x/T_{0x}$ , dashed line and open symbol is  $P_x/T_{0x}$ , both for slope 0.5. Open squares are  $P_x/T_{0x}$  for slope 0.25; open square with cross is  $(P_x + uw_{wave})/T_{0x}$  for slope 0.25.

0.176 $\text{m}^2\text{s}^{-2}$  for  $H_0=0.03^{\circ}\text{Cms}^{-1}$ , but the pressure force shows the same normalized value and is also relatively constant with surface roughness. Thus, with an unstable layer characterized by  $L$  approximately equal to  $z_i$ , we obtain the same qualitative result as with  $L$  much less than  $z_i$ . The expected dependence on roughness for neutral flow is evidently not manifested until the stability is further reduced. It is possible that the LES may not be able to resolve the neutral surface layer adequately (Mason and Thompson, 1992) and that our low heat flux results are affected by this deficiency. However, our LES results are self-consistent and are certainly modified by the buoyancy effects, preventing direct application of the neutral layer predictions. A detailed simulation of the neutral layer and its transition to a buoyancy dominated flow is beyond the scope of the present investigation, but will be necessary to complete the description of stability effects.

The variation of the surface forces with terrain wavelength and slope is shown in Figure 5-14, and indicates an anomalous pressure force at  $\lambda = 4\text{km}$  and slope 0.25. The forces are normalized by the flat terrain value and generally compare very well with the

higher heat flux results, but the normalized pressure force at  $\lambda = 4\text{km}$  and a slope of 0.25 is almost twice the expected value. The reason for this anomaly is immediately clear upon examination of the mean flow, as presented in Figure 5-15. The boundary layer features are very similar to previously described results, but there is a very distinct steady gravity wave above the inversion. The vertical profile of horizontally-averaged momentum flux,  $\overline{uw}$ , is shown in Figure 5-16 and indicates a gravity wave stress of  $0.043\text{m}^2\text{s}^{-2}$  due to the standing wave; this can be compared with the total surface pressure force stress of  $0.106\text{m}^2\text{s}^{-2}$ . Contributions from the other components, that is, the resolved and subgrid fluctuation correlations, are seen to be negligible above the inversion. When the wave stress value is subtracted from the total pressure force for the  $\lambda = 4\text{km}$  case the normalized force matches very closely with the higher heat flux cases; the boundary layer pressure force contribution is indicated by the cross in the open square in Figure 5-14. This is the appropriate force for determining the mean boundary layer velocity profiles, because the relationship (5.28) implicitly assumes zero stress at the top of the turbulent layer. A more general integral of the momentum equation gives

$$f(u_B - u_g) = \frac{(F_x - F_i)}{z_i} \quad (5.29)$$

where  $F_i$  represents the average Reynolds stress at the inversion. This is precisely the gravity wave momentum flux above the mixed layer, so the difference between this and the surface force gives the correct momentum balance.

It is interesting that only one case generates a significant gravity wave stress in comparison with the surface pressure force. The Brunt-Vaisala frequency,  $N$ , where

$$N^2 = \frac{g}{T_0} \frac{\partial T}{\partial z}$$

is a cutoff frequency for the waves; higher frequency forcing of the stable layer produces evanescent disturbances. Thus, the critical wavelength for a wind speed of  $5\text{ms}^{-1}$  and a potential temperature gradient of  $5^\circ\text{Ckm}^{-1}$ ,  $2\pi U/N$ , is approximately  $2.5\text{km}$ . It is not surprising, therefore, that we only see a significant wave response for  $\lambda = 4\text{km}$  but clearly the wavelength is not the only factor of importance. The larger amplitude terrain, maximum slope of 0.5, produces a strong separation between the ridges and therefore reduces the streamline displacement in the main boundary layer, similar to that in Figure 5-7. The separation evidently modifies the boundary layer flow enough to cause a net reduction in the inversion displacement, and the wave stress is reduced to  $0.015\text{m}^2\text{s}^{-2}$  in comparison with a surface pressure stress of  $0.2\text{m}^2\text{s}^{-2}$ . It is also noteworthy that the

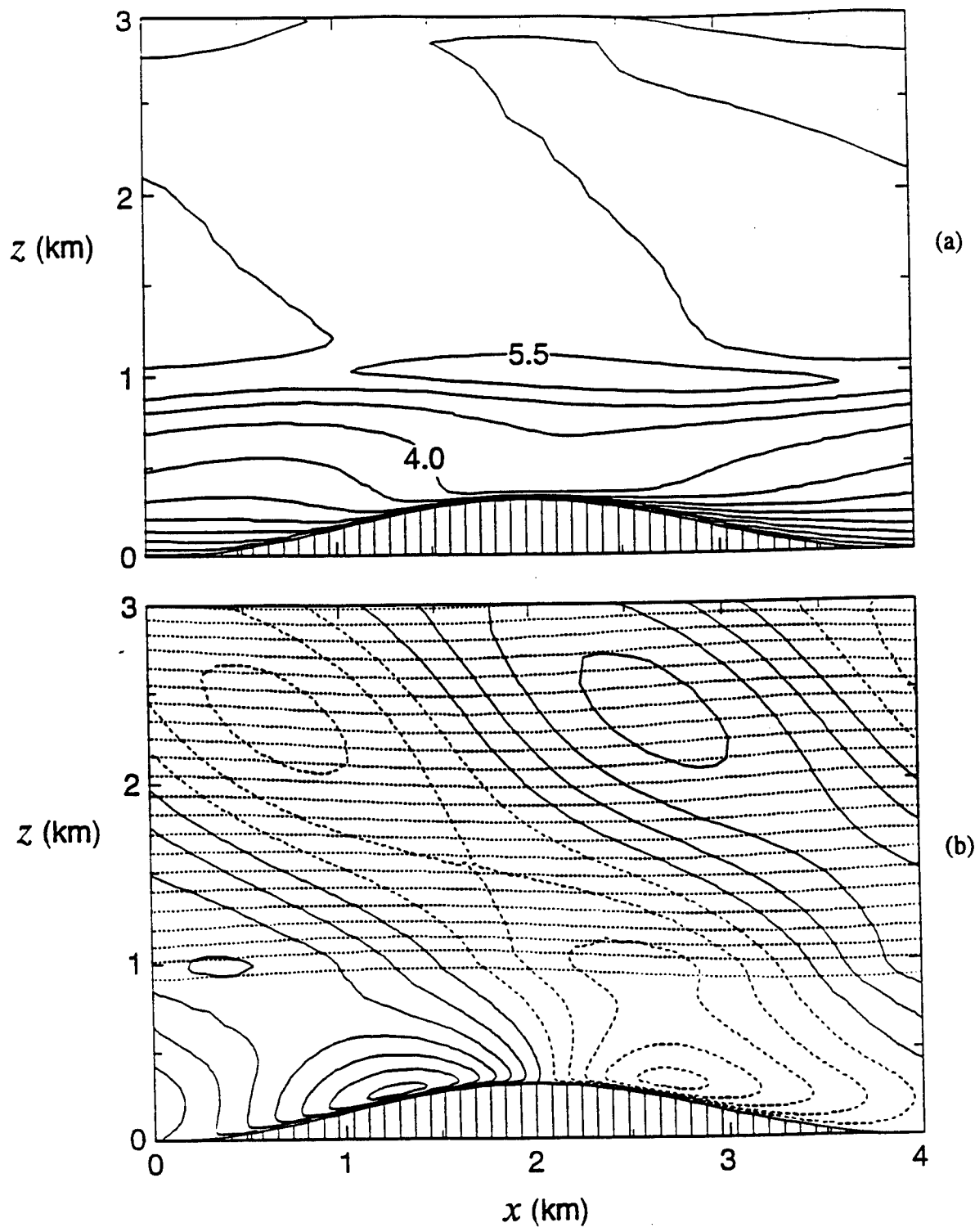


Figure 5-15. Mean flow over 4km ridges with slope 0.5 and  $z_0=1\text{m}$  and surface heat flux,  $H_0=0.0045^\circ\text{Cms}^{-1}$ . (a) mean  $x$ -component of velocity, contour interval of  $0.5\text{ms}^{-1}$ . (b) mean vertical velocity component, contour interval of  $0.1\text{ms}^{-1}$ , and potential temperature field, contour interval of  $0.5^\circ\text{K}$  (shown as dotted lines).

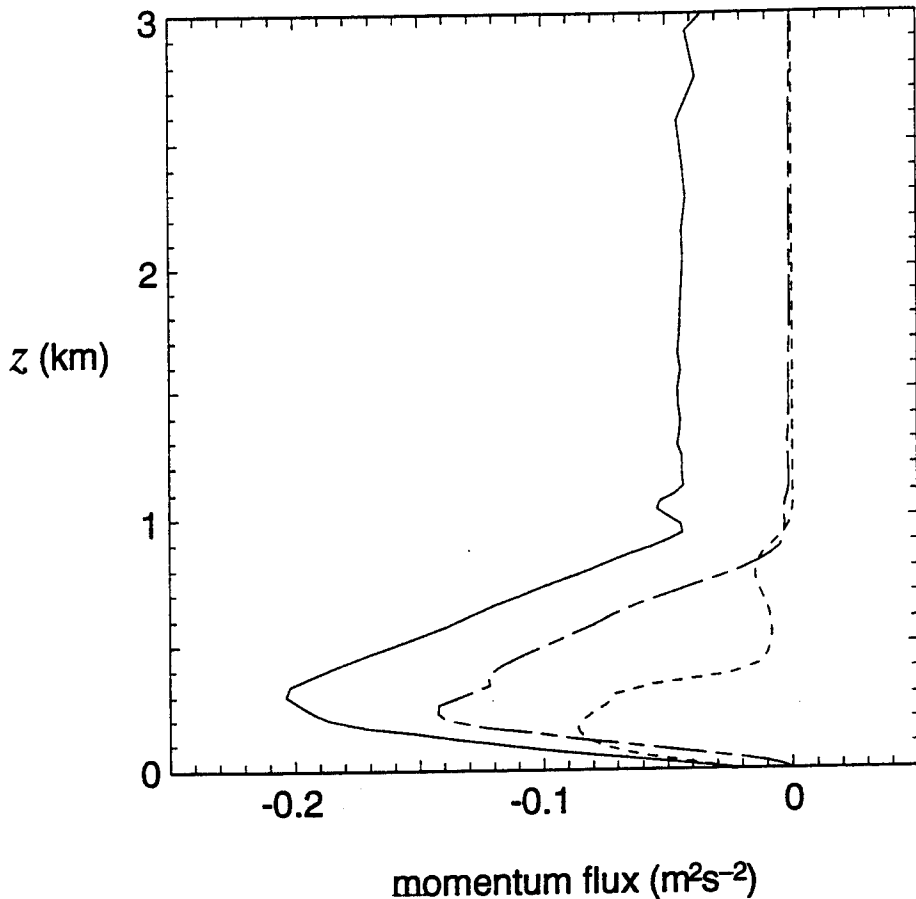


Figure 5-16. Vertical profiles of horizontally-average momentum flux for the 4km ridge with slope 0.25 and low surface heat flux. Short dashes represent the subgrid component, long dash-short dash represents the contribution from resolved scale fluctuations. Solid line is the total flux, including the contribution from the steady mean flow.

higher heat flux calculations,  $H_0=0.03^{\circ}\text{Cms}^{-1}$ , showed much smaller wave amplitudes for both slope values. The wave stresses were  $0.02\text{m}^2\text{s}^{-2}$  and  $0.01\text{m}^2\text{s}^{-2}$  for the  $s=0.25$  and  $s=0.5$  cases respectively. The ability of the convective boundary layer to absorb the terrain streamline deflections and prevent disturbance of the inversion is clearly an important factor determining the stable layer response.

Results for a more unstable boundary layer were obtained with  $u_g=2\text{ms}^{-1}$ ,  $z_0=1\text{m}$ , and  $H_0=0.03^{\circ}\text{Cms}^{-1}$ . Surface forces for a slope of 0.5 are shown in Figure 5-17 as a function of terrain wavelength; the forces are normalized by the flat surface stress value of  $0.061\text{m}^2\text{s}^{-2}$ . The effective drag coefficient for the flat surface is significantly

increased by the instability, but there is also an increase in the normalized pressure force relative to the  $u_g=5\text{ms}^{-1}$  cases at the two longer wavelengths (see Figure 5-10). There is evidence of the increased importance of buoyancy in the  $\lambda = 4\text{km}$  flows, as can be seen in the mean streamlines in Figure 5-18. The separation region is clearly enhanced by the buoyant instability, accelerating the reversed flow up the lee slope of the ridge and building an extensive recirculation region over the valley. These changes in effective boundary layer stability are enhanced by the reduction in  $u_B$  due to the surface drag, and are therefore more important for the longer wavelengths.

#### 5.4.4 Variation With Flow Direction.

The previous sections have all dealt with a geostrophic wind normal to the ridge axis. There is some interaction between the two horizontal velocity components through the Coriolis effects, so we examine the role of the geostrophic wind direction in this section. Four wind directions were calculated for  $\lambda = 2\text{km}$ ,  $u_g=5\text{ms}^{-1}$ ,  $z_0=1\text{m}$ ,  $H_0=0.03^\circ\text{Cms}^{-1}$ , and a slope of 0.5. A direction of  $0^\circ$  is the standard geostrophic flow

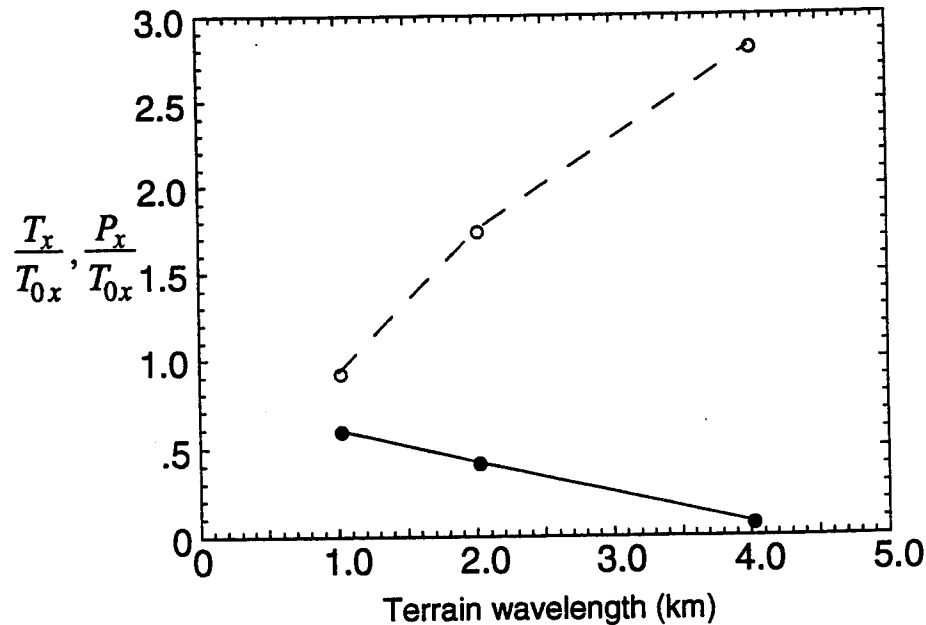


Figure 5-17. Normalized surface force variation with terrain wavelength for flow over ridges with slope 0.5 and  $z_0=1\text{m}$ , at low geostrophic wind speed of  $2\text{ms}^{-1}$ .

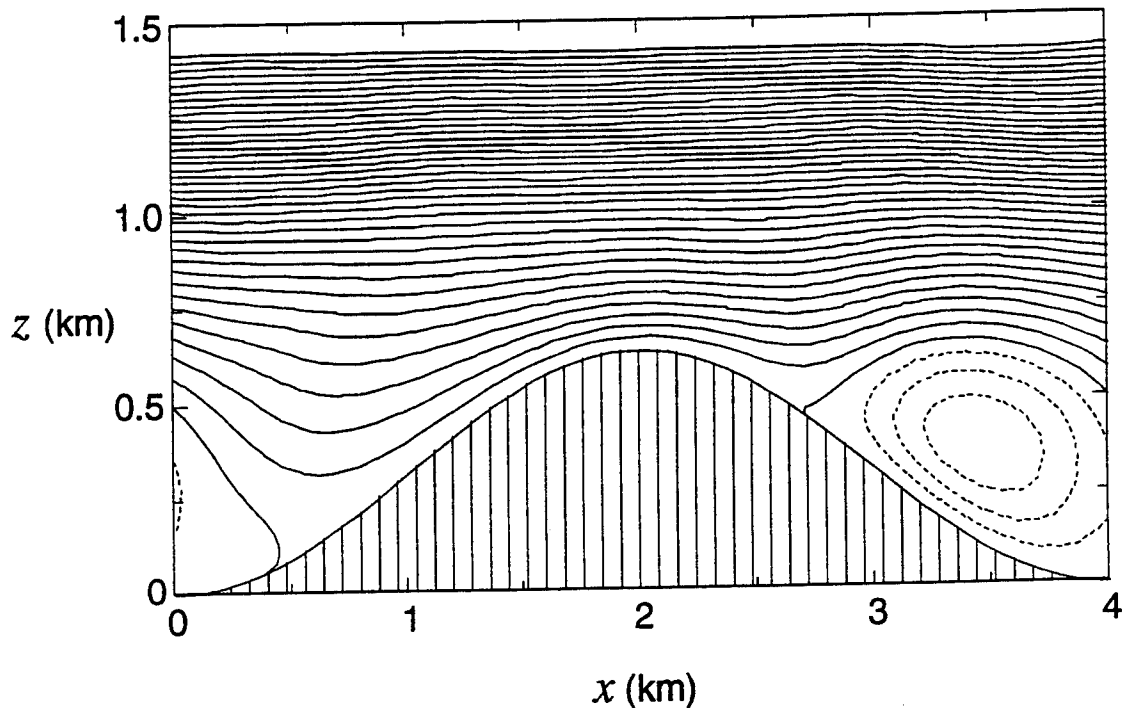


Figure 5-18. Mean streamlines for flow over a 4km ridge with slope 0.5 and  $z_0=1\text{m}$  at low geostrophic wind speed of  $2\text{ms}^{-1}$ . Contour interval is  $100\text{m}^2\text{s}^{-1}$ .

normal to the ridges,  $\pm 45^\circ$  implies a geostrophic flow of  $(3.5\text{ms}^{-1}, \pm 3.5\text{ms}^{-1})$ , while  $90^\circ$  represents a flow of  $(0, 5\text{ms}^{-1})$ .

The variation of the forces with direction is shown in Figure 5-19(a). The force variation seems complicated when viewed as a function of geostrophic direction, but shows some correspondence to the mean boundary layer velocity  $(u_B, v_B)$ , which is displayed in Figure 5-19(b). The boundary layer velocity basically responds to the rotation of the geostrophic wind, but shows a phase lag corresponding to the drag-induced deflection. Although the general behavior is as anticipated, with an approximate  $45^\circ$  turning of the wind in the boundary layer and a corresponding response in the surface forces, the quantitative details are not predictable by a simple rotation. First, there is a clear anisotropy in direction with  $x$ -forces behaving differently from  $y$ -forces since there are no terrain slopes in the  $y$ -direction. Also, the relation between the pressure force,  $P_x$ , and the  $x$ -component of velocity,  $u_B$ , is not straightforward. The four directions chosen for this study produce two pairs of  $u_B$  values. For similar values of  $u_B$ , the pressure force is similar, even though  $v_B$  is significantly different. However, the lower value of  $u_B$  produces a larger pressure force than expected from a quadratic law. It is likely that this

behavior is due to the enhanced instability at low values of  $u_B$  as seen in the previous section, which apparently transfers momentum more efficiently.

Mean velocity fields for the two cases with geostrophic wind at an angle of  $\pm 45^\circ$  relative to the ridge, that is, geostrophic winds of ( $3.5\text{ms}^{-1}$ ,  $\pm 3.5\text{ms}^{-1}$ ), are shown in Figure 5-20. These flows are quite different, with  $u_B$  being very small in the first and  $v_B$  small in the second. However, it is interesting that both cases show that there is significant wind shear in the component with the small layer-averaged value. The major component exhibits a well-mixed region above the hill crests, but there is roughly  $2\text{ms}^{-1}$  shear across the boundary layer depth transverse to the mean flow.

The pressure force for the low- $u_B$  values, that is, geostrophic wind directions of  $90^\circ$  and  $45^\circ$ , is much larger than would be expected by scaling the  $0^\circ$  result by the square of  $u_B$ . However, the value is very similar to that obtained with  $u_g=2\text{ms}^{-1}$  and a similar value for  $u_B$ . The pressure forces scale reasonably well with the value of the boundary layer velocity if we use the stability-dependent stress values based on  $u_B$ , as determined from the previous section. Apparently, the pressure force depends on the effective stability of the flow as determined by the actual mean boundary layer velocity normal to the ridges and is largely independent of the flow parallel to the crests. The force parameterizations are discussed in the next section.

## 5.5 SURFACE FORCE PARAMETERIZATION.

The extensive parameter studies described in the previous section can be used as a basis for a general surface drag parameterization scheme for convective flow over ridges. The objective of such a scheme is the representation of the average surface forces in terms of large scale parameters, such as the wind speed, surface heat flux, terrain geometry, etc. We postulate a functional dependence for the forces, and use the LES results to provide quantitative input for the parameterizations.

### 5.5.1 Pressure Force.

We first consider the pressure force, since this is the major contributor to the force variability. The general expectation is that the pressure force will vary in proportion to the square of the terrain slope and also like the square of some appropriate flow speed.

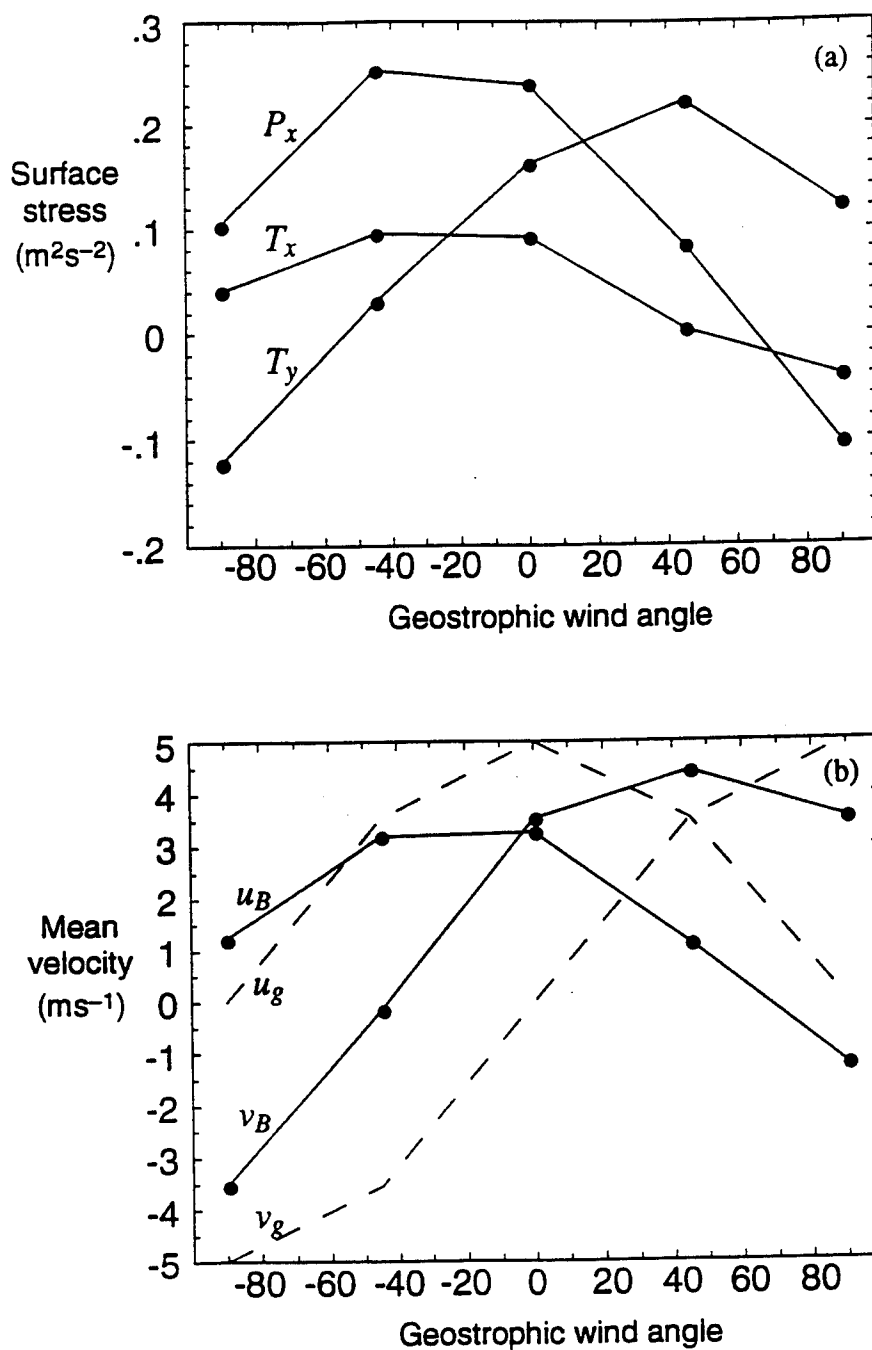


Figure 5-19. Variation of surface forces and mean boundary layer velocity with geostrophic wind direction for 2km ridges and  $z_0=1m$ . (a) average pressure force ( $P_x$ ), and tangential stress forces ( $T_x$ ,  $T_y$ ) per unit area. (b) mean boundary layer velocity components ( $u_B$ ,  $v_B$ ).

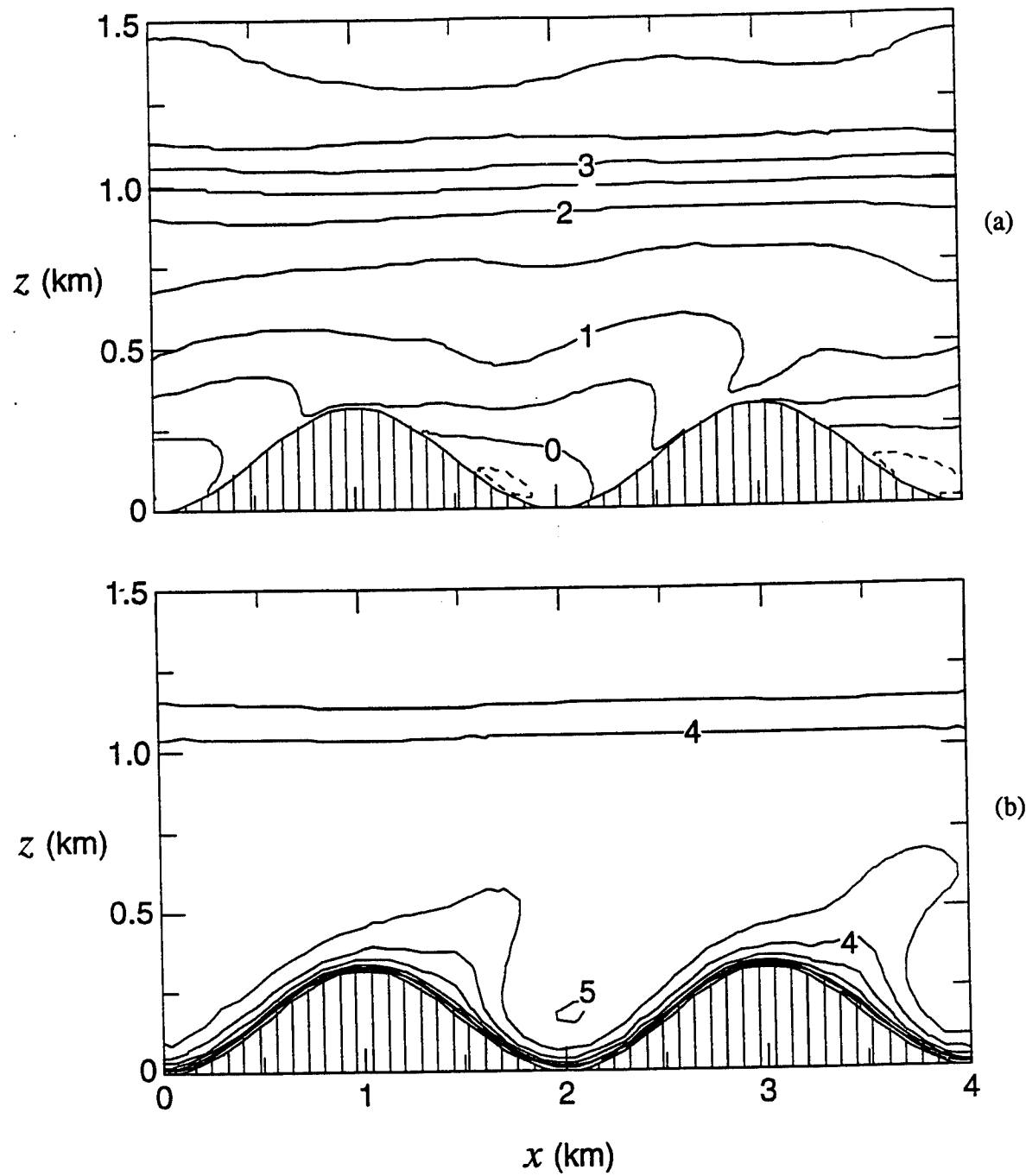


Figure 5-20. Mean horizontal velocity components flow over 2km ridges with slope 0.5 and  $z_0=1\text{m}$ . (a)  $\bar{u}$  and (b)  $\bar{v}$  for geostrophic flow at  $+45^\circ$ . (c)  $\bar{u}$  and (d)  $\bar{v}$  for geostrophic flow at  $-45^\circ$ . Contour interval is  $0.5\text{ms}^{-1}$ .

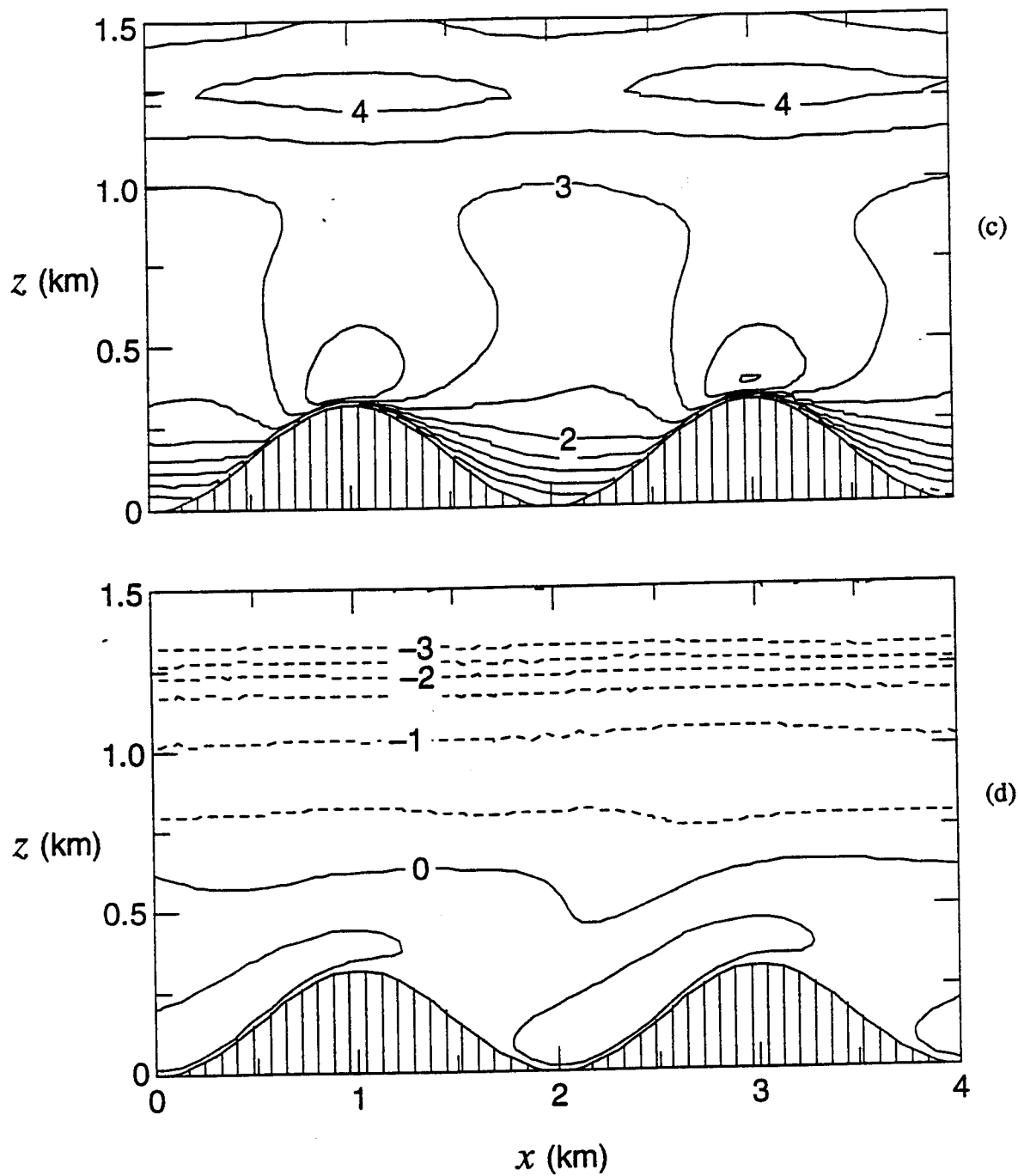


Figure 5-20 Mean horizontal velocity components flow over 2km ridges with slope 0.5 and  $z_0=1\text{m}$ . (a)  $\bar{u}$  and (b)  $\bar{v}$  for geostrophic flow at  $+45^\circ$ . (c)  $\bar{u}$  and (d)  $\bar{v}$  for geostrophic flow at  $-45^\circ$ . Contour interval is  $0.5\text{ms}^{-1}$  (Continued).

The slope dependence is anticipated from linearized analyses and is also supported by the results of section 5.4.1. We suggest that the bulk average boundary layer velocity,  $u_B$ , is a plausible velocity scale, since this represents the mean boundary layer flow normal to the ridge. The first approximation for  $P_x$  can therefore be written as

$$P_x = C_1 s^2 u_B^2 \quad (5.30)$$

where  $s$  is the maximum slope, and  $C_1$  is a dimensionless coefficient. We do not expect  $C_1$  to be a constant; it must describe effects other than flow speed and terrain slope. The functional dependence of  $C_1$  on other flow parameters must now be determined.

The surface roughness dependence shown in Section 5.4.2 indicated that the pressure force was closely proportional to the equivalent flat surface stress, if all other parameters remained fixed. Since we wish to use the effective boundary layer speed,  $u_B$ , as the velocity scale, we need to define a flat surface drag coefficient,  $c_{D0}$ , such that

$$(T_x^2 + T_y^2)^{1/2} = c_{D0} (u_B^2 + v_B^2) \quad (5.31)$$

for the flat surface. Here,  $(u_B, v_B)$  is the steady-state average boundary layer velocity for the flat surface, and the force dependence is chosen to be consistent with horizontal isotropy. We have not used the  $x$ -component of the stress in this definition of  $c_{D0}$ , so we are not entirely consistent with the force normalization employed in the previous section. However, the additional complication involved in defining generalized drag coefficients for the different direction components does not seem warranted at this stage. From (5.31),  $c_{D0}$  will be a function of  $z_0$ , geostrophic wind speed,  $U_g$ , and the boundary layer stability, measured by  $w_*$ . Values for  $c_{D0}$  determined from the LES calculations are shown in Figure 5-21 as a function of the stability parameter,

$$S_B = \frac{w_*}{(u_B^2 + v_B^2)^{1/2}}$$

Our representation of the pressure force now becomes

$$P_x = C_2 c_{D0} s^2 u_B^2 \quad (5.32)$$

where the undetermined coefficient,  $C_2$ , accounts for other flow effects.

The different terrain wavelengths in Section 5.4.1 produced different pressure force results, so this must be accounted for in  $C_2$ . It was suggested that the 'constriction' effect induced by the stable inversion layer could be responsible for the increased forces

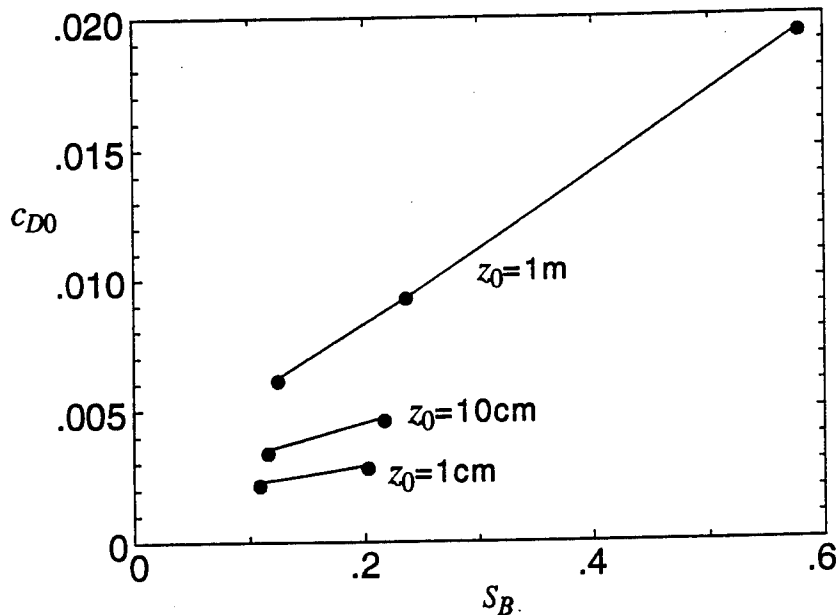


Figure 5-21. Bulk mean drag coefficient,  $c_{D0}$ , for flow over flat terrain as determined from the LES calculations. Variation is shown for different roughness lengths as a function of boundary layer stability,  $S_B$ .

on the longer wavelength ridges. Conservation of mass implies that the speed over the ridges crest must increase if the layer depth is diminished, and we observed a relatively horizontal inversion in the LES results. If we use this accelerated speed as the scaling velocity, then  $C_2$  contains a factor inversely proportional to the square of the depth of the boundary layer over the crest, i.e.,

$$P_x = \frac{C_3 c_{D0} s^2 u_B^2}{(1 - h_{\max}/z_i)^2} \quad (5.33)$$

where  $h_{\max}$  and  $z_i$  are defined relative to the average terrain elevation.

The relation (5.33), with  $C_3 = 5$ , provides a reasonably good description of the pressure forces for most of the calculated cases, as can be seen in Figure 5-22. The poorly predicted forces are associated with the light wind cases for the strongly unstable boundary layer, and for two of the wind direction values from Section 5.4.4. Variations with slope, wavelength, and surface roughness are well predicted for the moderately unstable layer,  $w_*/U_g = 0.2$ , and also for the lower heat flux cases, where  $w_*/U_g = 0.1$ .

It was postulated that the anomalously large pressure forces shown in Figure 5-22 were due to the effects of buoyant instability at low wind speed. It was suggested in the

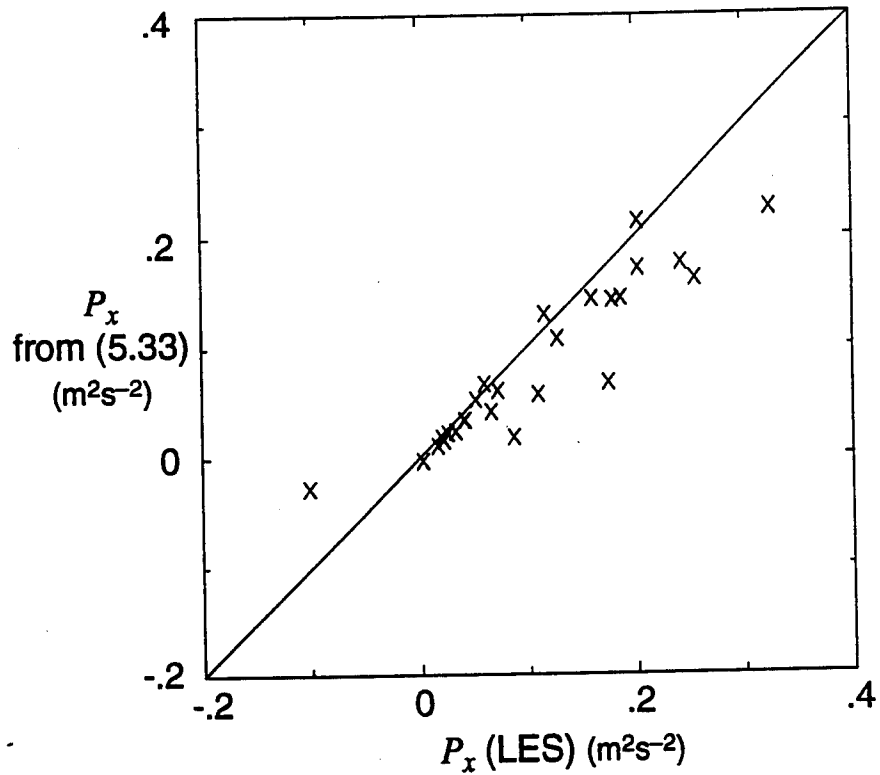


Figure 5-22. Comparison between LES results for  $P_x$  and the estimate from (5.33).

previous section that the stability dependence of the pressure force seemed to be determined by the component of velocity normal to the ridge. The final form for the pressure force is therefore

$$P_x = C_3 c_{D0} \left( \frac{z_0}{z_i}, \frac{w_*}{|u_B|} \right) \frac{s^2 u_B |u_B|}{(1 - h_{\max}/z_i)^2} \quad (5.34)$$

where the sign of the boundary layer wind is now accounted for.

The functional dependence of  $c_{D0}$  was only crudely determined from the LES results shown in Figure 5-21, and simple linear interpolation/extrapolation was used in the application of (5.34). The final comparison between the pressure force predicted by (5.34) and the calculated LES values is shown in Figure 5-23. There is now reasonably good agreement throughout the range of conditions of the simulations, with only one case showing an error of more than about 20%. This is the largest hill at the smallest heat flux, and (5.34) overpredicts the pressure force by 50%.

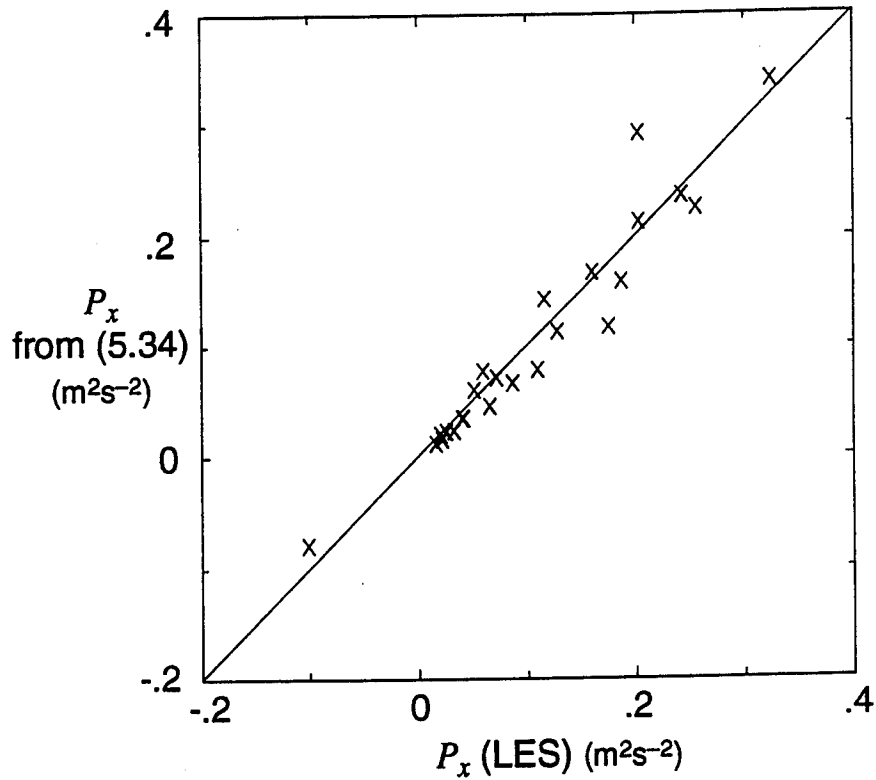


Figure 5-23. Comparison between LES results for  $P_x$  and the estimate from (5.34).

### 5.5.2 Tangential Stress Forces.

The processes controlling the tangential turbulent stresses are governed by the local velocity field near the surface. The major features evident in the force variations are a decrease in  $T_x$  due to the flow separation between the ridges, and an increase in  $T_y$  due to the enhancement in the transverse velocity component. An obvious approach to the parameterization of these forces is therefore to assume the same dependence as the flat surface case, i.e.,

$$T_x = c_{D0} u_B \left( u_B^2 + v_B^2 \right)^{1/2} \quad (5.35a)$$

$$T_y = c_{D0} v_B \left( u_B^2 + v_B^2 \right)^{1/2} \quad (5.35b)$$

and we only need to determine the appropriate drag coefficient,  $c_{D0}$ . Estimates made using the same value as in the pressure force (5.34) are compared with the LES results in Figure 5-24. There is a clear overprediction of the tangential forces for both components, and it is clear that these components do not show the stability effects observed in the

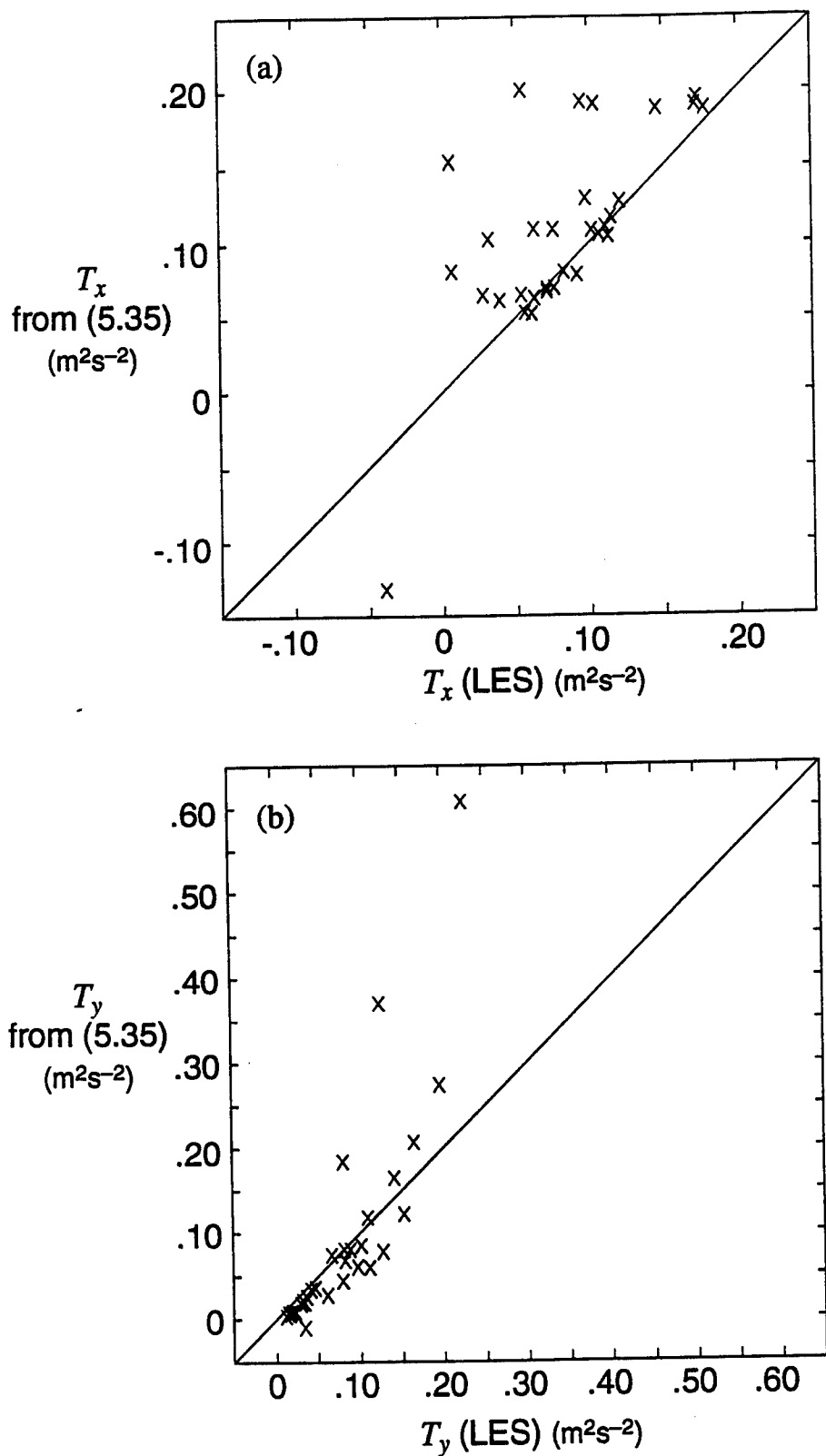


Figure 5-24. Comparison between LES results for (a)  $T_x$  and (b)  $T_y$  and the estimate from (5.35) with the stability dependent coefficient as in (5.34).

pressure force variations. Revised estimates were made using the stability parameter  $S_B$ , based on the mean speed,  $(u_B^2 + v_B^2)^{1/2}$ , rather than the  $u_B$ -component, and the results are shown in Figure 5-25. This also contains a reduction factor on  $T_x$  to account for the separation effects, so that the final form for the tangential stress is

$$T_x = c_{D0} \left( \frac{z_0}{z_i}, S_B \right) u_B (u_B^2 + v_B^2)^{1/2} (1 - h_{\max}/z_i)^2 \quad (5.36a)$$

$$T_y = c_{D0} \left( \frac{z_0}{z_i}, S_B \right) v_B (u_B^2 + v_B^2)^{1/2} \quad (5.36b)$$

This formulation provides a reasonably good approximation for the range of the LES results.

### 5.5.3 Extension to Complex Terrain.

The results of the previous section were confined to sinusoidal ridges, but the wide range of parameters allowed a general basis for the force parameterization. In order to further broaden the basis, several calculations were made for different terrain geometry. First, variations on the sinusoidal shape assumption were investigated by extending the width of the valley region in comparison with the ridge itself. The terrain is still two-dimensional, so the basic parameterization can remain as described by (5.34). The three cases are illustrated in Figure 5-26, showing increasingly isolated ridges but maintaining the same r.m.s. terrain slope. The ridges become higher as the separation increases, and the flow perturbation becomes larger but is localized around the ridge. The force results for the three cases are given in Table 5-1.

The second series of cases are three-dimensional hills, i.e., with variation in the  $y$ -direction. A modulation of the ridge terrain was tried, with elevation defined by the relation

$$h(x, y) = \frac{h_0}{2} \left( 1 - \cos \frac{2\pi x}{\lambda_x} \right) \left[ \alpha + \frac{(1-\alpha)}{2} \left( 1 + \cos \frac{2\pi y}{\lambda_y} \right) \right] \quad (5.37)$$

Thus,  $h = \alpha h_{2D} + (1 - \alpha) h_{3D}$ , where  $h_{2D}$  is the ridge topography (5.24),

$$h_{3D} = \frac{h_0}{4} \left( 1 - \cos \frac{2\pi x}{\lambda_x} \right) \left( 1 + \cos \frac{2\pi y}{\lambda_y} \right)$$

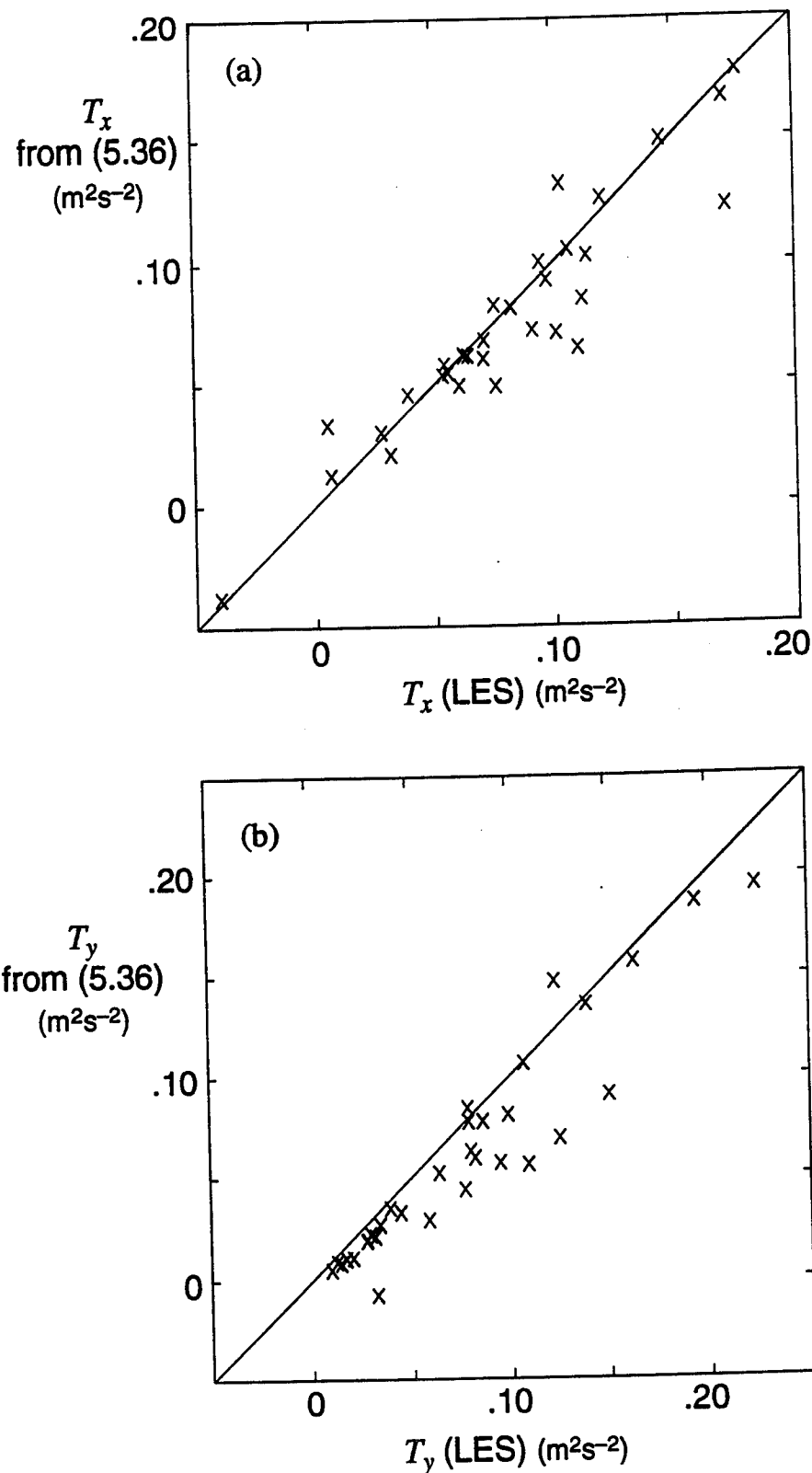


Figure 5-25. Comparison between LES results for (a)  $T_x$  and (b)  $T_y$  and the estimate from (5.36) with the stability dependent coefficient based on  $(u_B^2 + v_B^2)^{1/2}$ .

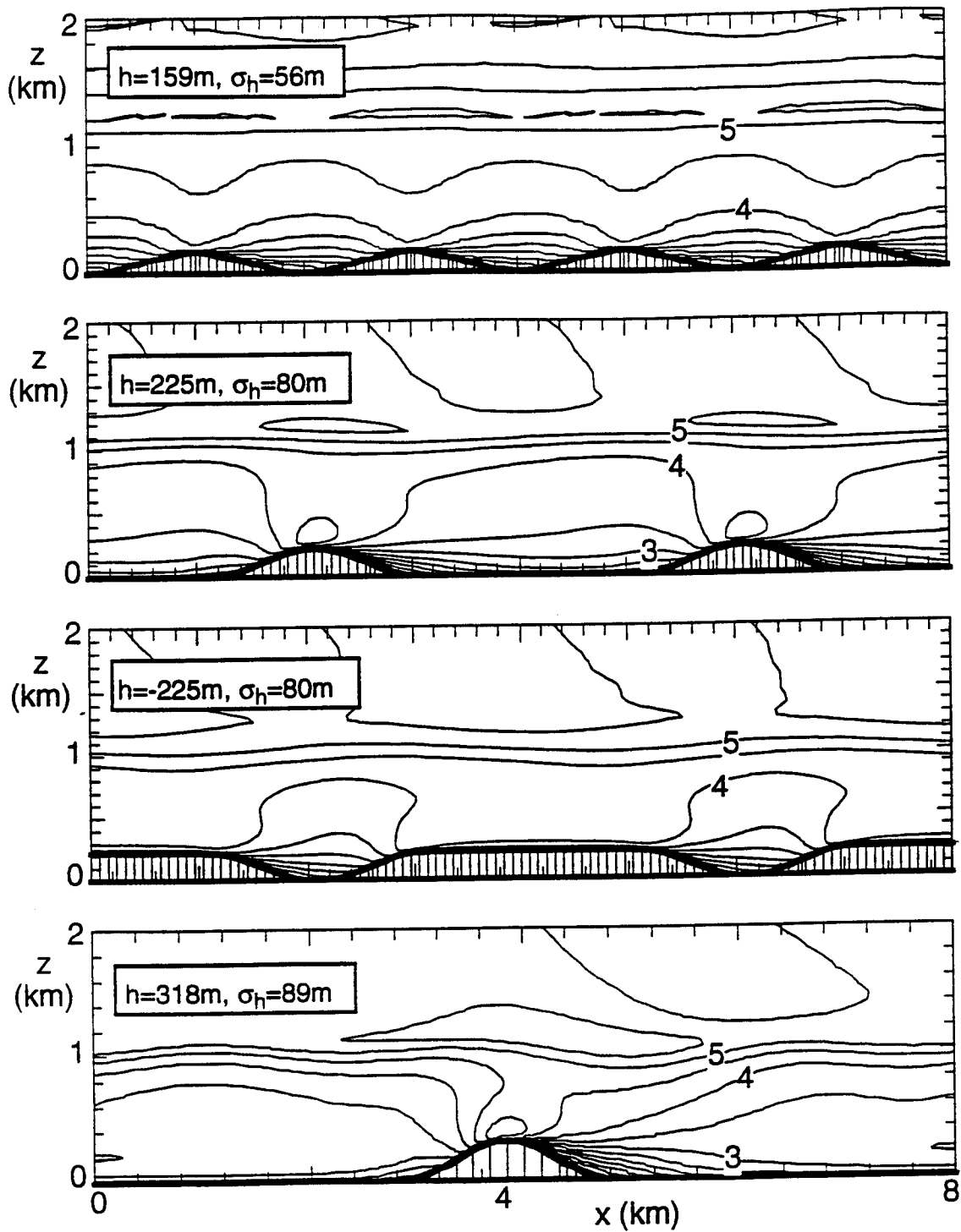


Figure 5-26. Mean  $u$ -velocity for convective flow over four ridge shapes. Standard sinusoidal ridge is shown at top, and velocity contours are in  $\text{ms}^{-1}$ . Geostrophic wind is  $5\text{ms}^{-1}$ , the surface roughness is  $1\text{m}$ .

**Table 5-1. Forces for complex terrain shapes.**

Terrain	$h_0$ (m)	Max. slope	$P_x$ ( $\text{m}^2\text{s}^{-2}$ )	$P_y$ ( $\text{m}^2\text{s}^{-2}$ )	$T_x$ ( $\text{m}^2\text{s}^{-2}$ )	$T_y$ ( $\text{m}^2\text{s}^{-2}$ )
3D-isolated	318	0.50	0.025	0.010	0.158	0.087
$\lambda_x=\lambda_y=2\text{km}$ $\alpha=1$	318	0.50	0.068	0.036	0.125	0.094
$\lambda_x=\lambda_y=2\text{km}$ $\alpha=1$	159	0.25	0.018	0.008	0.164	0.085
$\lambda_x=\lambda_y=2\text{km}$ $\alpha=0.5$	318	0.50	0.121	0.010	0.1114	0.130
$\lambda_x=\lambda_y=2\text{km}$ $\alpha=0.5$	159	0.25	0.033	0.002	0.170	0.092
$\lambda_x=2\text{km}$ $\alpha=0$	318	0.50	0.240	0.0	0.093	0.162
$\lambda_x=2\text{km}, \alpha=0$ (Fig. 5-26a)	159	0.25	0.049	0.0	0.144	0.098
Fig. (5-26b)	225	0.35	0.057	0.0	0.138	0.109
Fig. (5-26c)	225	0.35	0.045	0.0	0.148	0.099
Fig. (5-26d)	318	0.50	0.094	0.0	0.148	0.113

and  $\alpha$  is an interpolation parameter between the two shapes. Simulations were made for the parameters given in Table 5-1, with values of  $\alpha$  of 0, 0.5, and 1; all cases used a surface roughness height of 1m and surface heat flux of  $0.03^\circ\text{Kms}^{-1}$ . The table also includes an isolated circular hill, which has cosine shape with a radius of 1km in the 4km square domain. Force results from the calculations are given in the table.

The force parameterization given in (5.34) is clearly a specialization, since the only component of the pressure force is in the  $x$ -direction for ridge terrain. We require a

general directional dependence to account for three-dimensional terrain, but the form must collapse to (5.34) for two-dimensional ridges. The generalization of the r.m.s. slope must come from the second-rank tensor,  $s_{ij}$ , defined as

$$s_{ij} = \overline{\frac{\partial h}{\partial x_i} \frac{\partial h}{\partial x_j}}$$

The force parameterization can then be written as

$$P_i = 10 c_{D0} \left( \frac{z_0}{z_i}, \frac{w_*}{u_S} \right) \frac{s_{ij} u_{Bj} u_S}{\left( 1 - \sqrt{2} \sigma_h / z_i \right)^2} \quad (5.38a)$$

$$T_i = c_{D0} \left( \frac{z_0}{z_i}, \frac{w_*}{U_B} \right) U_B \left( u_{Bi} - C_T s_{ij} u_{Bj} \right) \quad (5.38b)$$

where

$$\begin{aligned} U_B &= |u_{Bi}| \\ U_S &= \frac{|s_{ij} u_{Bj}|}{\lambda(s)} \\ C_T &= \frac{1 - (1 - \sqrt{2} \sigma_h / z_i)^2}{\lambda(s)} \end{aligned}$$

and  $\lambda(s)$  is the maximum eigenvalue of  $s_{ij}$ . This somewhat obscure normalization is required to ensure that the force is proportional to the modulus of the boundary layer velocity for horizontally isotropic terrain. The comparison between the prediction of the pressure force from (5.38) and the complex terrain force results from this section is shown in Figure 5-27. The results are encouraging, and suggest that the given form may be reasonably accurate for a wide range of conditions.

## 5.6 TURBULENCE AND DIFFUSION.

The presence of terrain clearly modifies the mean velocity field, as shown in the previous section, and this will induce changes in the turbulence fields. The turbulence is distorted by the additional shears and responds in a complicated way. Shear generally produces turbulent kinetic energy, but the transient shears experienced in flow over terrain do not always persist long enough for equilibrium relationships to become

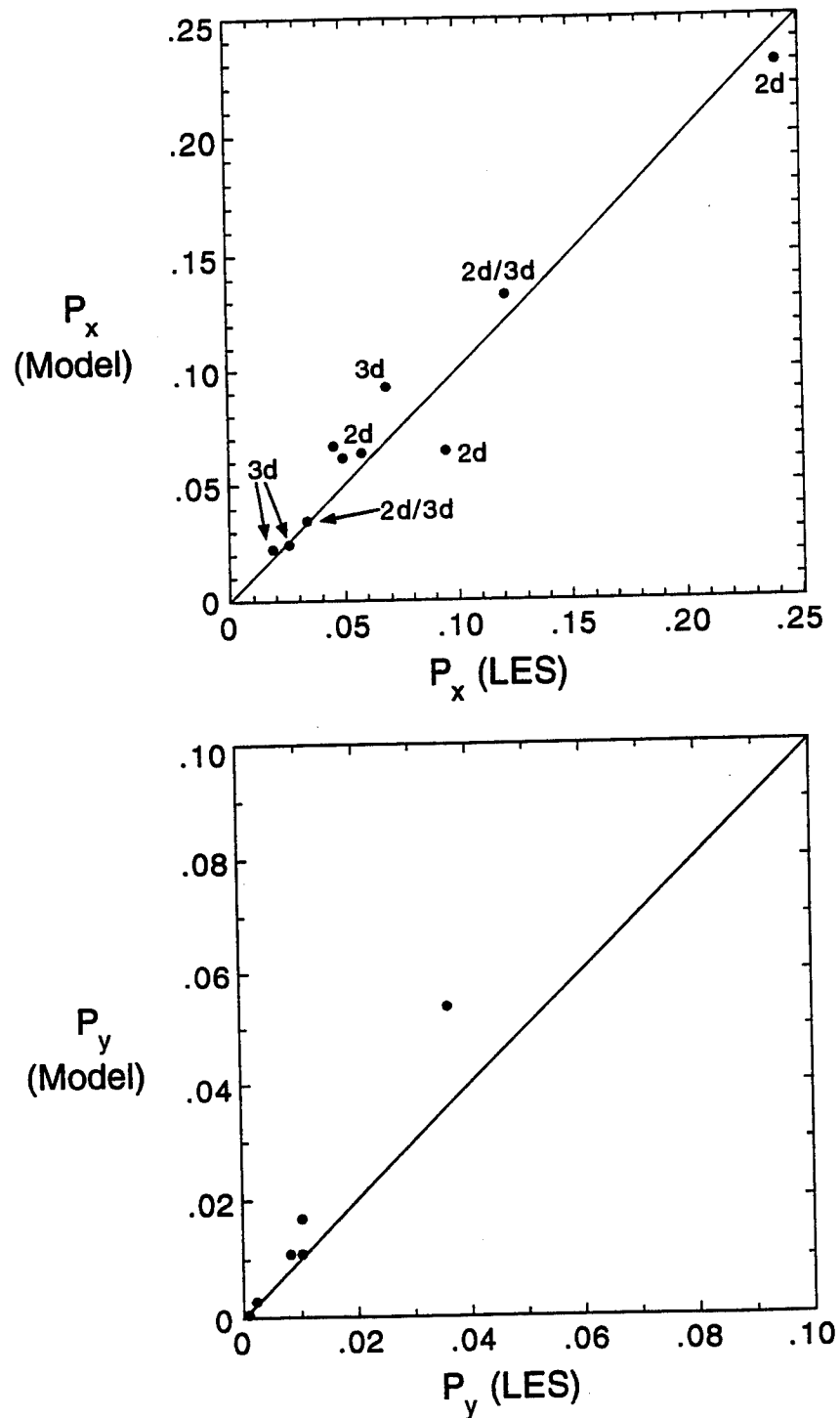


Figure 5-27. Comparison between LES pressure forces and the prediction from (5.38) for the range of terrain shapes described in Table 5-1 and the 2d-ridges in Figure 5-26.

established. The dispersion of dust particles in the boundary layer will be affected by both the mean flow and turbulence changes, but we first examine the turbulence fields from the LES calculations. We consider the sinusoidal ridge terrain first.

### 5.6.1 Velocity Variances.

One of the complicating features of turbulent flow over the terrain is the effect of shear distortion on the turbulent eddies. The stretching and tilting of the eddies as they pass over the terrain is a non-equilibrium process if the timescales of the distortion are faster than the eddy turnover timescales. This is one of the reasons for using LES to model the flow, since empirical assumptions about the Reynolds stress distributions are unreliable under these conditions. We do, however, use an equilibrium assumption for the subgrid stress model, which assumes that the timescale of the subgrid eddies is fast enough that they remain in balance with the local wind shear. The subgrid turbulence scale,  $\Lambda_{\max}$ , is generally 45m for the calculations reported here, so that the subgrid turbulence time scale,  $\Lambda/q$ , is roughly 45s for a typical r.m.s. subgrid turbulence velocity,  $q$ , of  $1\text{ms}^{-1}$ . The energy dissipation time scale is longer by a factor of  $(2b)^{-1}$ , which is 4 for the constants used in the turbulence model (Lewellen, 1977). The transit time for flow over the ridges depends on the wavelength and mean boundary layer velocity, but most of the results are for a 2km wavelength and a geostrophic wind of  $5\text{ms}^{-1}$ . The average boundary layer speed is somewhat less than the geostrophic speed, so a typical transit time for passage over the ridge is about 500s, compared with the dissipation time of about 200s. The subgrid turbulence consequently responds on time scales faster than the distortion time, but not significantly faster. The subgrid perturbations may not be completely reliable, therefore, except in the region very close to the surface where the scale is limited by distance from the ground and response time scales are correspondingly faster. The subgrid component is a relatively small fraction of the total turbulence energy, however, so inaccuracies in this component do not significantly affect the overall results.

The general behavior of all three components of the velocity variance for two different terrain slopes is presented in Figure 5-28. Velocity statistics were obtained from a transverse average across the integration domain and a 3000s time average; this period was determined to be sufficiently long to provide reliable statistics. For a maximum terrain slope of 0.25, the variance perturbations are relatively small, and the ambient vertical profile is clearly visible. The disturbance near the surface is of significant

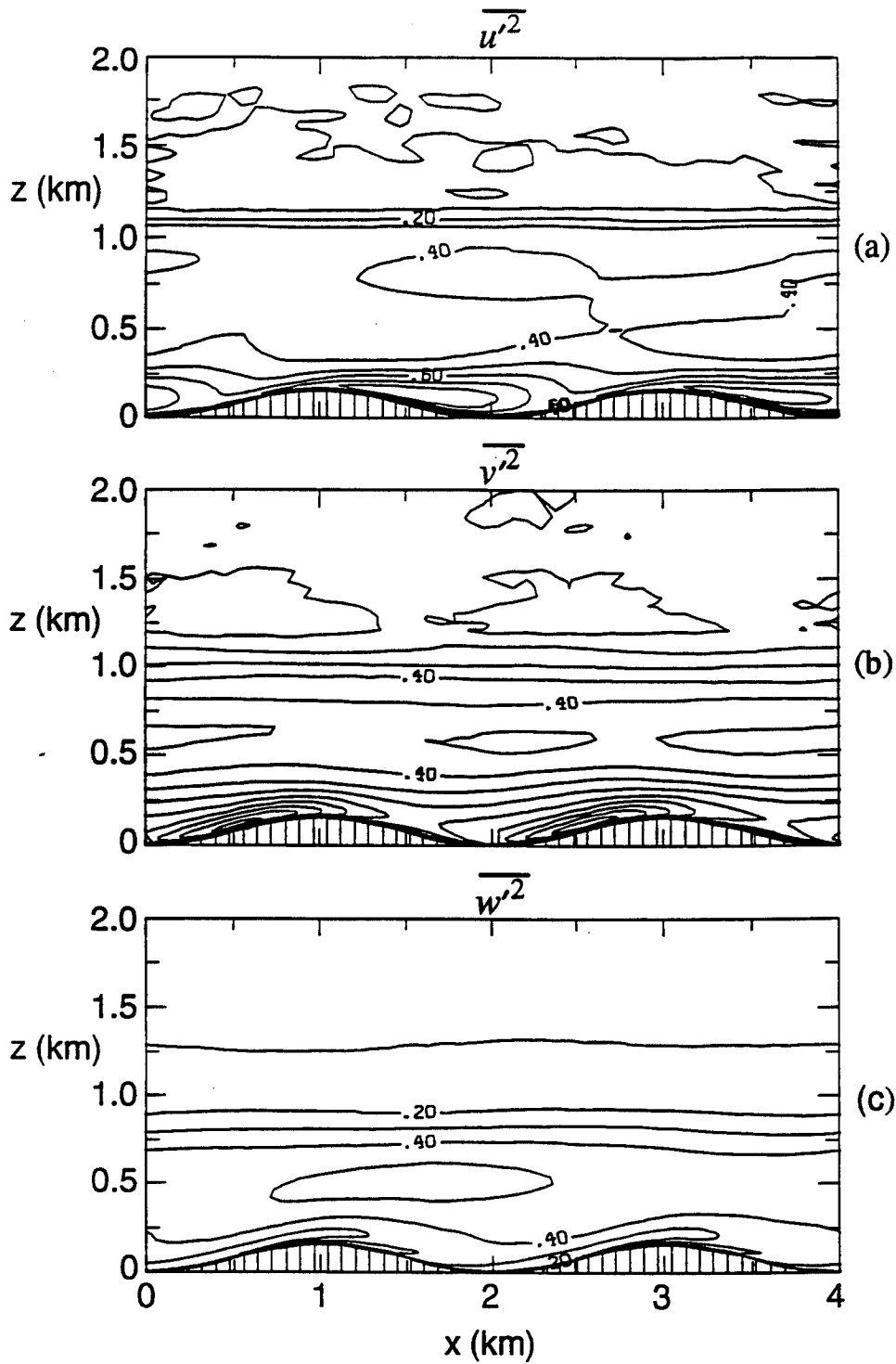


Figure 5-28. Total velocity variances (resolved + subgrid). Contour increments are  $0.1 \text{ m}^2 \text{s}^{-2}$ . Max. slope=0.25: (a) streamwise, (b) transverse, (c) vertical. Max. slope=0.5: (d) streamwise, (e) transverse, (f) vertical.

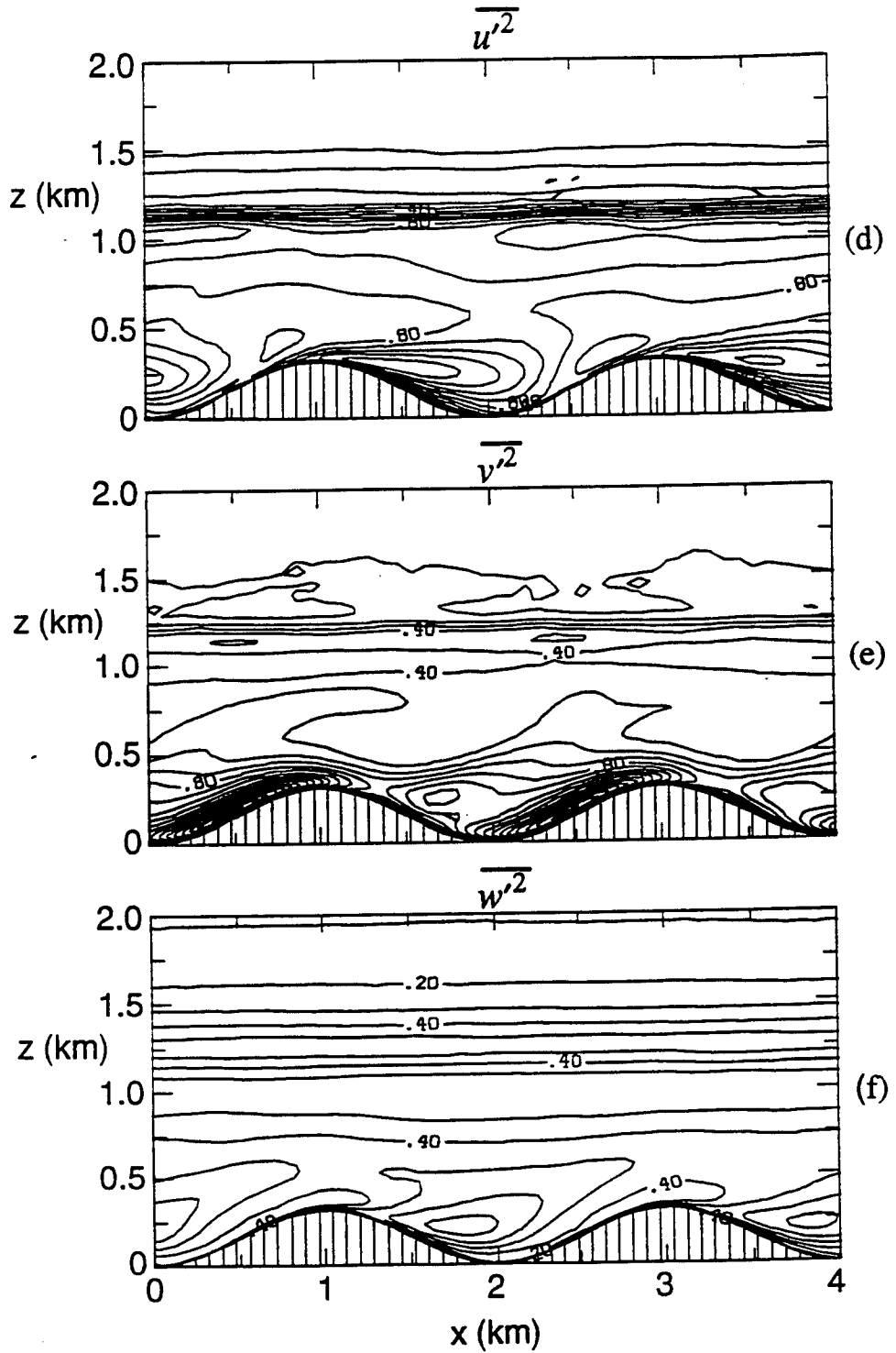


Figure 5-28. Total velocity variances (resolved + subgrid). Contour increments are  $0.1 \text{ m}^2 \text{s}^{-2}$ . Max. slope=0.25: (a) streamwise, (b) transverse, (c) vertical. Max. slope=0.5: (d) streamwise, (e) transverse, (f) vertical (Continued).

amplitude but is confined to a layer of about 200m depth. The amplitude of the disturbance and also the vertical extent is increased in the higher slope case. The streamwise component,  $\overline{u'^2}$ , shows a strong increase downstream of the hill crest and above the surface. This is a region of high vertical shear, as the surface flow is reduced in the lee and is associated with the separation bubble boundary for the slope of 0.5. The high values of  $\overline{u'^2}$  grow from a very shallow layer, originating just upstream of the crest in the region of high surface stress values, and spreading vertically downstream. There is evidence of a reduction in  $\overline{u'^2}$  at some height above the surface just upstream of the crest. This is seen as a lowering of the contours for small slope, and becomes a local minimum at a slope of 0.5. The vertical velocity variance,  $\overline{w'^2}$ , behaves differently, showing an increase above the surface upstream of the crest but smaller values in the shear layer region where  $\overline{u'^2}$  is maximum. The most dramatic variations are seen in  $\overline{v'^2}$ , however. There is an increase in  $\overline{v'^2}$  over the upslope of the ridge that becomes very large for the higher slopes. The local maximum in  $\overline{v'^2}$  for a slope of 0.5 is almost twice as large as the streamwise fluctuation variance in the separating shear layer.

The variance perturbations are qualitatively consistent with existing analyses of turbulence modification in flow over ridges. Britter et al. (1981), discussing the response of neutral layer turbulence, suggest that the variances close to the surface are governed by the tangential stress behavior, which maximizes over the crest. Further above the surface, the turbulence undergoes rapid distortion effects (Batchelor and Proudman, 1954), which reduces  $\overline{u'^2}$  over the crest but increases the two transverse components,  $\overline{v'^2}$  and  $\overline{w'^2}$ . Some of these features are visible in the convective layer results in Figure 5-28, but the existing rapid distortion analyses are not strictly applicable to the convective layer situation. The analysis has been carried out (Newley, 1985) for axisymmetric turbulence with  $\overline{v'^2} = \overline{w'^2}$ , but the convective layer has large values for both horizontal components near the surface and a small vertical velocity variance and therefore does not match the assumptions of the theory. The rapid distortion results for the transverse and vertical components are sensitive to the initial turbulence levels. The existing analyses also ignore the presence of the solid surface in their derivation of the velocity spectrum from the vorticity distortion. The more complete theory of Hunt (1973) would be required for the convective situation where the larger eddies are significantly affected by the wall. It is still instructive to examine the quantitative response of the velocity variances, however, so we now proceed to a closer examination of the variance profiles.

Vertical profiles of the three variance components for a slope of 0.125 are shown in Figure 5-29 in comparison with the flat surface results. The perturbations are relatively small, but several features are clear. First, the  $\overline{u'^2}$  intensity is generally increased throughout the layer, indicative of a nonlinear response due to the repeated interaction with the periodic ridges even at this small slope. Relative to the mean value,  $\overline{u'^2}$  is increased near the surface but is reduced from the flat surface value over the crest of the ridge. Above the valley,  $\overline{u'^2}$  is increased except for a reduction in the lowest 100m. The transverse component shows an increase in the lower half of the boundary layer both over the crest and the valley, while the vertical component shows a general reduction except for the lowest 100m. The  $\overline{w'^2}$  results must be viewed with caution near the surface, since the bulk of the variance is represented by the subgrid model using the 'quasi-equilibrium' assumption.

The trends observed in the small slope case are more obvious when the slope is increased to 0.5. Figure 5-30 shows the variance profiles from the large slope calculation and the general increase in all three components is immediately obvious. The horizontal variance components are roughly doubled in the main boundary layer, with significant perturbations in the lower altitudes.  $\overline{u'^2}$  shows its maximum amplitude in the shear layer that separates from the lee slope of the ridge, while  $\overline{v'^2}$  shows the dramatic increase in the lowest 200m, as noted in Figure 5-28. The variation in the depth of the boundary layer relative to the local surface elevation is clearly visible in the profiles, with a maximum difference of about 300m between crest and valley.

The profiles of  $\overline{w'^2}$  in Figure 5-30 also show an increase in the main boundary layer, with a local maximum associated with the separating shear layer. There is a close correspondence between  $\overline{w'^2}$  and  $\overline{u'^2}$  in the relative variation in the main boundary layer; both components show a minimum over the crest and a maximum over the valley. The average value of  $\overline{w'^2}$  is increased much less than the horizontal components, however. This is consistent with the general observations of increased horizontal variance in complex terrain, although the sinusoidal ridges demonstrate that the topography need not be complicated; a significant slope is all that is required to generate the large vertical gradients and induce high amplitude horizontal velocity fluctuations.

A more striking feature of the vertical velocity variance profiles is the strong maximum just above the inversion. The elevated maximum is all resolved scale energy,

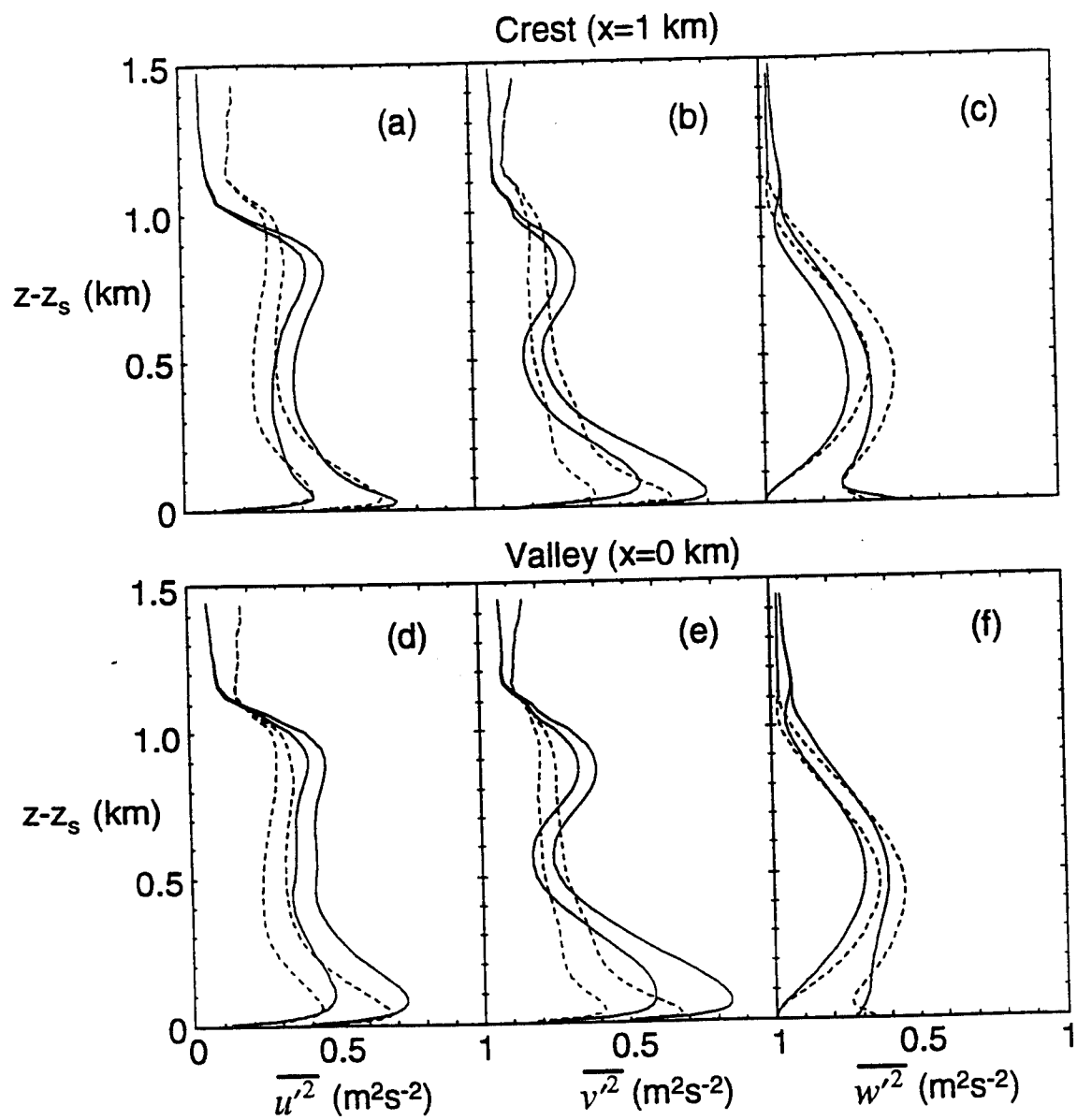


Figure 5-29. Vertical profiles of velocity variances for max. slope=0.125 at the hill crest and valley. The dashed lines are for the corresponding flat case. Both resolved and total variances are shown.

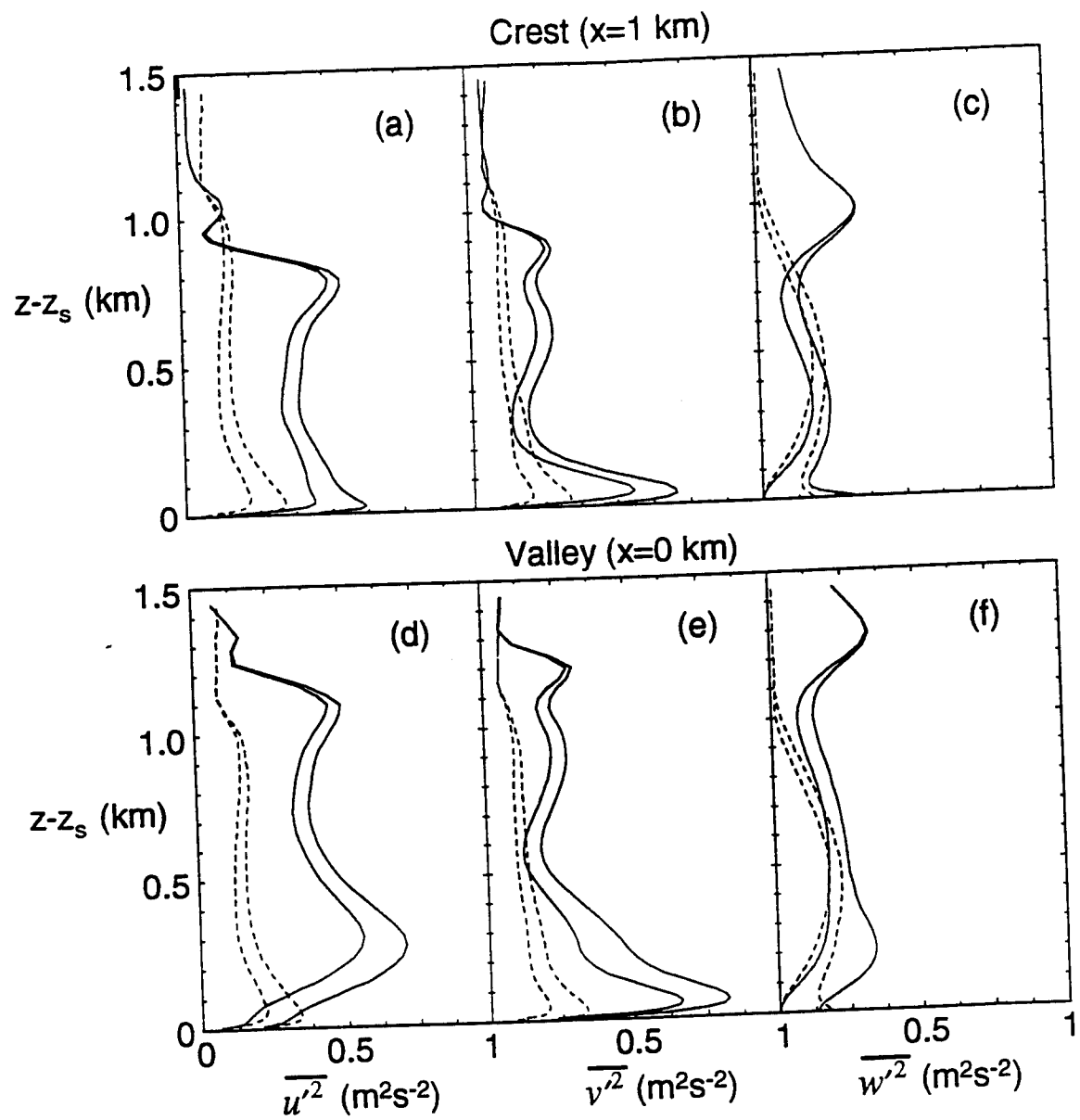


Figure 5-30. Vertical profiles of velocity variances for max. slope=0.5 at the hill crest and valley. The dashed lines are for the corresponding flat case. Both resolved and total variances are shown.

and examination of the instantaneous flow fields shows immediately that it is due to a wave disturbance in the stable region. The profiles in Figure 5-30 are obtained from averages in the  $y$ -direction as well as a time average, and a typical realization of the vertical velocity field at  $z=1200\text{m}$  is shown in Figure 5-31. A coherent wave pattern is clear, and seems to be associated with a roll-like convective structure in the boundary layer. The wave is aligned at  $30^\circ$  to the left of the geostrophic wind direction, consistent with the mean wind in the boundary layer. The Ekman balance between the mean boundary layer flow and the surface drag forces implies that large slope cases produce large angles between the rolls and the geostrophic direction. This increases the shear at the inversion and produces a stronger relative flow across the rolls, so that smaller slopes show much weaker wave disturbance. The trapped wave velocity variance is an unsteady feature that varies with the inversion structure and convection pattern; it does not appear to influence the turbulent layer significantly so the dynamics of the waves will not be pursued further.

The most dramatic feature of the turbulence response within the boundary layer is undoubtedly the increase in  $\overline{v'^2}$  near the surface. We are not aware of previous measurements or predictions of this phenomenon, and we therefore examine the mechanism in more detail. The instantaneous  $v$ -velocity field at  $\zeta=50\text{m}$  is shown in Figure 5-32, and intense regions of high transverse velocity are clearly visible. The regions are elongated in the direction of the near-surface flow and are located on the upslopes of the ridges. The high transverse velocities are associated with high streamwise vorticity, as can be seen in Figure 5-33. The  $x$ -component of vorticity at  $\zeta=80\text{m}$  shows very intense features along the upwind slopes, while the vertical section at  $x=500\text{m}$  (midway up the slope) shows localized vortices above the surface layer of negative vorticity. The surface layer is produced by the mean  $v$ -component of velocity in the Ekman layer, but the isolated vortices are clearly visible above it with both positive and negative signs and a scale of about  $250\text{m}$ .

The velocity fluctuations associated with these intense streamwise vortices are strongly affected by the presence of the solid boundary, since the vortices are close to the wall. This is the reason for the preferential manifestation of the kinetic energy in the  $v$ -component, rather than equally amongst  $v$  and  $w$ . An idealized reflective boundary condition at the wall would reduce the normal component of the velocity to zero and double the transverse velocity component, giving a strong enhancement of  $v'^2$  at the

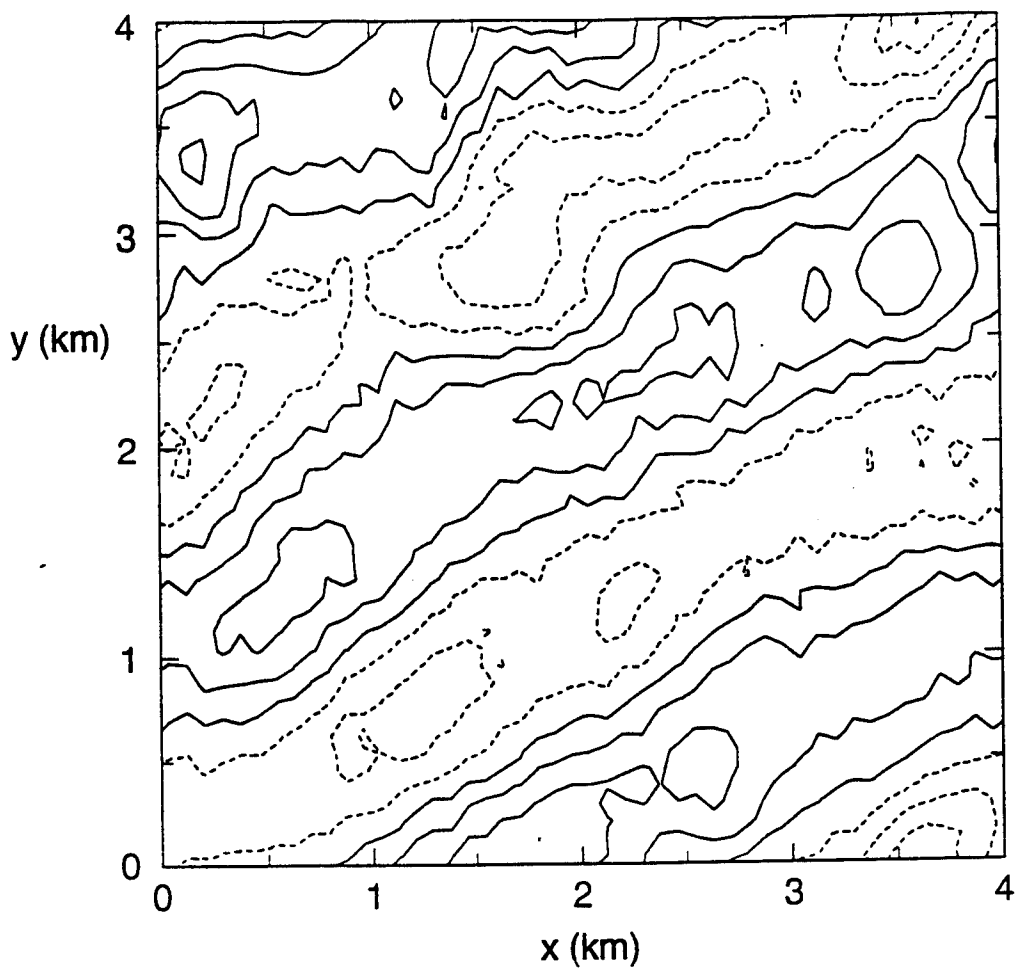


Figure 5-31. Vertical velocity at  $\zeta = 1200\text{m}$  for max. slope=0.5. Contour intervals are  $0.5 \text{ ms}^{-1}$ . Dashed contour lines indicate negative velocity.

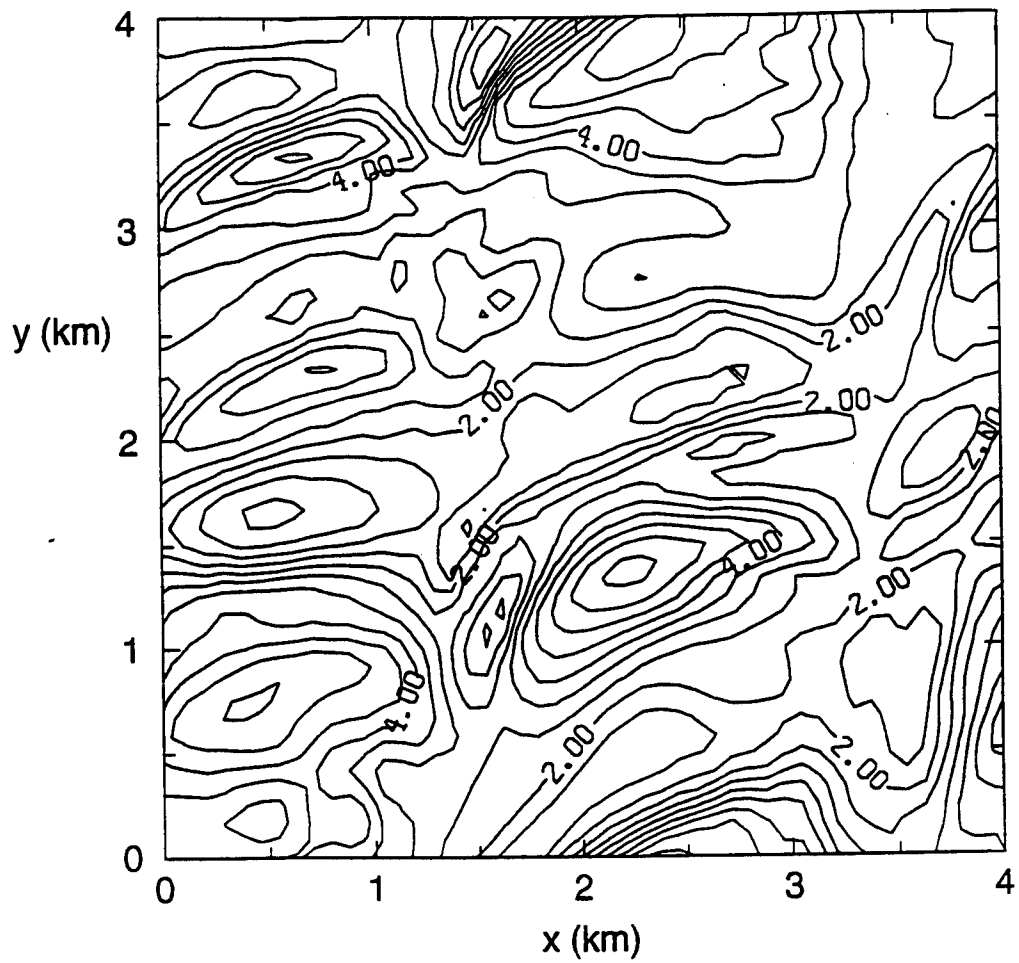


Figure 5-32. Transverse velocity at  $z=50\text{m}$  for max. slope=0.5. Contour intervals are  $0.5\text{ms}^{-1}$ .

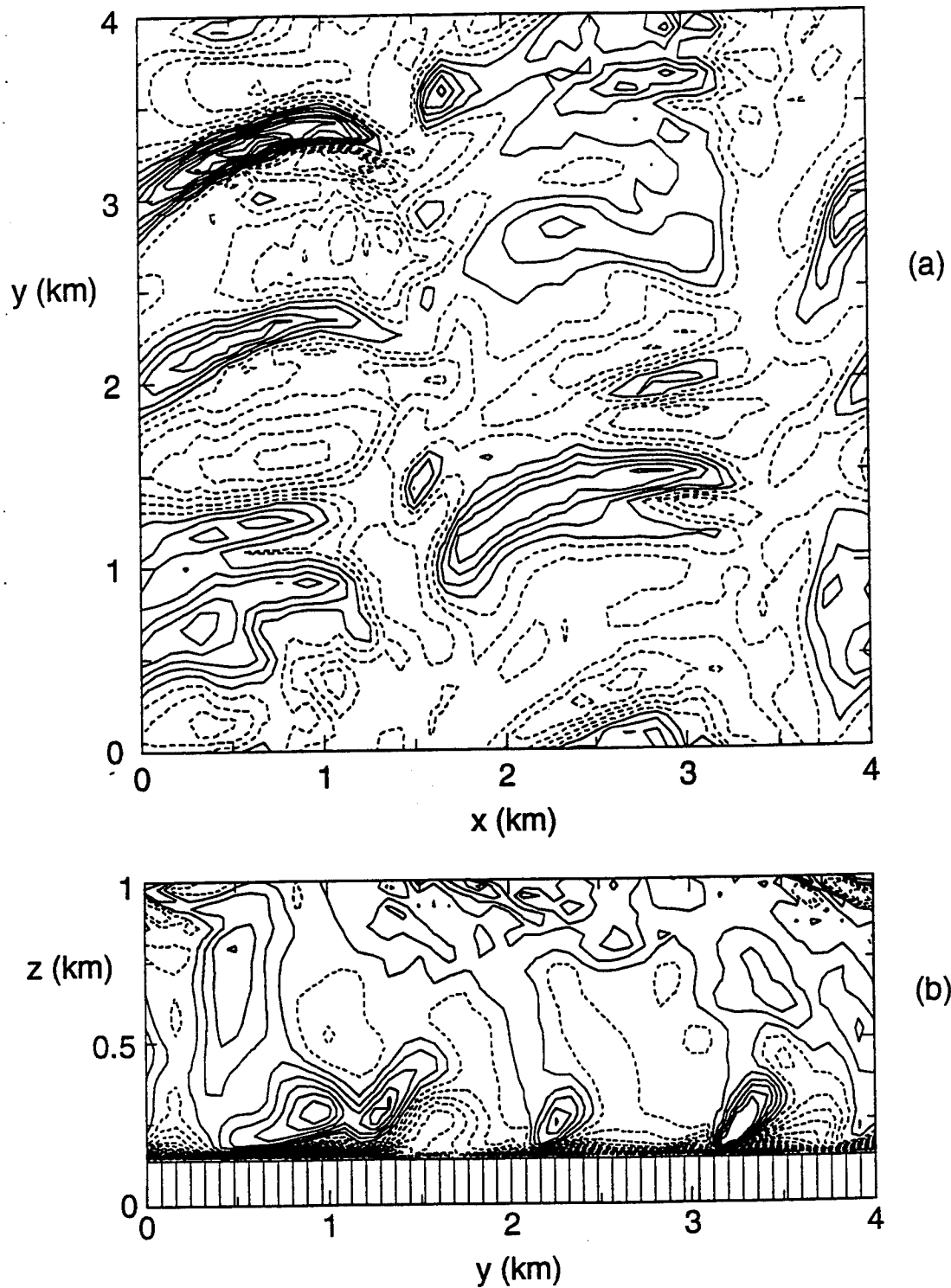


Figure 5-33. Streamwise component of vorticity for max. slope=0.5. Contour intervals are  $0.005\text{s}^{-1}$ . (a) at  $\zeta=80\text{m}$ , (b) at  $x=500\text{m}$ .

surface. The wall layer drag reduces the velocity very close to the surface, but the large increase in  $\bar{v}^2$  on the lower side of the vortex is clearly evident in the LES results. The vortices are reminiscent of the Taylor-Görtler vortices observed in boundary layer flow over a concave surface, e.g., Tani (1962), So and Mellor (1975) and Hoffman et. al. (1985). Although the main boundary layer is deep compared with the terrain scales, the velocity shear is largely confined to a relatively thin surface layer. The valley region presents a concave surface, and we might therefore expect production of coherent streamwise vortices in the local flow. However, the intensity of the vortices observed in our LES calculations appears to be significantly larger than experimental observations in curved boundary layer flow. This is due to enhancement by the shear distortion in the flow over the ridges. Experimental flows have generally involved minimal streamwise acceleration in an attempt to isolate the curvature mechanisms, but in the ridge flow the vorticity production occurs in a region of strong acceleration. Streamwise vorticity is enhanced by stretching of the vorticity field as the flow accelerates toward the crest of the ridge, increasing the  $v$ -velocity and also stabilizing the vortex. The rate of stretching of vorticity aligned with the mean flow direction is given by

$$2 \frac{\bar{u}_i \bar{u}_j}{\bar{u}_k \bar{u}_k} \frac{\partial \bar{u}_i}{\partial x_j}$$

and the spatial distribution of this quantity is illustrated in Figure 5-34. For linearized potential flow over a sinusoidal surface, the stretching rate is simply  $2e^{-2\pi z/\lambda} \partial h / \partial x$  where  $h$  is the surface elevation and  $\lambda$  is the terrain wavelength. The linearized vertical damping scale is therefore about 300m for the 2km ridges and the maximum stretching is located at the maximum slope on the upwind side of the ridge. The general shape of the stretching field in the nonlinear flow over the steep ridges is qualitatively similar to the linearized result, and the stretching rates are fast enough to produce significant increase in the local vorticity.

The persistence of the vortices is illustrated in Figure 5-35, which shows the  $v$ -velocity midway up the ridge slope and 40m above the surface as a function of time from the two runs with maximum slopes of 0.25 and 0.5. The slice across the 4km wide domain shows intermittent structure at a slope 0.25, with occasional 'streaks' of high speed flow lasting for about 1000s. At a slope of 0.5, however, two distinct narrow regions of very high  $v$ -velocity migrate in the positive  $y$ -direction at about  $3\text{ms}^{-1}$  for the whole 3000s period. The magnitude of the  $v$ -velocity in the streak is modulated over the

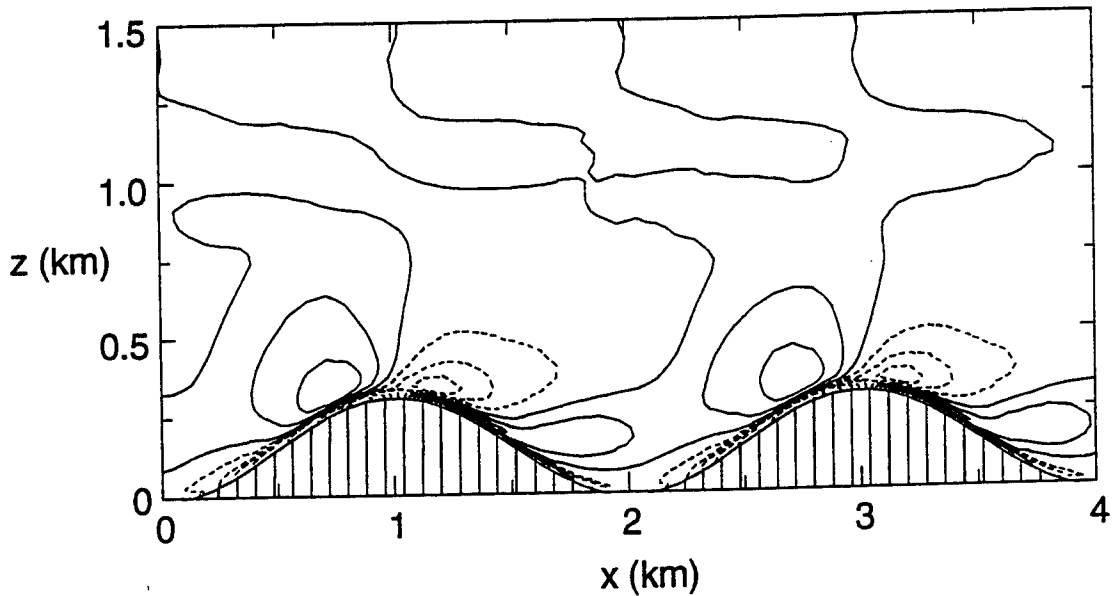


Figure 5-34. Stretching rate of vorticity aligned with the mean flow for max. slope=0.5.  
Contour increments are  $5 \times 10^{-4} \text{ s}^{-1}$ .

time period but the identity of the structure is maintained throughout, providing strong evidence of the stability of these vortices. The difference in persistence time between the two slope cases seems to be related to the existence of a reverse flow in the valley. At a slope of 0.5, the separated flow region is much more complex than the classical curved boundary layer of the Taylor-Gortler instability, and streamwise vorticity is probably generated through instabilities of the separating shear layer. The strong stretching mechanism is centered on the reattachment point, however, and vortices are therefore almost fixed relative to the terrain surface. Once initiated, a vortex can evidently sustain itself under the stretching action for long time periods.

The vorticity production mechanism discussed above is controlled by the Taylor-Gortler instability mechanism, which depends on the velocity profile shape over the concave valley surface. The vertical extent of the instability is determined by the profile shear and will therefore depend on surface roughness. The turbulence enhancement induced by the vortex stretching mechanism, on the other hand, scales with the wavelength of the terrain and does not depend strongly on factors like the surface roughness or boundary layer stability. Figure 5-36 shows the  $v'^2$  profiles for different roughness lengths at the mid-point of the upslope. It can be seen that the depth of the

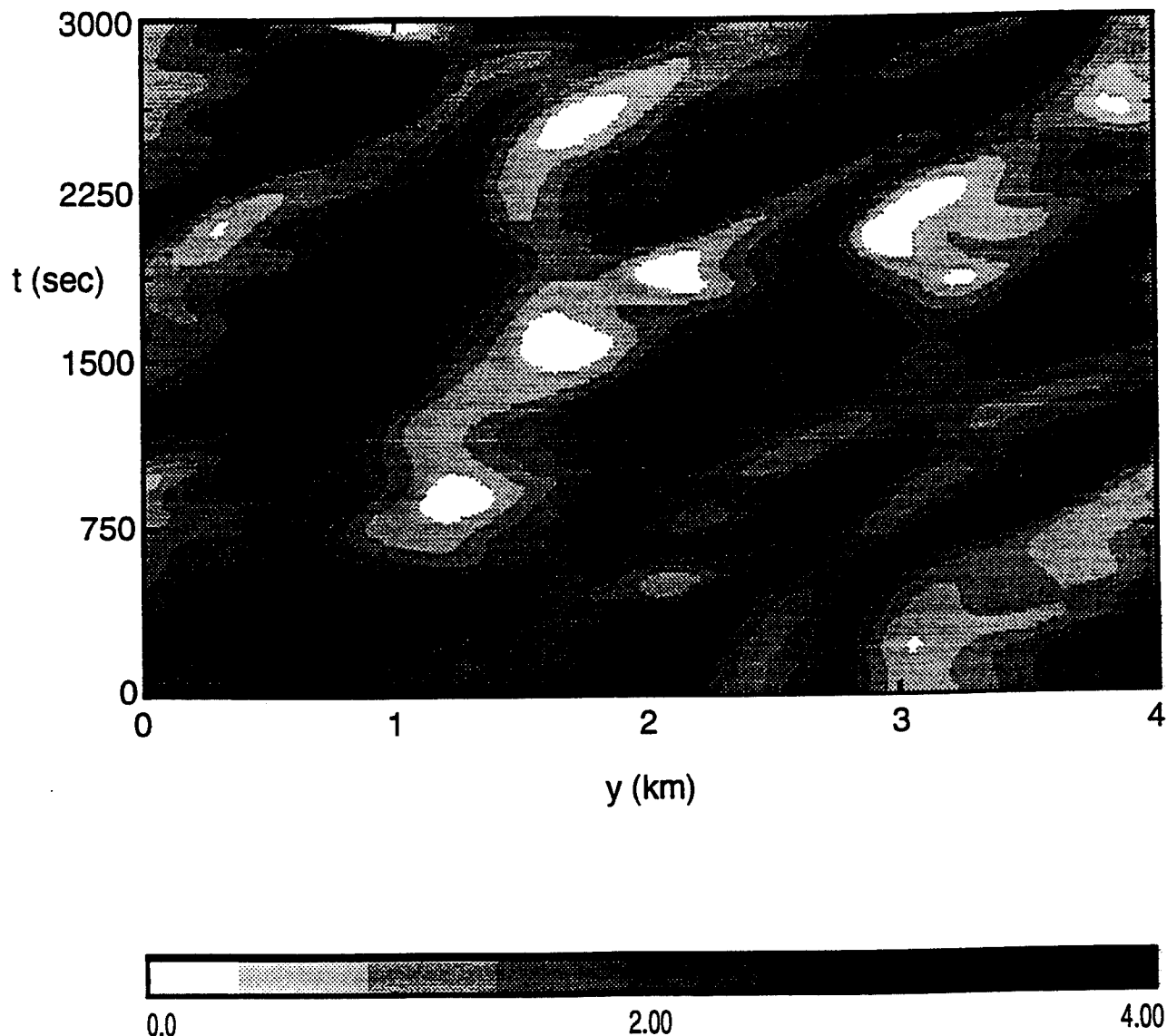


Figure 5-35. Transverse velocity at  $x=500\text{m}$ ,  $z=40\text{m}$  as a function of time and  $y$  for  
(a) max. slope=0.25, (b) max. slope=0.5.

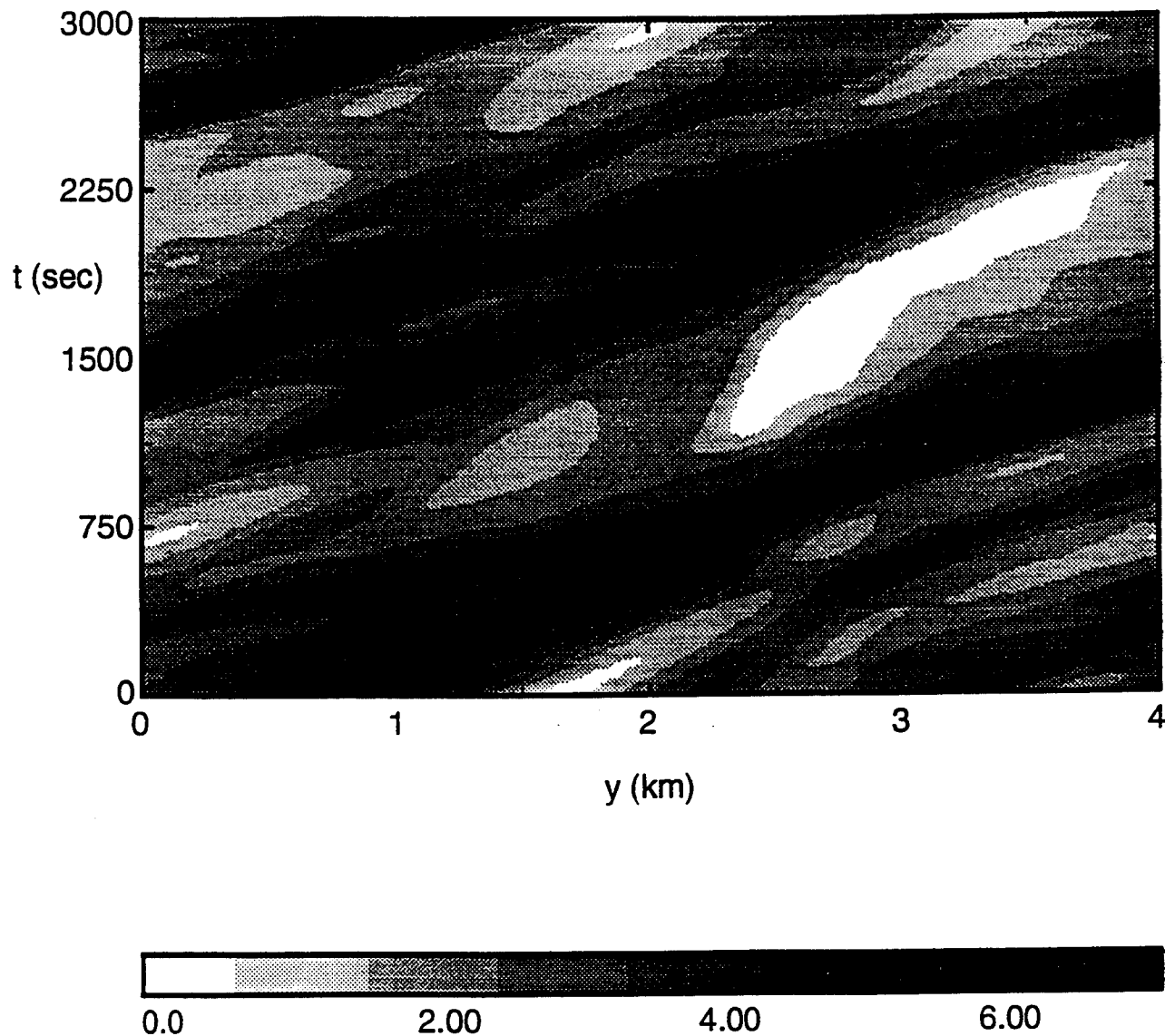


Figure 5-35. Transverse velocity at  $x=500m$ ,  $z=40m$  as a function of time and  $y$  for  
(a) max. slope=0.25, (b) max. slope=0.5 (Continued).

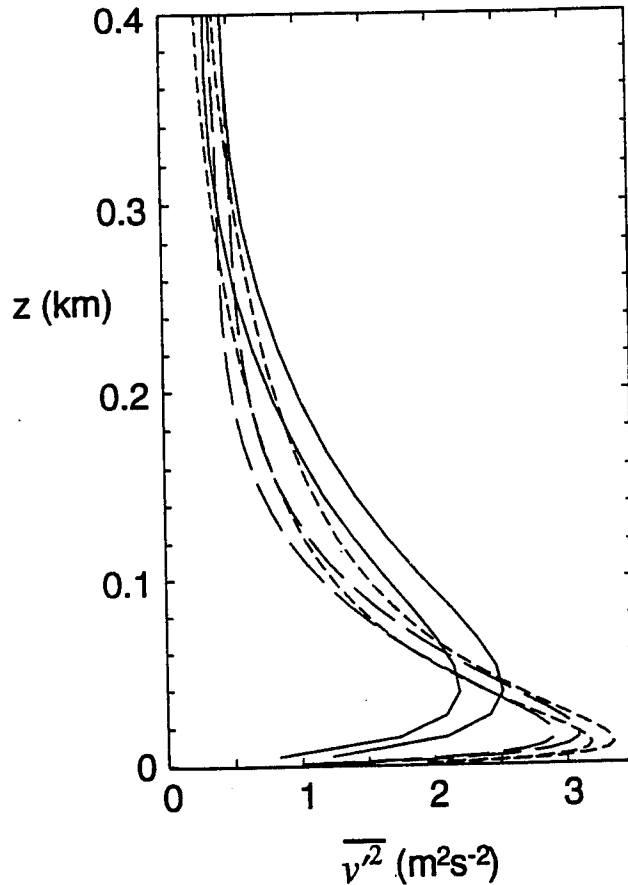


Figure 5-36. Vertical profiles at  $x=500\text{m}$  of total and resolved transverse velocity variance for max. slope=0.5. Solid lines:  $z_0=1\text{m}$ ; long dashes:  $z_0=0.1\text{m}$ ; and short dashes:  $z_0=0.01\text{m}$ .

enhanced  $\overline{v'^2}$  layer does decreases with roughness, although the magnitude also appears to be roughness-dependent.

Figure 5-37 shows the turbulence profiles for a case with smaller buoyancy flux, but other parameters as in Figure 5-30. The increase in  $\overline{v'^2}$  near the surface is again obvious, suggesting the importance on the near-surface shear instabilities and the stretching effect, since neither mechanism depends on buoyancy or convective eddies. The flat terrain profiles show that the turbulence is not dominated by convection in this case, since the variances maximize close to the ground.

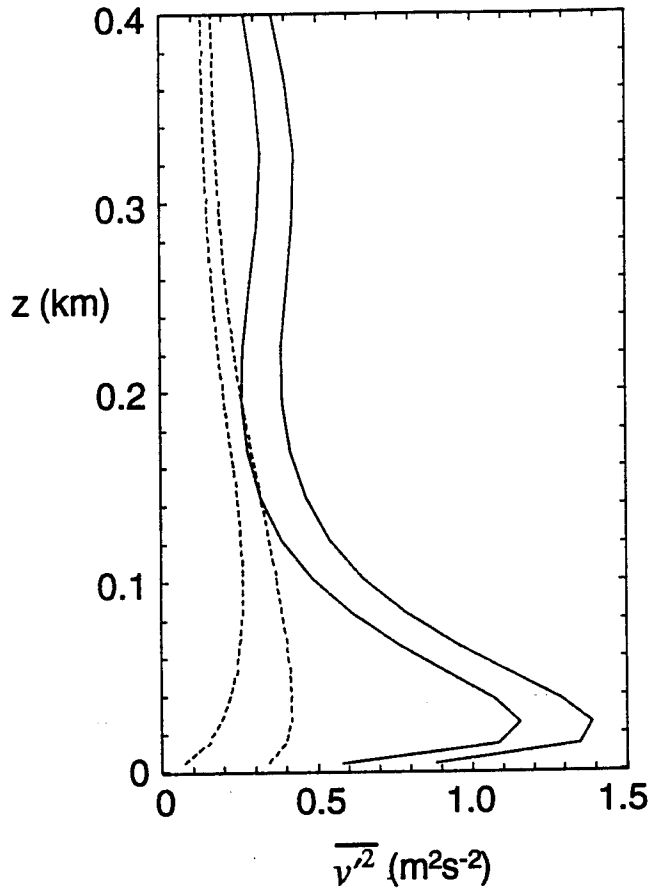


Figure 5-37. Vertical profiles at  $x=500\text{m}$  of resolved and total transverse velocity variance for max. slope=0.5,  $H_0=0.0045^\circ\text{Cms}^{-1}$ . The dashed lines are for the corresponding flat case.

### 5.6.2 Heat and Momentum Fluxes.

The off-diagonal Reynolds stresses are subject to the same rapid distortion effects as the velocity variances, so that the eddy viscosity relation is only valid close to the surface. The vertical profiles of momentum and heat fluxes from the small slope case with 2km ridges are shown in Figure 5-38, and compared with the flat terrain case. The profiles of  $\overline{u'w'}$  and  $\overline{v'w'}$  are very similar in character, and show the major features seen in observational studies. The Reynolds stresses shows an elevated minimum over the crest of the ridges, with a maximum at the surface and an increase from the flat terrain profile at higher altitudes. The elevated  $\overline{u'w'}$  minimum is just below  $z=100\text{m}$  while the  $\overline{v'w'}$  minimum is around 200m. Estimates of the height of the stress minimum from the neutral flow analyses of Sykes (1980) and Belcher et al. (1993) are close to the inner layer scale height, and the theoretical prediction has been compared with field

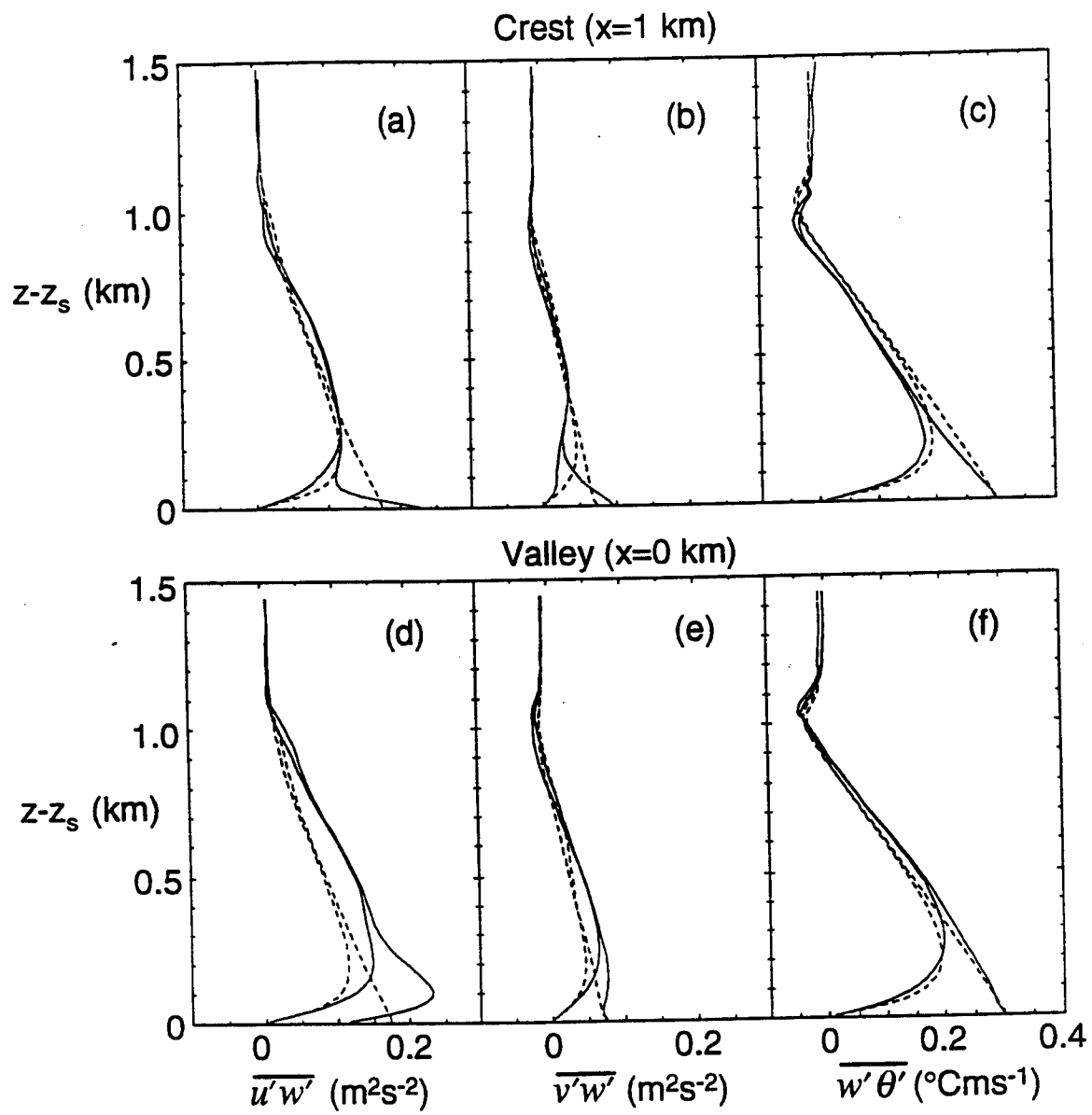


Figure 5-38. Vertical profiles of vertical fluxes for max. slope=0.125 at the hill crest and valley. The dashed lines are for the corresponding flat case. Both resolved and total fluxes are shown.

observations by Belcher et al. Using the definition of the inner scale from Belcher et al. and assuming the horizontal scale of the sinusoidal ridges as  $L = \lambda/4$ , the inner scale is obtained from the expression

$$l_s \ln(l_s / z_0) = 2\kappa^2 L \quad (5.39)$$

as  $l_s \approx 50$ m. The result in Figure 5-38 is somewhat higher than this estimate and may be affected by the LES resolution. The minimum in  $\overline{u'w'}$  is located at the point where the resolved scale component begins to dominate, and could possibly move downward if the resolution was increased. The agreement with the theoretical estimate is reasonably good, however, and indicates that most of the flux transport is adequately resolved in this calculation.

The momentum flux profiles in the valley show the opposite phase in the perturbation near the ground, but the fluxes are increased throughout the main boundary layer. The fluxes are generally higher over the valley at heights above the inner layer scale, and are similar to the velocity variances, which indicate a nonlinear response at this slope and a net increase in the turbulence level. The increase in average momentum flux is manifested in the total surface drag, discussed in Section 5.5, which shows a pressure force of roughly 10% of the flat stress value.

The heat flux perturbations show a simpler response than the Reynolds stresses, with a reduction above the crest and an increase over the valley. The surface heat flux is a prescribed constant for the flow, so there can be no net change over the ridges, but there is also no indication of an inner layer in these profiles.

At a larger slope, the flux perturbations are much more significant. Figure 5-39 shows the profiles for a slope of 0.5. The large increase in surface drag is reflected in the  $\overline{u'w'}$  profiles, particularly over the valley, where the momentum flux across the separating shear layer is clearly the dominant transfer mechanism. The profile over the crest still shows the elevated minimum, at a slightly lower elevation than the small slope case and a similar response in  $\overline{v'w'}$ . The bulk of the transfer of v-momentum is also located near the shear layer above the valley, but the flux profiles show considerable oscillation with altitude. The heat flux is also clearly reduced over the hill crest and augmented above the valley. The full two-dimensional structure of the fluxes is illustrated in Figure 5-40, which shows the heat flux maximizing on the lee slope of the ridges; apparently the convective eddies are preferentially initiated in the upslope flow of the separation region. The heat absorbed on the windward slope is not sufficient to

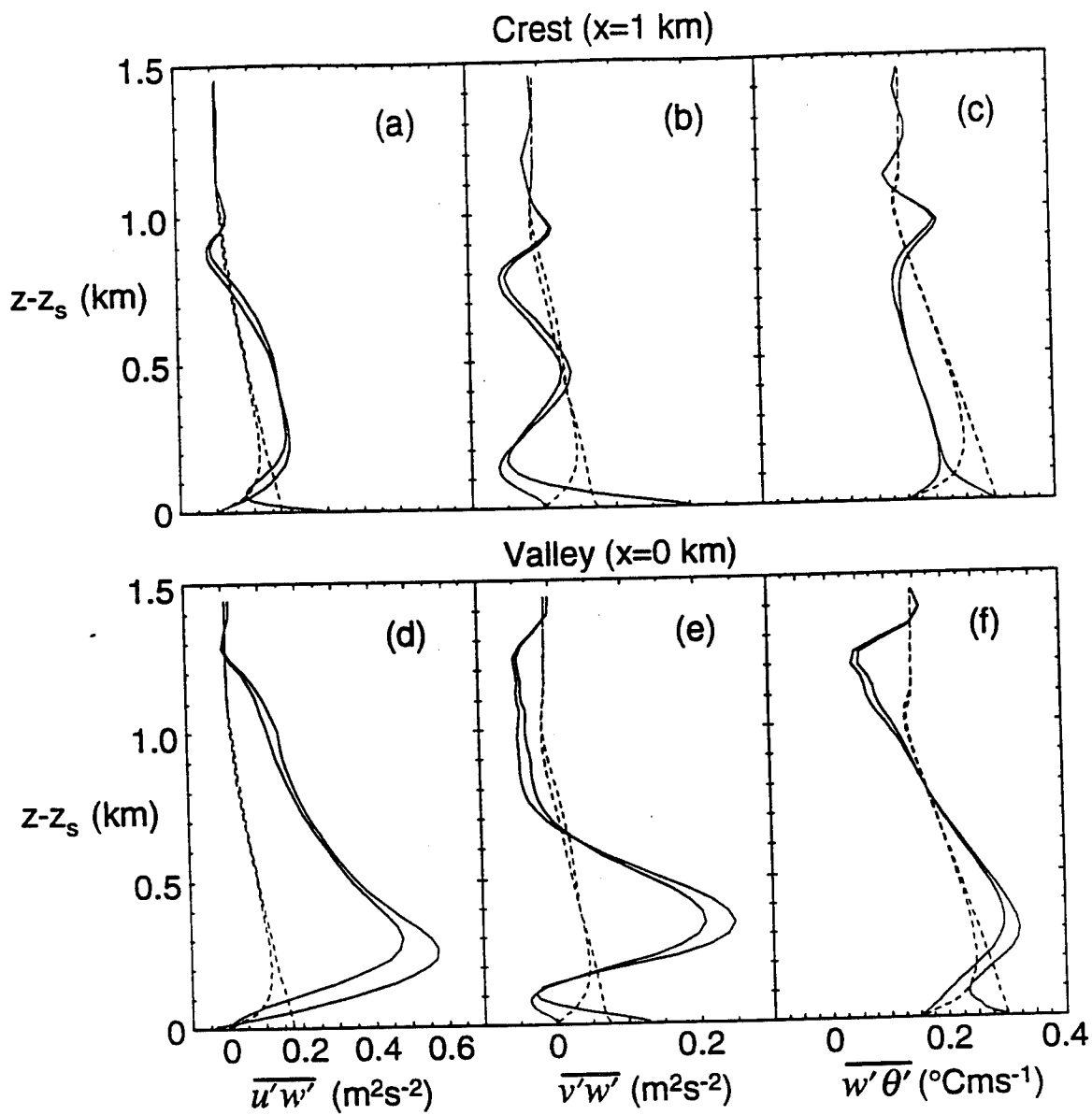


Figure 5-39. Vertical profiles of vertical fluxes for max. slope=0.5 at the hill crest and valley. The dashed lines are for the corresponding flat case. Both resolved and total fluxes are shown.

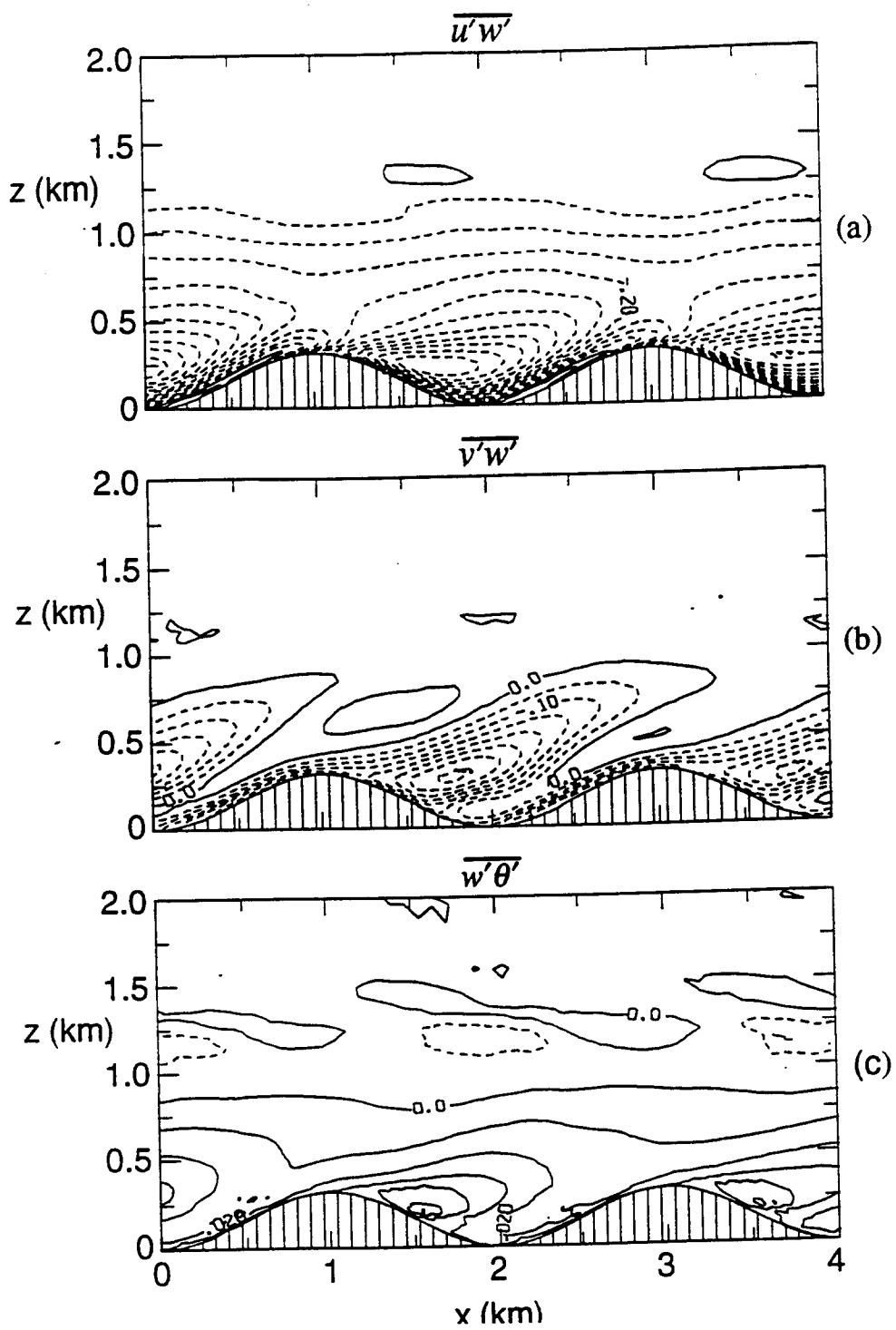


Figure 5-40. Vertical profiles of momentum and heat fluxes for max. slope=0.5.  
 Contour intervals are  $0.05\text{m}^2\text{s}^{-2}$  for momentum fluxes and  $0.01^\circ\text{Cms}^{-1}$  for heat flux. (a)  $u$ -momentum, (b)  $v$ -momentum, (c) heat.

promote upwind separation, but produces a buoyant separating shear layer that tends to rise and form a convective updraft.  $\overline{v'w'}$  also shows the strong maximum in the shear layer that continues up to the inversion, producing large horizontal variations throughout the depth of the boundary layer. This contrasts with  $\overline{u'w'}$  and  $\overline{w'\theta'}$ , which become more horizontally uniform above the hills.

### 5.6.3 Dispersion Effects.

The turbulence levels over complex terrain are generally increased relative to flat terrain. Grant and Mason (1989) have suggested that the turbulence above the crests of the hills is comparable to that over a flat surface with an equivalent surface stress, and there is rough confirmation of this hypothesis in the LES results. As we have seen, the flow field is nearly homogeneous in the horizontal at heights more than about 100m above the ridge crests; this statement does not apply to flux of the momentum component along the ridge,  $\overline{v'w'}$ , but the variance profiles and  $\overline{u'w'}$  profiles are close to homogeneous. Turbulence variances do not show exactly the same shape as a flat terrain profile, but the magnitudes are comparable. We should therefore expect enhanced dispersion over complex terrain, and the application of the simple modeling scheme of Section 2 should produce the correct trends. The total surface forces obtained from (5.38) should be used to estimate  $u_*$  in the parameterization. However, the actual dispersion process is more complicated than a simple increase in turbulence intensity.

In order to obtain a picture of the dispersion effects, the LES calculation was used to track a number of "massless" Lagrangian particles for a period of time. The particles were released into the convective boundary layer over terrain of slope 0.5, as illustrated in Figure 5-3. This is a separated flow, and the turbulence intensities are shown in Figure 5-28. A cluster of 100 particles were released into the fully developed turbulent flow at time  $t=0$ , say. The particles were initially located in a 10x10 array over a 250m horizontal square at an altitude of 400m. The square was positioned above the crest of the ridge, which has an elevation of 318m for this case. The particles are transported by the resolved scale eddy field, and no subgrid diffusion effects were included.

The subsequent positions of the particles at 15min intervals out to  $t=1$  hour are shown in Figure 5-41. The cluster only provides a rough estimate of the dispersion effects, but it is clear that there is a rapid spread of the distribution. The mean wind direction is clear in the plan view, with particles moving almost  $45^\circ$  to the left of the

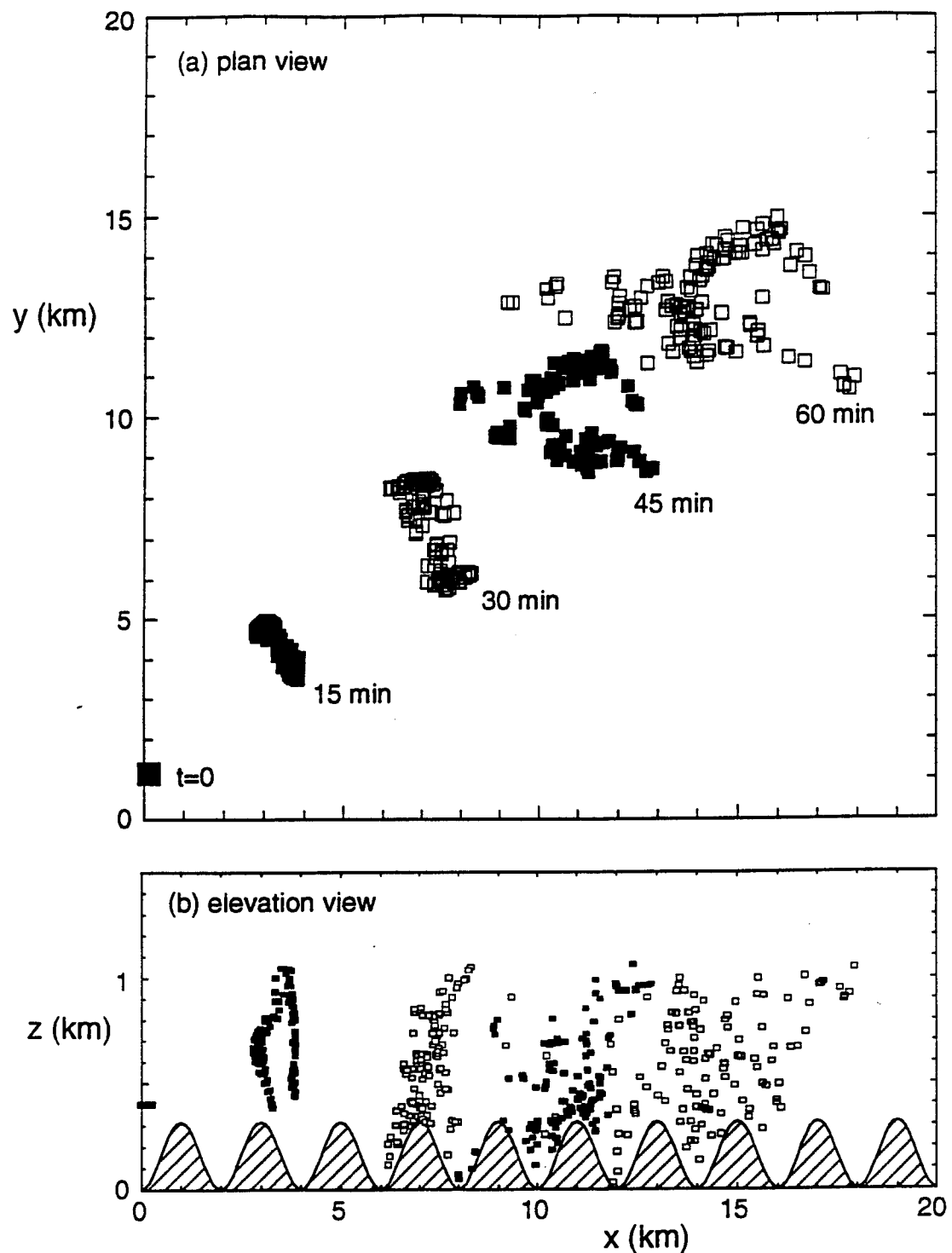


Figure 5-41. Particle dispersion over 1 hour from a localized release in convective flow over periodic ridges. maximum terrain slope is 0.5, and geostrophic wind is  $5\text{ms}^{-1}$  in the  $x$ -direction.

geostrophic wind direction, i.e., the positive  $x$ -direction. This is to be expected from the surface force results, which determine the mean boundary layer velocity through the balance with the Coriolis force. The particles spread more rapidly in the  $x$ -direction, and the elevation view shows that the spread is closely associated with the trapping and retardation of particles in the valleys. The flow is turbulent, so that even though the mean streamlines are closed within the recirculation region there is a strong exchange of fluid between the valleys and the overlying boundary layer. The spread in the  $x$ -direction is about 8km over the 1 hour period, while that in the  $y$ -direction is about 3km. The latter is consistent with the magnitude of  $\overline{v^2}$ , as shown in Figure 5-28, but the  $x$ -spread is much larger than implied by the  $\overline{u^2}$  distribution. The mean flow variations are clearly responsible for much of the diffusion in the  $x$ -direction, and this must be accounted for in a proper description of dispersion in complex terrain.

The mean flow effects can be represented in late-time dispersion models through appropriate specification of the mean wind profile over complex terrain. The flow field shown in Figure 5-3 can be averaged in the horizontal, and will yield a much larger wind shear than the boundary layer over flat terrain. The total integrated shear must be the same, since the velocity is zero at the wall and approaches the geostrophic value above the PBL. However, the shear is concentrated in a shallow layer at the surface over flat terrain. The effect on particle dispersion is therefore limited to a small fraction of the cloud near the ground. The profiles over the ridges show that the shear is distributed over a much deeper layer, certainly extending above the crests, and may even produce significant reverse velocities in the separation regions. This increased depth of influence is responsible for the increased diffusion in the  $x$ -direction, since a large fraction of the boundary layer is now affected by the shear.

We have not been able to perform a sufficient number of dispersion calculations to provide quantitative statistics on cloud spread rates for the range of meteorological conditions and release locations considered in the study, but the limited information obtained gives insight into the dominant processes that need to be considered. A simple means of estimating the dispersion enhancement over complex terrain will be discussed in Section 5.8.

## 5.7 PARTICLE DEPOSITION RATES.

The turbulent deposition of small particles has been shown to be an important removal mechanism in the PBL, and practical parameterization schemes were discussed in Section 4. The principal flow parameters determining the deposition rate were the surface roughness (or vegetative canopy characteristics) and the surface stress (or turbulence levels). The presence of terrain has a strong influence on the surface stress and local turbulence levels, so we must consider the effects of terrain on particle deposition rates.

The LES model discussed earlier in this section included a conservation equation for a scalar species with the surface deposition parameterization given by (4.18)-(4.21) in Section 4. Several model runs were conducted with a scalar species introduced into the boundary layer, and the average deposition rate over the computational domain was calculated. The rate was determined as the ratio of the average surface flux of scalar quantity to the average concentration at the lowest model grid level. The grid location is somewhat arbitrary, but is fixed for the series of runs and therefore provides a standard definition. The flux of scalar depends on the instantaneous, local value of the surface stress, as does the local concentration, but the quantities discussed in this section are averaged over the 4km x 4km domain and over a 3000s time period.

Table 5-2 shows the effective deposition velocities for a number of LES runs with different terrain parameters. It is apparent from the table that the slope of the terrain does not produce a marked effect on the effective deposition velocity, in contrast with the momentum transfer results of Section 5.5. It seems that the deposition velocity is hardly changed by the presence of terrain, and this insensitivity can be understood from the fact that the turbulent deposition is determined by the surface stress distribution. A large component of the increased surface force is due to the pressure force on the hills, while the average tangential stress component is generally reduced slightly over the ridges. The pressure force transfers momentum but has no comparable role in the particle deposition rate. The deposition is more closely related to the tangential force, but depends on the magnitude of the stress. The  $x$ -component is reduced by the terrain, but the  $y$ -component is generally increased; the overall average magnitude is therefore much less sensitive to terrain variations.

**Table 5-2. Deposition velocity for 10 $\mu\text{m}$  particles over terrain.**

Surface roughness (m)	Ridge wavelength (km)	Maximum slope	Deposition velocity (cm/s)
0.01	2	0.25	0.4
0.01	2	0.50	0.6
0.1	2	0.25	1.4
0.1	2	0.50	1.5
1.0	1	0.50	5.7
1.0	2	0.25	4.8
1.0	2	0.50	6.3
1.0	4	0.25	6.7
1.0	4	0.50	6.3

Table 5-2 strongly suggest that the representation of deposition rates over complex terrain should utilize the tangential force parameterizations from (5.38) in determining the effective  $u_*$ , but continue to use the flat terrain deposition scheme of Section 4.

## 5.8 IMPLEMENTATION IN LATE-TIME MODELS.

We have briefly suggested some of the directions for implementing the terrain representations in late-time models. One of the key aspects of such representations is the need to describe larger scale processes, so that the statistical average over a region of complex terrain is appropriate. Detailed calculations for particular local terrain conditions requires a detailed simulation of the local flow field; we are concerned here with larger scale effects. We need to represent both mean boundary layer transport and the effective dispersion rates, both horizontal and vertical, in complex terrain. Deposition

rates were discussed in Section 5.7, and a simple scheme was recommended based on the tangential force parameterization (5.38).

We assume that the large scale wind field used to drive the late-time dispersion model will not contain a detailed terrain parameterization for the PBL, so that the available winds are closer to geostrophic values. Under these conditions a simple time-dependent scheme for estimating the mean boundary layer wind can be obtained from the integrated momentum equations (5.25), and the definition of the mean boundary layer velocity,  $u_B$ , in (5.27). The equations can be written

$$\frac{\partial u_B}{\partial t} = -f(v_B - v_g) + \frac{F_x}{z_i} \quad (5.40a)$$

$$\frac{\partial v_B}{\partial t} = f(u_B - u_g) + \frac{F_y}{z_i} \quad (5.40b)$$

The surface force,  $F$ , is determined from the previously developed parameterizations (5.38), and the inversion depth,  $z_i$ , is obtained from either the meteorological fields, or from a prediction scheme such as METPRO (see Section 2).

The dispersion rates in complex terrain were shown to be a result of both turbulence and mean flow effects. The turbulence intensities were discussed in Section 5.6, where the surface force parameterization was suggested as a basis for estimating the large-scale average velocity variance profiles. The effect of the mean flow perturbations can be modeled by including a mean wind shear in the boundary layer wind profile. The wind shear provides a persistent effect on the particle dispersion, and models the effect of the slow moving air in the sheltered valley regions. We emphasize that we are representing the large scale processes over a number of terrain features, not the detailed flow distortion around a particular hill. The boundary layer wind and turbulence profiles should be thought of as a large scale area average, over a horizontal area of  $100\text{km}^2$ , say.

Unfortunately, limitations on time have prevented an extensive study of the quantitative dispersion mechanisms for the range of meteorological and terrain parameters studied in the numerical simulations. We therefore suggest a basic parameterization scheme, with numerical parameters specified to the best of our current knowledge. We expect that the representation could be refined by further investigation of the LES results. The assumption in the scheme is that the effect of the slow moving air in the valleys can be modeled as a simple linear shear profile in the velocity. Under

homogeneous mixing conditions, the wind shear is usually confined to thin layer at the ground and the inversion. The shear does not produce strong dispersion of material under these circumstances. We therefore propose that the wind profile include a linear regime in the lower part of the boundary layer, with a maximum reduction that depends on the r.m.s. slope of the topography, and a depth that depends on the r.m.s. height of the terrain. The simplest model incorporating these effects is

$$u_i = u_{0i} - c_2 \left( 1 - \frac{z}{c_1 \sigma_h} \right) \frac{s_{ij} u_{0j}}{\sqrt{\lambda(s)}}$$

for  $z < c_1 \sigma_h$ , and  $u = u_0$  above. The mean velocity is required to be  $u_B$ , so this determines  $u_0$  if the other quantities are prescribed. As a preliminary estimate, we suggest that  $c_1=2.5$ , and  $c_2=2$ .

## SECTION 6

### CONCLUSIONS

The representation of planetary boundary effects on the distribution of near-surface dust in late-time modeling of nuclear clouds has been considered. Representations of the boundary layer turbulence and effective diffusivity have been recommended for application in the models. The diffusivity estimate is based on recent turbulence closure models, and provides a generalized description of the boundary layer based on a small number of boundary layer parameters. The boundary layer parameters include the wind speed and surface fluxes, in addition to the surface roughness and boundary layer depth, and a simplified scheme for determining the fluxes using the METPRO meteorological pre-processor (Paine, 1987) is recommended.

A relatively detailed examination of the effect of dust on the solar radiative flux transport was conducted, since the solar heating is a major component of the boundary layer energy input. A preliminary study indicated that concentrations of small particles, i.e., smaller than  $10\mu\text{m}$  diameter, at levels of around  $10^{-7}\text{g/cc}$  could produce significant effects on the radiative transfer. Such concentrations are feasible in a multiburst scenario, so detailed dynamic calculations were performed using the ARAP turbulence closure model and the delta-Eddington radiative flux model. The effect of a dense dust cloud is to absorb the solar flux in the upper portion of the cloud, preventing the flux from reaching the ground. This removes the buoyancy generation mechanism from the planetary boundary layer, and suppresses the turbulent diffusion near the surface. The lower part of the cloud remains unmixed during the daytime as a result of this suppression. The absorbing part of the dust cloud, however, is lofted by the heating and maintains a low level of turbulent mixing. The representation of these effects in a late-time dispersion model is a difficult problem. Late-time models are traditionally passive in nature, i.e., the dust is transported and diffused but does not induce its own velocity field. The effective radiation reaching the surface can be estimated from area-averaged vertical integrals of the dust, so that a crude estimate of the surface heating changes can be included, but the representation of the dynamic lofting mechanism requires a more detailed dynamic model.

Turbulent deposition of particles at the surface is an important process for small dust particles, and parameterizations for inclusion in late-time models have been suggested. The models represent the effects of particle size and the nature of the vegetative canopy or surface roughness, if details are available. The models are simple enough for practical calculation, and provide a reasonably accurate description of laboratory data.

Most of the existing boundary layer representations are appropriate for flat, homogeneous terrain, but most real applications involve flow over hills and valleys. In order to improve our understanding of flow over terrain and provide a basis for representing the effects in late-time dispersion models, numerical simulations of atmospheric boundary layer flow over topography under convective conditions have been performed for a range of meteorological conditions and terrain shapes. The bulk of the turbulent velocity fluctuations have been resolved using the Large-Eddy Simulation technique with a terrain-following coordinate transformation. An extensive set of simulations was conducted to examine the flow response to variations in terrain amplitude and wavelength, surface roughness, boundary layer stability, and geostrophic flow direction for idealized sinusoidal ridges.

Terrain wavelengths between 1km and 4km were studied, with maximum slopes up to 0.5. Surface roughness length was varied between 1cm and 1m, and geostrophic flow direction was varied relative to the ridge orientation. In addition, the stability was varied by changing the surface heat flux and geostrophic wind speed. Mean flow fields and surface forces were the principal focus of the study. The surface forces were analyzed and used to develop a simplified parameterization scheme for late-time dispersion models using the average boundary layer velocity.

The LES results have been used to derive a simplified surface drag parameterization for convective flow over more general topography, utilizing the results from simulations with different shaped ridges and three-dimensionality. The simulations also provide insight into the enhanced horizontal dispersion rates in complex terrain, and a simple estimate for general conditions has been recommended. The LES calculations showed that particle deposition rates are not as strongly modified by terrain, and the flat surface parameterization can be used in complex terrain, provided the surface friction velocity is estimated from the tangential stress force, i.e., the pressure force should not be included.

## SECTION 7

### REFERENCES

- Amiro, B. D. (1990), "Comparison of turbulence statistics within three boreal forest canopies", *Boundary-Layer Met.*, **51**, 99-121.
- Bache, D. H. (1979a), "Particle transport within plant canopies - I. A framework for analysis", *Atmos. Env.*, **13**, 1257-1262.
- Bache, D. H. (1979b), "Particle transport within plant canopies - II. Prediction of deposition velocities", *Atmos. Env.*, **13**, 1681-1687.
- Bache, D. H. (1984), "Prediction of the bulk deposition velocity and concentration profiles within plant canopies", *Atmos. Env.*, **18**, 2517-2519.
- Batchelor, G. K. and I. Proudman (1954), "The effect of rapid distortion on a fluid in turbulent motion", *Quart. J. Mech. Appl. Math.*, **7**, 83-103.
- Belcher, S. E., T. M. J. Newley and J. C. R. Hunt (1993), "The drag on an undulating surface induced by the flow of a turbulent boundary layer", *J. Fluid Mech.*, **249**, 557-596.
- Britter, R. E., J. C. R. Hunt and K. J. Richards (1981), "Airflow over a two-dimensional hill: studies of velocity speed-up, roughness effects and turbulence", *Quart. J. Roy. Met. Soc.*, **105**, 91-111.
- Businger, J. A. (1973), "Turbulent transfer in the atmospheric surface layer", *Workshop on Micrometeorology*, ed. D. A. Haugen, American Meteorological Society, Boston.
- Businger, J. A., J. C. Wyngaard, Y. Izumi and E. F. Bradley (1971), "Flux-profile relationships in the atmospheric surface layer", *J. Atmos. Sci.*, **28**, 181-189.
- Businger, J. A. (1986), "Evaluation of the accuracy with which dry deposition can be measured with current micrometeorological techniques", *J. Clim. & Appl. Met.*, **25**, 1100-1124.

Chamberlain, A. C. (1967), "Transport of *Lycopodium* spores and other small particles to rough surfaces", *Proc. Roy. Soc.*, **296A**, 45-70.

Clark, T. L. (1977), "A small-scale dynamic model using a terrain-following coordinate transformation", *J. Comp. Phys.*, **24**, 186-215.

Csanady, G. T. (1973), "*Turbulent diffusion in the environment*", D. Reidel, 248pp.

Davidson, C. I. and S. K. Friedlander (1978), "A filtration model for aerosol dry deposition: application to trace metal deposition from the atmosphere", *J. Geophys. Res.*, **83**, 2343-2352.

Davidson, C. I., J. M. Miller and M. A. Pleskow (1982), "The influence of surface structure on predicted particle dry deposition to natural grass canopies", *Water Air Soil Pollut.*, **18**, 25-43.

Deardorff, J. W. (1970), "Convective velocity and temperature scales for the unstable planetary boundary layer and for Rayleigh convection.", *J. Atmos. Sci.*, **27**, 1211-1213.

Deardorff, J. W. (1972), "Parameterization of the planetary boundary layer for use in General Circulation Models", *Mon. Wea. Rev.*, **100**, 93-106.

Fiedler, F. and H. A. Panofsky (1972), "The geostrophic drag coefficient and the effective roughness length", *Quart. J. Roy. Met. Soc.*, **98**, 213-220.

Friedlander, S. K. (1977), "*Smoke, Dust and Haze*", Wiley, New York, 317pp.

Fuchs, N. A. (1964), "*The Mechanics of Aerosols*", Pergamon, New York.

Gill, A. E. (1982), "*Atmosphere-ocean dynamics*", Academic Press, New York, 662pp.

Gould, T. R. and C. I. Davidson (1992), "Variability and uncertainty in particle dry deposition modeling", Fifth International Conference on Precipitation Scavenging and Atmosphere-Surface Exchange, July 1991, Richland, WA, 1115-1123, Hemisphere.

Grant, A. L. M. and P. J. Mason (1990), "Observations of boundary-layer structure over complex terrain", *Quart. J. Roy. Met. Soc.*, **116**, 159-186.

Hoffman, P. H., K. C. Muck and P. Bradshaw (1985), "The effect of concave surface curvature on turbulent boundary layers", *J. Fluid Mech.*, **161**, 371-403.

Hunt, J. C. R. (1973), "A theory of turbulent flow around two-dimensional bluff bodies", *J. Fluid Mech.*, **61**, 625-706.

Hunt, J. C. R., S. Leibovich and K. J. Richards (1988), "Turbulent shear flow over low hills", *Quart. J. Roy. Met. Soc.*, **114**, 1435-1470.

Jackson, P. S. and J. C. R. Hunt (1975), "Turbulent wind flow over a low hill", *Quart. J. Roy. Met. Soc.*, **101**, 929-955.

Joseph, J. H., W. J. Wiscombe and J. A. Weinman (1976), "The delta-Eddington approximation for radiative flux transfer", *J. Atmos. Sci.*, **33**, 2452-2459.

Klebanoff, P. S. (1955), "Characteristics of turbulence in a boundary layer with zero pressure gradient", NACA Report No.1247.

Krettenauer, K. and U. Schumann (1992), "Numerical solution of turbulent convection over wavy terrain", *J. Fluid Mech.*, **237**, 261-300.

Lewellen, W. S. (1977), "Use of invariant modeling", *Handbook of Turbulence*, ed. W. Frost and T. H. Moulden, Plenum Press, pp237-280.

Lewellen, W. S. and Y. P. Sheng (1980), "Modeling of dry deposition of SO<sub>2</sub> and sulfate aerosols", EPRI, EA-1452, Project 1306-1, 67pp.

Lumley, J. L. and H. A. Panofsky (1964), "The structure of atmospheric turbulence", Wiley Interscience, New York, 239pp.

Mason, P. J. (1988), "The formation of areally averaged roughness lengths", *Quart. J. Roy. Met. Soc.*, **114**, 399-420.

- Mason, P. J. (1989), "Large-eddy simulation of the convective atmospheric boundary layer", *J. Atmos. Sci.*, **46**, 1492-1516.
- Mason, P. J. (1992), "Large-eddy simulation of dispersion in convective boundary layers with wind shear", *Atmos. Env.*, **26A**, 1561-1572.
- Mason, P. J. and N. S. Callen (1986), "On the magnitude of the subgrid-scale eddy coefficient in large-eddy simulations of turbulent channel flow", *J. Fluid Mech.*, **162**, 439-462.
- Mason, P. J. and D. J. Thompson (1987), "Large-eddy simulations of the neutral-static-stability planetary boundary layer", *Quart. J. Roy. Met. Soc.*, **113**, 413-444.
- Mason, P. J. and D. J. Thompson (1992), "Stochastic backscatter in Large-eddy simulation of boundary layers", *J. Fluid Mech.*, **242**, 51-78.
- McMahon, T. A. and P. J. Denison (1979), "Empirical atmospheric deposition parameters - a survey", *Atmos. Env.*, **13**, 571-585.
- Newley, T. M. J. (1985), "Turbulent air flow over hills", Ph.D Thesis, Cambridge University.
- Nicholson, K. W. (1988), "The dry deposition of small particles: a review of experimental measurements", *Atmos. Env.*, **22**, 2653-2666.
- Paine, R. J. (1987), "User's guide to the CTDM meteorological preprocessor (METPRO) program", Contract No 68-02-3421, .Atmos. Sci. Res. Lab., USEPA.
- Paine, R. J., and S. R. Hanna (1986), "User's guide to the Hybrid Plume Dispersion Model (HPDM) and its associated processors, Version 2.1", EPRI Document PD-034-585.
- Panofsky, H. A. and J. Dutton (1984), "Atmospheric turbulence", Wiley, New York, 397pp.
- Pasquill, F. (1974), "Atmospheric Diffusion", Ellis Horwood, Chichester, 429pp.

Peters, K. and R. Eiden (1992), "Modelling the dry deposition velocity of aerosol particles to a spruce forest", *Atmos. Env.*, **26A**, 2555-2564.

Piacsek, S. A. and G. P. Williams (1970), "Conservation properties of convection difference schemes", *J. Comp. Phys.*, **6**, 392-405.

Rogallo, R. S. and P. Moin (1984), "Numerical simulation of turbulent flows", *Ann. Rev. Fluid Mech.*, **16**, 99-137.

Saucier, R. (1987), "NUSSE3 model description", Chemical Research and Development & Engineering Center, CRDEC-TR-87046.

Schmidt, H. and U. Schumann (1989), "Coherent structure of the convective boundary layer derived from large-eddy simulations", *J. Fluid Mech.*, **200**, 511-562.

Schumann, U. (1988), "Minimum friction velocity and heat transfer in the rough surface layer of a convective boundary layer", *Boundary-Layer Met.*, **44**, 311-326.

Schwartz, S. E. (1992), "Why is clean air clean?", Fifth Int. Conf. on Precipitation Scavenging and Atmosphere-Surface Exchange, July 1991, Richland, WA, 393-399, Hemisphere.

Sehmel, G. A. (1973), "Particle eddy diffusivities and deposition velocities for isothermal flow and smooth surfaces", *Aerosol Sci.*, **4**, 125-138 .

Sehmel, G. A. (1980), "Particle and gas dry deposition: a review", *Atmos. Env.*, **14**, 983-1011.

Shaw, R. H. (1977), "Secondary wind speed maxima inside plant canopies", *J. Appl. Met.*, **16**, 514-521.

Shettle, E. P. and J. A. Weinman (1970), "The transfer of solar irradiance through inhomogeneous turbid atmospheres evaluated by Eddington's approximation", *J. Atmos. Sci.*, **27**, 1048-1055.

Slinn, W. G. N. (1982), "Predictions for particle deposition to vegetative canopies", *Atmos. Env.*, **16**, 1785-1794.

So, R. M. C. and G. L. Mellor (1975), "Experiment on turbulent boundary layers on a concave wall", *Aero. Quart.*, **26**, 25-40.

Spalart, P. R. (1989), "Theoretical and numerical study of a three-dimensional turbulent boundary layer", *J. Fluid Mech.*, **205**, 319-340.

Sykes, R. I. (1980), "An asymptotic theory of incompressible turbulent boundary-layer flow over a small hump", *J. Fluid Mech.*, **101**, 647-670.

Sykes, R. I. and D. S. Henn (1989), "Large-eddy simulation of turbulent sheared convection", *J. Atmos. Sci.*, **46**, 1106-1118.

Sykes, R. I., D. S. Henn and W. S. Lewellen (1993), "Surface-layer description under free-convection conditions", *Quart. J. Roy. Met. Soc.*, **119**, 409-421.

Sykes, R. I., S. F. Parker and D. S. Henn (1993), "Probabilistic prediction of late-time nuclear clouds", DNA-TR-93-61.

Tani, I. (1962), "Production of longitudinal vortices in the boundary layer along a concave wall", *J. Geophys. Res.*, **67**, 3075-3080.

Taylor, P. A., R. I. Sykes and P. J. Mason (1989), "On the parameterization of drag over small-scale topography in neutrally-stratified boundary-layer flow", *Boundary-Layer Met.*, **48**, 409-422.

Townsend, A. A. (1976), "*The structure of turbulent shear flow*", Cambridge University Press, Cambridge, 429pp.

Tsay, S.-C., G. L. Stephens and T. J. Greenwald (1991), "An investigation of aerosol microstructure on visual air quality", *Atmos. Env.*, **25A**, 1039-1054.

Vihma, T. and H. Savijärvi (1991), "On the effective roughness length for heterogeneous terrain", *Quart. J. Roy. Met. Soc.*, **117**, 399-408.

Walko, R. L., W. R. Cotton and R. A. Pielke (1992), "Large-eddy simulations of the effects of hilly terrain on the convective boundary layer", *Boundary-Layer Met.*, **58**, 133-150.

Wilson, N. R. and R. H. Shaw (1977), "A higher order closure model for canopy flow", *J. Appl. Met.*, **16**, 1197-1205.

Wiman, B. L. B. and G. I. Agren (1985), "Aerosol depletion and deposition in forests - a model analysis", *Atmos. Env.*, **19**, 335-347.

Wood, N. and P. J. Mason (1991), "The influence of static stability on the effective roughness lengths for momentum and heat transfer", *Quart. J. Roy. Met. Soc.*, **117**, 1025-1056.

Wyngaard, J. C. (1985), "Structure of the Planetary Boundary Layer and Implications for its Modeling", *J. Climate Appl. Meteor.*, **24**, 1131-1142.

Wyngaard, J. C. and R. A. Brost (1984), "Top-down and bottom-up scalar diffusion in the convective boundary layer", *J. Atmos. Sci.*, **41**, 102-112.

Wyngaard, J. C. and A. Venkatram (Eds.) (1988), "*Lectures on air pollution modeling*", American Meteorological Society, Boston, 390pp.

## DISTRIBUTION LIST

DNA-TR-93-175

### DEPARTMENT OF DEFENSE

ASSISTANT TO THE SECRETARY OF DEFENSE  
ATTN: EXECUTIVE ASSISTANT

DEFENSE INTELLIGENCE AGENCY  
ATTN: PGI-4

DEFENSE NUCLEAR AGENCY  
2 CY ATTN: IMTS  
ATTN: NASF  
ATTN: OPNA  
5 CY ATTN: RAEM  
ATTN: RAEM ROBERT KEHLET  
2 CY ATTN: SPWE  
ATTN: SPWE LTC JIM HODGE  
ATTN: SPWE LTC MARK BYERS  
ATTN: SPWE MAJ ROB COX  
ATTN: SPWE K PETERSEN

DEFENSE TECHNICAL INFORMATION CENTER  
2 CY ATTN: DTIC/OC

### DEPARTMENT OF THE ARMY

ARMY RESEARCH LABORATORIES  
ATTN: SLCM-SE

US ARMY CHEMICAL SCHOOL  
ATTN: COMMANDING OFFICER

USA CML & BIOLOGICAL DEFENSE AGENCY  
ATTN: AMSCB-BDL J CANNALIATO

### DEPARTMENT OF THE NAVY

NAVAL AIR SYSTEMS COMMAND  
ATTN: E ECK

NAVAL RESEARCH LABORATORY  
ATTN: CODE 7920

NAVAL SURFACE WARFARE CENTER  
ATTN: CODE K42 L VALGE

OFFICE OF CHIEF NAVAL OPERATIONS  
ATTN: NUC AFFAIRS & INT'L NEGOT BR

STRATEGIC SYSTEMS PROGRAM  
ATTN: SP0272 R G STANTON

### DEPARTMENT OF THE AIR FORCE

AIR FORCE STUDIES AND ANALYSIS  
ATTN: AFSAAS/SAS

AIR UNIVERSITY LIBRARY  
ATTN: AUL-LSE

HQ USAF/XOFS  
ATTN: XOFN

WRIGHT RESEARCH & DEVELOPMENT CENTER  
ATTN: D RICHMOND

### DEPARTMENT OF ENERGY

LAWRENCE LIVERMORE NATIONAL LAB  
ATTN: ALLEN KUHL

### OTHER GOVERNMENT

CENTRAL INTELLIGENCE AGENCY  
ATTN: OSWR/NED 5S09 NHB

### DEPARTMENT OF DEFENSE CONTRACTORS

JAYCOR  
ATTN: CYRUS P KNOWLES

KAMAN SCIENCES CORP  
ATTN: DASIAC

KAMAN SCIENCES CORPORATION  
ATTN: DASIAC

LOGICON R & D ASSOCIATES  
ATTN: E FURBEE  
ATTN: J WEBSTER  
ATTN: R POPE

LOGICON R & D ASSOCIATES  
ATTN: G GANONG

MCDONNELL DOUGLAS CORPORATION  
ATTN: L COHEN

NORTHROP CORP  
ATTN: G CURRY

S-CUBED  
ATTN: C NEEDHAM

SCIENCE APPLICATIONS INTL CORP  
ATTN: D BACON  
ATTN: J COCKAYNE  
ATTN: P VERSTEEGEN

TITAN CORPORATION (THE)  
2 CY ATTN: C P CERASOLI  
2 CY ATTN: D S HENN  
2 CY ATTN: R I SYKES

W J SCHAFFER ASSOCIATES, INC  
ATTN: S HOWIE